# Data Analysis and Lattice Calculations for HERMES


**Diploma Thesis**

by

**Florian Sanftl**

from

Landshut

Institute for Theoretical Physics

at the University of Regensburg

supervised by

Prof. Dr. Andreas Schäfer

Regensburg

in May 2009

*”Non quia difficilia sunt non audemus,*
*sed quia non audemus difficilia sunt.”*
L.A. Seneca

# Contents


**1 Introduction** **1**

## Part I The Analysing Power $A_{UT}$ of Inclusive Charged Mesons at HERMES

**2 The Phenomenological Framework** **7**
2.1 $ep$ Scattering . . . 7
2.1.1 Deep-Inelastic Scattering (DIS) . . . 7
2.1.2 The Quark Parton Model . . . 11
2.1.3 Quantum Chromodynamics . . . 12
2.2 The Structure of the Nucleon . . . 13
2.2.1 Leading-Twist without Transverse Momenta: $q(x)$, $\Delta q(x)$ and $\delta q(x)$ . . . 13
2.2.2 Quark-Nucleon Helicity Amplitudes . . . 15
2.2.3 Transverse Momentum Dependent Distribution Functions . . . 16
2.2.4 Gauge Link and naïve T–Odd Distribution Functions . . . 17
2.2.5 The Sivers Distribution Function . . . 18
2.2.6 The Collins Fragmentation Function . . . 19
2.2.7 Cross Sections and Azimuthal Asymmetry Moments in Semi-Inclusive DIS . . . 20
2.3 SSAs in $lp^{\uparrow} \rightarrow hX$ and $p^{\uparrow}p \rightarrow hX$ Processes . . . 24

**3 The HERMES Experiment** **27**
3.1 The HERA Lepton Beam . . . 27
3.2 The HERMES Target . . . 28
3.3 The Spectrometer . . . 29
3.3.1 The Tracking System . . . 29
3.3.2 The Particle Identification Detectors . . . 30
3.3.3 The Luminosity Monitor . . . 31
3.4 Data Acquisition (DAQ) and Processing . . . 31

**4 The Extraction of the Analysing Power $A_{UT}$** **33**
4.1 The Extraction Method . . . 33
4.2 The HERMES Data Productions . . . 35
4.3 Burst Level Data Selection . . . 35
4.3.1 Data Quality . . . 35
4.3.2 Calculation of the Luminosity . . . 36
4.4 Track Level Data Selection . . . 37
4.4.1 Geometry Cuts . . . 37
4.4.2 Particle Identification . . . 37
4.4.3 Kinematic Cuts . . . 44
4.4.4 Yields of Inclusive Charged Hadrons . . . 46
4.5 Systematic Studies . . . 47
4.5.1 Effect of the Target Magnet Correcion (TMC) . . . 47
4.5.2 Compatiblity between productions . . . 50

**5 Results and Discussion** **55**
5.1 The Integrated Analysing Power $A_{UT}$ . . . 55
5.2 The Analysing Power $A_{UT}(P_{h\perp}, P_{hz}/E_{Beam})$ . . . 56

5.3 The Disentanglement of Sub-Processes . . . 58
5.3.1 The SIDIS-Region . . . 60
5.3.2 The Photoproduction-Region . . . 62

**Part II The Spin Structure of the $\Lambda^0$ Baryon on the Lattice**

**6 Motivation** **67**

**7 Lattice Quantum Chromo-Dynamics** **69**
7.1 Continuum Quantum Chromodynamics . . . 69
7.2 Discretisation I: The Lattice . . . 70
7.3 Discretisation II: Fermions on the Lattice . . . 71
7.3.1 The Naïve Discretisation . . . 71
7.3.2 Wilson Fermions . . . 72
7.3.3 Clover-Wilson Fermions . . . 73
7.4 Discretisation III: Gluons on the Lattice . . . 73
7.4.1 The Naïve Discretisation . . . 74
7.5 Expectation Values on the Lattice . . . 75
7.6 Propagators . . . 76
7.7 Extraction of Masses . . . 76
7.8 Extraction of Matrix Elements . . . 77

**8 Calculation of the Two- and Three-Point-Functions** **79**
8.1 Two Point Correlation Functions . . . 79
8.1.1 The Meson Case: $K^+$ . . . 79
8.1.2 The Baryon Case I: The $\Lambda^0$ Hyperon . . . 80
8.1.3 The Baryon Case II: The $\Omega^-$ Hyperon . . . 81
8.2 Three Point Correlation Functions . . . 82
8.2.1 The Three Point Function of the $\Lambda^0$ Hyperon . . . 82
8.2.2 Sequential Sources and Propagators . . . 85
8.3 Status of the Numerical Calculations . . . 86

**9 Conclusions** **87**
9.1 Summary . . . 87
9.2 Outlook . . . 88

**A Appendix** **89**
A.1 Conventions . . . 89
A.2 Light-Cone Vectors . . . 89
A.3 Dirac Matrices . . . 89

**References** **91**

**Acknowledgements** **97**

# Chapter 1

# Introduction

Since the beginning of atomic physics, scattering experiments have proven to be a powerful tool to probe the inner structure of matter. Among the best examples is the discovery of the atomic nucleus, achieved in 1909 by Rutherford, Geiger and Marsden by scattering $\alpha$ particles off a gold foil. The increased performances of the particle accelerators over the past decades enabled to dramatically increase the energy of the projectiles and thus their spatial resolution power. As a result the nucleon and its substructures were eventually been resolved adopting a similar approach, though with an enormously greater experimental complexity.
By the end of the 60's, the first inclusive Deep Inelastic Scattering $e+p \rightarrow e'+X$ experiments at SLAC showed that the structure functions of the nucleons were to a large extent independent on the squared momentum transfer $Q^2$. This scaling behaviour of the structure functions was eventually interpreted by Bjorken and Feynman as the evidence of the existence of point-like sub-nucleonic particles, called partons [Bjo69, BP69, Fey69]. These objects were later identified with the quarks, spin 1/2 particles with fractional electric charge and a new degree of freedom called flavour, whose existence had been earlier predicted by Gell-Mann and Zweig on the basis of the symmetry properties of the meson and baryon multiplets [GM64]. The Quark Parton Model, developed in the late 60's, has proven to be particularly successful in the prediction of a number of "macroscopic" observables of the hadrons such as the mass, the charge and the spin. According to this model, the proton is made of three quarks, each carrying approximately a third of the proton mass. Two quarks have flavour up and charge $+\frac{2}{3}e$ and one has flavour down and charge $-\frac{1}{3}e$, thus resulting in a total charge $+e$ (i.e. the same of the electron but with opposite sign). Furthermore, in a proton with spin along a certain direction, two of the quarks have spin in the same direction and one in the opposite direction, thus resulting in a total spin equal to 1/2.
Though this model represented a major step toward the understanding of the inner structure of the nucleon, it was soon found to be not enough appropriate for a comprehensive interpretation of the experimental data. Indeed, experimental results showed that only roughly 50% of the nucleon's momentum is carried by quarks. The missing momentum could only be explained a few years later within the framework of the quantum chromodynamics (QCD), the gauge theory of strong interactions (see Chapter 7). According to this theory, which requires the existence of the colour as an additional degree of freedom of the quarks, the missing momentum of the nucleon is carried by the gluons, the gauge bosons of the strong interaction. These particles do not show up in the electroweak scattering processes as they carry no electro-weak charge. The first evidence for the existence of gluons was the observation of three-jet events at the electron-positron collider PETRA at DESY in 1979 [B$^+$79].
Among the most surprising consequences of QCD is confinement, which causes a quark subjected to a high momentum transfer during a scattering process, to fragment into a colourless bunch of hadrons (jet) along its way to escape the nucleon. Since the momentum, the charge, the flavour and the spin orientation of the struck quark can be indirectly accessed through the analysis of the composition of the hadron jet, the experimental investigation of the hadronic final state in deep inelastic scattering experiments allows a deeper insight into the sub-nuclear processes than inclusive measurements alone.

With the evidence that the proton and the neutron are not elementary particles, physicists were challenged with the task of explaining the nucleon's spin in terms of its constituents. This created a new frontier in hadron physics phenomenology which is still very active and has had a crucial impact in our understanding of the internal structure of the nucleon. The internal dynamic spin structure of the nucleon can be probed by scattering polarised beams off polarised targets. As it is a non-trivial task to produce polarised nuclear targets and high energy polarised beams, the spin distribution of quarks inside the nucleon remained experimentally inaccessible for many years.
The first measurements of polarised electron-proton scattering were performed at SLAC by the E80 and E130 collaborations in the mid '70s [A$^+$76, B$^+$83]. Though affected by large experimental uncertainties, the spin-dependent

structure functions of the proton were found to be in reasonable agreement with the theoretical predictions. A break-through occurred in the late '80s, when the EMC [A$^+$89] collaboration repeated these measurements at CERN with higher precision and in a wider kinematic range using a polarised muon beam with an energy 10 times higher than at SLAC. The reported results for the spin-dependent structure function of the proton were found to be in strong disagreement with the predictions of the Ellis-Jaffe sum rule [EJ74, A$^+$88]. When used in combination with SU(3) symmetry arguments to calculate the fraction of the nucleon's spin carried by the up, down and sea quarks, this result implies that the majority of the spin of the nucleon is not carried by the quarks, a major surprise that came soon to be known as the 'spin crisis'. This unexpected result, which caused a lot of excitement in the high energy physics community, was especially surprising since the extraction of the static magnetic moments of the nucleons, based on similar symmetry arguments, was in perfect agreement with the quark model predictions. The EMC results were substantially confirmed for both the proton and the neutron by the SMC experiment at CERN [A$^+$93, A$^+$94, A$^+$95, A$^+$97] and the E142 experiment at SLAC [A$^+$96] in the following years. The SMC experiment also provided another important result: the first determination of the separate contributions of the valence and the sea quarks to the nucleon spin in Semi-Inclusive Deep Inelastic Scattering measurements [A$^+$98b]. In such measurements, the scattered lepton is required to be detected in coincidence with at least one of the hadrons produced in the fragmentation of the struck quark ($e+p \rightarrow e+h+X$). The immediate consequence of all these results was that there ought to be additional sources of spin within the nucleon besides the quarks. The most natural candidates are the spin of the gluons $\Delta G$ and the orbital angular momentum of quarks $L_z^q$ and gluons $L_z^G$:

$$s_z^N = \frac{1}{2} = \frac{1}{2}\Delta\Sigma + \Delta G + L_z^q + L_z^G, \tag{1.0.1}$$

where

$$\Delta\Sigma = \Delta u_v + \Delta d_v + \Delta q_s \tag{1.0.2}$$

is the contribution carried by the valence and sea quark spins. Precision measurements from the HERMES and the COMPASS experiments have recently established that this contribution is of the order of 30%.

In the last few years, a rapidly increasing attention has been devoted until now, from both the theoretical and the experimental point of view, to the non-collinear phenomena in the nucleon. It was indeed realised that many important new aspects of the nucleon structure can be accessed through the so-called Transverse Momentum Dependent (TMD) distribution functions. These distribution functions arise when the quark transverse momentum $p_T$ is not integrated over. Among them the Sivers function is particularly interesting since its existence requires a nonzero orbital angular momenta of the quarks and has been linked to the spatial distribution of partons inside the nucleon [BHS02, Bur02]. The Sivers function describes the correlation between the transverse polarisation of the target nucleon and the transverse momentum $p_T$ of quarks (Sivers mechanism) [Siv91, Siv90]. The Sivers function appears together with the well known spin-independent fragmentation function (Sivers moments) in the cross section for a transversely polarised nucleon and produces a different left-right asymmetry. From 2002 to 2005 the HERMES experiment was operated with a hydrogen target polarised transversely to the direction of the HERA lepton beam. The data collected during this period allowed the study of transverse target Single Spin Asymmetries (SSA). In particular, the extraction of the analysing power $A_{UT}$ (in literature also the notation $A_N$ is common) of inclusive charged hadrons from the full HERMES transverse data set is presented in this thesis. This extraction is the most precise measurement of the analysing power $A_{UT}$ ($A_N$) kind so far.

### Outline of the thesis

This thesis is organised as follows. It is devided into two parts. In the first part, we will perform a analysis of the Single Spin Asymmetry $A_{UT}$ of charged mesons produced in $lp^\uparrow \rightarrow hX$-processes. The theoretical framework for inclusive and semi-inclusive deep inelastic scattering is provided in Chapters 2. A phenomenological and historical perspective is adopted for the description of the inclusive hadronic processes, a detailed treatment of the formalism concerning the physics of the transverse degrees of freedom of the nucleon is presented as well. In Chapter 3 the main components of the HERMES experimental apparatus are presented. Therefore, we will focus on the description of the main features of the spectrometer, tracking and particle identification algorithms and data acquisition. The extraction of the Single Spin Asymmetry $A_{UT}$ is discussed in Chapter 4 after a brief overview of the main steps of the underlying data analysis. A selection of systematic studies is also reported at the end of this chapter. In Chapter 5 the results of the measurement of the Single Spin Asymmetry $A_{UT}$ are presented, the underlying physical sub-processes are disentengled and identified based on data (meaning without the use of dedicated Monte-Carlo simulations). The discussion and the attempt to interpret the results is also part of Chapter 5.

The second part is devoted to the spin structure of the $\Lambda^0$ hyperon. In Chapter 6 we will give a motivation for the investigation of the $\Lambda^0$ spin structure. Models to describe the spin structure are addressed as well. In Chapter 7 we will give a short introduction to lattice-QCD which is our theoretical tool of choice to access the spin structure of the $\Lambda^0$ in a non-perturbative manner. In Chapter 8 we will present the two- and three-point functions necessary to extract the relevant matrix-elements connected to the spin structure. In addition we will give a short status report about the still ongoing numerical calculations.
Final conclusions and a brief summary of Part I and Part II are reported in Chapter 9.

# Part I

# The Analysing Power $A_{UT}$ of Inclusive Charged Mesons at HERMES

# Chapter 2

# The Phenomenological Framework

In this chapter quark distribution and fragmentation functions, which appear in the cross section for semi–inclusive deep–inelastic scattering, are introduced and their properties described. The topic of this thesis is the extraction of the analysing power $A_{UT}$ which is very closely connected to the Sivers distribution function. Thus we will focus on this naïve-T-odd Sivers distribution function [Siv90, Siv91], $f_{1T}^{\perp q}$, which describes the correlation between the transverse polarisation of the nucleon and the transverse momentum $p_T$ of the quarks within. Although we are not able to access them directly in our analyis, we will for completeness address the Collins fragmentation function as well. Furthermore, the concept of cross–section asymmetries — the measured observables in deep–inelastic scattering experiments for the extraction of quark distribution functions is presented.
The definition of twist as proposed in [Jaf96] is used, i.e., a leading–twist or respectively twist–two term is identified with a term of leading order in a $1/Q$ expansion. In the subsequent chapter we will also use the concept of light-cone coordinates (cf. Appendix A, [Jaf96]). In light-cone coordinates the leading twist term is of order $1/P^+$.
The notation of Mulders and Tangermann [MT96] is applied to the distribution and fragmentation functions (in the following abbreviated as DF and FF) except for the three leading–twist distribution functions that do not vanish when integrated over transverse quark momenta. For these three functions, $q(x,\vec{p}_T^{\,2})$ refers to the unpolarised distribution $f_1^q(x,\vec{p}_T^{\,2})$, $\Delta q(x,\vec{p}_T^{\,2})$ to the helicity distribution $g_{1L}^q(x,\vec{p}_T^{\,2})$, and $\delta q(x,\vec{p}_T^{\,2})$ to the transversity distribution $h_1^q(x,\vec{p}_T^{\,2})$, where $p_T$ is the intrinsic quark transverse momentum. The definitions of the azimuthal angles and the asymmetries follow the Trento conventions [BDDM04]. Throughout this work, four–vectors are written as normal symbols, e.g., $q$, space vectors with three or two components are indicated by arrows, e.g., $\vec{p} = (\vec{p}_T, p_z)$, where transverse vectors (with two components) have an additional subscript $T$. As common in high energy physics, we work in the framework of natural units, meaning that $\hbar = c = 1$. Further notations and conventions for Part I can be found in Appendix A.

## 2.1 $ep$ Scattering

### 2.1.1 Deep-Inelastic Scattering (DIS)

A very successful tool to gain information about the inner structure of the nucleon is the deep–inelastic scattering process which is described in this section. Inclusive deep–inelastic scattering was the first process in which point–like partons were identified inside the nucleon. In the deep–inelastic scattering (DIS) process a lepton scatters off a nucleon via the exchange of a virtual boson. Details on this type of reactions can be found in [PS95, HM84, Man92]. For charged leptons and moderate squared momentum transfers to the target, $Q^2$, the exchange of a single virtual photon, as shown in Figure 2.1, is the dominant process during which the nucleon breaks up and forms a final hadronic state $X$. The maximum possible momentum transfer is determined by the centre-of-mass energy $\sqrt{s}$ which is only about 7.2 GeV at the HERMES experiment. In inclusive DIS only the scattered lepton is detected whereas additional hadrons of the final state $X$ are detected in semi-inclusive DIS processes. In contrast to inclusive and semi-inclusive DIS the hadronic state $X$ is fully reconstructed in exclusive DIS. The momentum transfer $q = k - k'$ is spacelike so we use $Q^2 = -q^2$ and this implies an energy loss for the electron in the laboratory frame of $\nu = P \cdot q / m_N$. The squared momentum transfer to the target $Q^2$ is a measure of the spatial resolution in the scattering process. In DIS processes, $Q^2$ is large enough to resolve the constituents of the nucleon (cf. Figure 2.4).

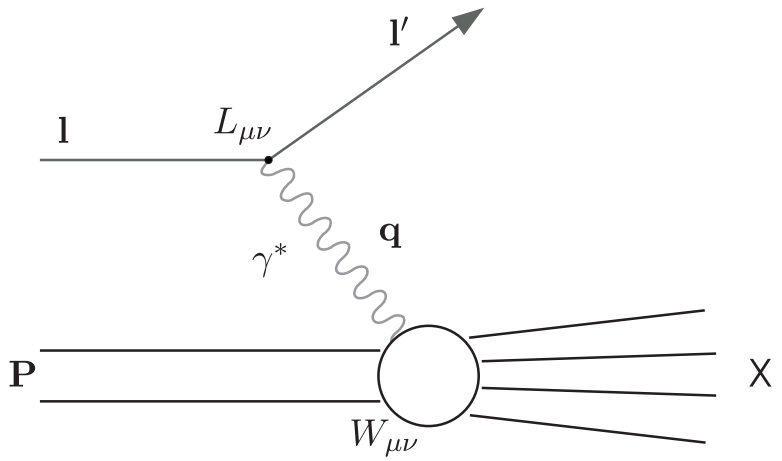


**Figure 2.1:** Lowest order DIS process in the one–photon exchange in the laboratory system.

The invariant matrix element of this process it given by

$$i\mathcal{M}(eN \to eX) = \bar{u}(k',\lambda')(-ie\gamma_\mu)u(k,\lambda)\left(\frac{-ig_{\mu\nu}}{q^2}\right)\int d^4x e^{iqx}\langle X|J^\nu(x)|P,\lambda\rangle, \tag{2.1.1}$$

where $J^\nu(x)$ is the quark electromagentic current

$$J^\nu(x) = \sum_f Q_f \bar{q}_f \gamma^\mu q_f. \tag{2.1.2}$$

Here, $Q_f$ is the is the electromagnetic charge of quark flavour $q$ in units of the elementary charge $|e|$. The hadronic matrix element $\langle X|J^\nu|P\rangle$ cannot be calculated by perturbation theory as the QCD coupling is large at the scale of the nucleon mass. To obtain the cross section from this matrix element, it must however be squared and summed over all possible final states $X$. Using the optical theorem we can write the result as a product

$$d\sigma \propto L_{\mu\nu}W^{\mu\nu}, \tag{2.1.3}$$

where the leptonic tensor $L_{\mu\nu}$ is calcuable using pure QED:

$$\begin{aligned} L_{\mu\nu} &= 2(k_\mu k'_\nu + k'_\mu k_\nu - g_{\mu\nu}(k'\cdot k - m_e^2) + i\varepsilon_{\mu\nu\rho\sigma}s_e^\rho q^\sigma) \\ &= 2(L^{(S)}_{\mu\nu} + iL^{(A)}_{\mu\nu}) \end{aligned} \tag{2.1.4}$$

and the hadronic part, $W^{\mu\nu}$, can be decomposed as follows

$$W^{\mu\nu}(P,q)_{\lambda,\lambda'} = \frac{1}{4\pi}\int d^4x e^{iqx}\langle P,\lambda'|[J^\mu(x),J^\nu(0)]|P,\lambda\rangle. \tag{2.1.5}$$

As the nucleon is a spin-$\frac{1}{2}$ particle with polarisation $s$, we can define the density matrix [Man92]

$$\rho = \frac{1}{2}\left(1 + \frac{\vec{\sigma}\cdot\vec{s}}{m_N}\right) \tag{2.1.6}$$

and combine it with Equation (2.1.5) to

$$W^{\mu\nu}(P,q,s) = \mathrm{Tr}(\rho W^{\mu\nu}) = W^{\mu\nu}_{(S)} + iW^{\mu\nu}_{(A)}. \tag{2.1.7}$$

$W^{\mu\nu}_{(S)}$ is the symmetric, spin independent part of $W^{\mu\nu}$, whereas $W^{\mu\nu}_{(A)}$ is the anti-symmetric part containing all spin-dependent information of the nucleon. The complex inner structure of the nucleon prevents the exact calculation of the hadronic tensor. Only a parametrisation in terms of structure functions is possible. A further advantage of the decomposition of $W^{\mu\nu}$ in

$$W^{\mu\nu}_{(S)} = \left(-g_{\mu\nu} + \frac{q^\mu q^\nu}{q^2}\right)F_1(x,Q^2) + \frac{1}{P\cdot q}\left(P^\mu - \frac{P\cdot q}{q^2}q^\mu\right)\left(P^\nu - \frac{P\cdot q}{q^2}q^\nu\right)F_2(x,Q^2), \tag{2.1.8}$$

$$W^{\mu\nu}_{(A)} = \frac{1}{P\cdot q}\varepsilon^{\mu\nu\rho\sigma}q_\rho\left(s_\sigma g_1(x,Q^2) + \left(s_\sigma - \frac{s\cdot q}{P\cdot q}P_\sigma\right)g_2(x,Q^2)\right) \tag{2.1.9}$$

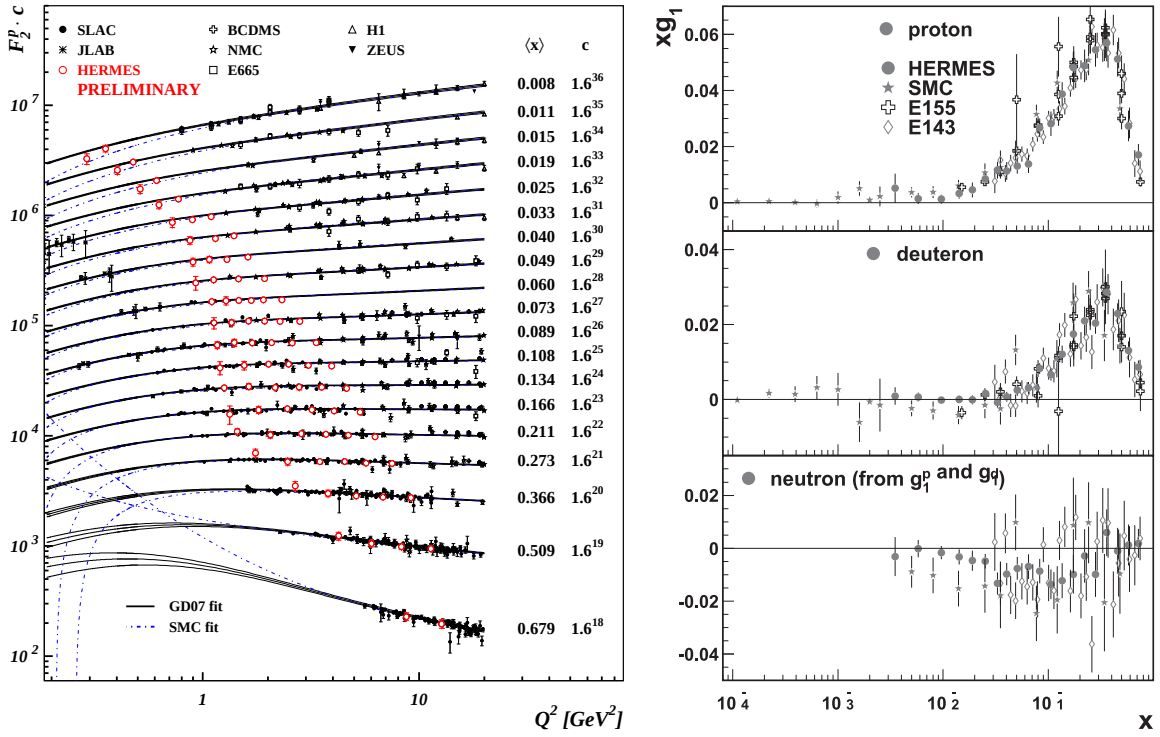


**Figure 2.2: Left**: The world data of $F_2^p$ is compared to phenomenological parameterisations. Latest HERMES results are included (red circles). Source: [Gab08]. **Right**: The spin–dependent structure function $xg_1$ of the proton, deuteron, and neutron measured as function of $x$ in DIS of polarised leptons. Source: [A$^+$07a]

is that it fulfils additional symmetry requirements as Lorentz covariance, gauge invariance, and parity conservation of the electromagnetic interaction. In Equations (2.1.8) and (2.1.9), we have introduced the variable $x$. It is called the Bjorken scaling variable and is defined as follows

$$x = \frac{-t}{s+u} = \frac{Q^2}{2k\cdot P - 2k'\cdot P} = \frac{Q^2}{2P\cdot q} = \frac{Q^2}{2m_N \nu}. \tag{2.1.10}$$

It satisifies $0 \leq x \leq 1$ due to $s = (P+q)^2 \geq m_N^2$. It can be interpreted as a measure for the inelasticity of the scattering process, where $x = 1$ corresponds to the fully elastic limit. The functions $F_1$, $F_2$ and $g_1$, $g_2$ are called the structure functions of the nucleon. From the Lorentz structure of the leptonic tensor $L_{\mu\nu}$ we can see that $F_1$ and $F_2$ can be determined from unpolarised DIS experiments while in order to measure $g_1$ and $g_2$ polarised particles are necessary. Figure 2.2 shows the latest results of DIS measurments on $g_1$ and $F_2$.
Using the relative energy transfer

$$y = \frac{\nu}{E_e} = \frac{p\cdot q}{p\cdot k}, \tag{2.1.11}$$

the final unpolarised cross section can be written in a very compact form:

$$\frac{d^2\sigma}{dx\,dy}(eN \to eX) = \frac{4\pi\alpha^2}{Q^4} s[xy^2 F_1(x,Q^2) + (1-y)F_2(x,Q^2)] \tag{2.1.12}$$

If both the incident lepton beam and the target protons are longitudinally polarised, the antisymmetric (spin-dependent) parts of the leptonic and hadronic tensors contribute to the cross section. Since in this case both the symmetric and anti-symmetric part of the cross section are non-vanishing, the only way to isolate the spin-dependent component consists in measuring the difference of the cross sections obtained with two opposite target spin states. More details on the calculation of polarised and unpolarised DIS cross sections can be found in Reference [AEL95], for instance. An overview over all relevant kinematic variables which will be used in this Chapter can be found in Table 2.1

| Variable | Description |
|---|---|
| $k = (E_e, \vec{k}), k' = (E'_e, \vec{k'})$ | 4-Momentum of Incoming and Outgoing Lepton |
| $P \overset{\text{lab}}{=} (m_N, \vec{0})$ | 4-Momentum of the Target nucleon |
| $\phi$, $\theta$ | Polar and Azimuthal Scattering Angles |
| $q = (\nu, \vec{q})$ | 4-Momentum of the Virtual Photon |
| $Q^2 = -q^2 \overset{\text{lab}}{\cong} 4EE' \sin^2(\theta/2)$ | Negative Squared 4-Momentum Transfer |
| $\nu = \frac{P \cdot q}{m_N} = E - E'$ | Energy Transfer from the Incoming Lepton to the Target Nucleon |
| $x = \frac{Q^2}{2P \cdot q} \overset{\text{lab}}{\cong} \frac{Q^2}{2m_N \nu}$ | Bjorken Variable |
| $y = \frac{P \cdot q}{P \cdot k} \overset{\text{lab}}{\cong} \frac{\nu}{E}$ | Fractional Energy of the Virtual Photon |
| $W^2 = (P+q)^2 \overset{\text{lab}}{\cong} m_N^2 + 2m_N \nu + Q^2$ | Squared Invariant Mass of the Hadronic Final State |
| $P_h = (E_h, \vec{P}_h)$ | 4-Momentum of a Final State Hadron |
| $z = \frac{P \cdot P_h}{P \cdot k} \overset{\text{lab}}{\cong} \frac{E_h}{\nu}$ | Fractional Energy of the Final State Hadron |
| $P_{h\perp} = \frac{\lvert\vec{P}_h \times \vec{q}\rvert}{\lvert\vec{q}\rvert}$ | Transverse Momentum of the Hadron |
| $\phi_h$ | Azimuthal Angle of the Hadron w.r.t. Scattering Plane |

**Table 2.1:** Summary of the most important kinematic variables used in DIS.

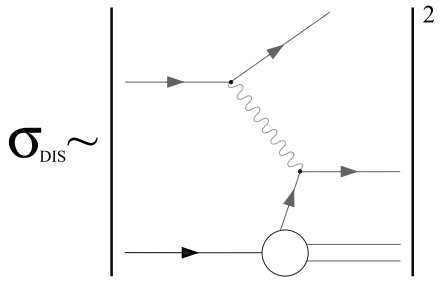


**Figure 2.3:** DIS in the parton model (laboratory frame!). The target is a cloud of partons and the lepton scatters elastically from one of the partons by exchanging a virtual photon.

### 2.1.2 The Quark Parton Model

The Quark PartonModel (QPM) was developed by Bjorken and Feynman in the late 1960's [Bjo69, BP69, Fey69]. The QPM is conveniently formulated in a reference frame where the nucleon moves with very high momentum (infinite-momentum frame or Breit frame), such that the transverse momentum components and the rest mass of the constituents and the nucleon itself can be neglected. In this special frame the scattering can be viewed as the absorption of a virtual photon by one of the collinearly moving partons inside the nucleon. The struck parton, which carries a fraction $p = \xi P$ of the total momentum of the nucleon, recoils with its original momentum reversed, as shown in Figure 2.3. After the absorption of the virtual photon, the mass-shell relation for the struck parton yields:

$$(\xi P + q)^2 = (\xi P)^2 + 2\xi P \cdot q - Q^2 = 0, \tag{2.1.13}$$

where $q = (\nu, \vec{q})$ is the four-momentum of the virtual photon and $Q^2 = -q^2$. Being a Lorentz invariant quantity, Equation (2.1.13) also holds in the laboratory frame, where $P = (m_N, \vec{0})$ (e.g. for a fixed target experiment):

$$(\xi m_N)^2 + 2\xi m_N \nu - Q^2 = 0. \tag{2.1.14}$$

In the scaling limit $Q^2 \gg m_N^2$, $\xi$ can be identified with is the definition of the Bjorken $x$ variable (cf. Equation (2.1.10)). In the QPM the Bjorken $x$ variable can thus be interpreted as the fractional momentum of the nucleon carried by the struck quark, and the DIS process consists in the incoherent sum of elastic scattering off the partons carrying a momentum fraction $x$ of the nucleon momentum. Thus we will use $x$ instead of $\xi$. The limit $Q^2 \to \infty$, $\nu \to \infty$ and $x = fixed$ is called Bjorken limit (which is equivalent to the expressions Bjorken scaling or scale invariance). This means that for the full nucleon, built up from partons of type $q$ with distributions $q(x)$, we can write the cross section as a sum of incoherent single parton scatterings (cf. Figure 2.3):

$$\sigma(eN \to eX) = \int_0^1 dx \sum_q q(x)\, \sigma(e\,q(xP) \to e q(p')). \tag{2.1.15}$$

The model, however, requires that the interaction between the individual partons is weak on short distances. This circumstance is satisfied if the scattering occurs on sufficiently short time scales, i.e. much shorter that the typical time scales of the interactions between partons. In this approximation, known as the Impulse Approximation, the partons can be regarded as a gas of quasi-free particles.
In the QPM the nucleon is described in terms of the parton distribution functions (DF) $q(x)$, which represent the probability density to find in the nucleon a quark of flavour $q$ and fractional momentum $x$. The quantity $q(x)\,dx$ thus represents the number of quarks with flavour $q$ and fractional momentum in the range $[x, x+dx]$. In the helicity base, the DF $q(x)$ can be split up in functions for quarks with parallel $(+)$ and antiparallel $(-)$ orientation of the spin with respect to the nucleon spin:

$$q(x) = q^+(x) + q^-(x). \tag{2.1.16}$$

It is possible to define some constraints by the number of valence quarks of given flavour $N_q$.

$$\int_0^1 dx\, [q(x) - \bar{q}(x)] = N_q. \tag{2.1.17}$$

Thus summing over all possible momtentum fractions yields the full nucleon momentum

$$\sum_{q,\bar{q}} \int_0^1 dx\, x\, q(x) = 1. \tag{2.1.18}$$

The polarised or helicity DF is then defined as

$$\Delta q(x) = q^+(x) + q^-(x). \tag{2.1.19}$$

The spin-independent and spin-dependent structure functions $F_1$, $F_2$ and $g_1$ (cf. previous Subsection) can now be interpreted within the QPM as the charge-weighted sums over the quark flavours $q$ (including anti-quarks) of the corresponding parton distribution functions:

$$F_1(x) = \frac{1}{2}\sum_q e_q^2 q(x) \tag{2.1.20}$$

$$g_1(x) = \frac{1}{2}\sum_q e_q^2 \Delta q(x) \tag{2.1.21}$$

$$g_2(x) = 0, \tag{2.1.22}$$

where $e_q$ is the fractional charge carried by the quarks. Since the structure function $g2$ is related to the transverse degrees of freedom of the quarks within the nucleon, it has no interpretation and vanishes in the QPM, where all the partons are assumed to move collinearly to the nucleon. The structure functions $F_1(x)$ and $F_2(x)$ are connected via the Callan-Gross [CG69] relation by

$$F_2(x) = 2xF_1(x). \tag{2.1.23}$$

In general the structure functions vary with $x$ and $Q^2$. In the QPM, however, they are independent of $Q^2$. This leads to the famous Bjorken scaling. The tree level process in Figure 2.3 will of course have to be corrected by higher order processes. This allows for a dependence on $Q^2$, which will however be relatively mild, on the order of $\ln Q^2$. These "scaling violations" were a direct test of QCD. A $Q^2$-independence of the structure functions would imply that the electromagnetic probe (incoming lepton) "sees" the same proton structure no matter how big the spatial resolution is (cf. Figure 2.4).

### 2.1.3 Quantum Chromodynamics

The violation of scaling can be explained if quarks interact with each other in the nucleon. In the late 1970s, a field theory of Quantum Chromodynamics (QCD) was developed whose basic fields are quarks interacting via electrically neutral vector gluons. QCD is the non–Abelian gauge theory (cf. Section 7.1 in Chapter 7) of the strong interaction and part of the Standard Model. Quarks couple to the strong interaction through three different colours. In contrast to Quantum Electrodynamics where the photons have no electrical charge and cannot couple to each other, the field quanta of the strong interaction, i.e., the gluons, do carry colour charge. This causes a scale or energy dependence of the strong coupling constant $\alpha_S$:

$$\alpha_S(Q^2) = \frac{12\pi}{(33 - n_f)\ln(Q^2/\Lambda_{\mathrm{QCD}^2})} \tag{2.1.24}$$

The QCD scale parameter $\Lambda_{\mathrm{QCD}}$ depends on the number of quark flavours $n_f$ and the renormalisation scheme. It is of the order of a couple of hundred MeV. Equation (2.1.24) is only valid for $Q^2 \gg \Lambda_{\mathrm{QCD}}$ and shows that the coupling decreases with increasing $Q^2$ and reaches zero for $Q^2 \to \infty$, i.e. in the Bjorken limit explained in the previous Subsection. This feature, which only appears in non.Abelian gauge theories, is called asymptotic freedom. It explains the success of the description of experimental results with the QPM in which the quarks are treated as free partons. For $\alpha_s \ll 1$ perturbative QCD is applicable and only lower order diagrams have to be taken into account. But the coupling constant is not necessarily smaller than 1 for small $Q^2$ so that perturbation theory fails. In the so-called confinement region ($Q^2 \lesssim 1\,\mathrm{GeV}^2$), where $\alpha_S$ is of the order of 1 or larger, phenomenological models or QCD calculations on the lattice have to be used to describe the experimental data (cf. Part II of this thesis).

Due to the fact that quarks and gluons interact, gluons dress the quarks in the nucleon with a cloud of gluons and virtual quark–antiquark pairs, so–called sea quarks. With increasing $Q^2$ the wavelength of the virtual photon decreases and the resolution of the external probing current increases. A quark which is not resolved at low $Q^2$ can therefore be resolved at larger $Q^2$ as a quark with lower momentum plus gluon (see Figure 2.4, top-panel). Hence, there is a depletion of high momentum partons and an increase in the low momentum parton distribution as $Q^2$ increases. This behaviour can be seen in Figure 2.2 where the structure function $F_2$, i.e., the sum of the distribution functions of the different quark and antiquark flavours weighted by $x$, is plotted dependent on $Q^2$ for different values of $x$. In addition, there is an enhancement of partons at small $x$ due to resolved gluons. At low $Q^2$

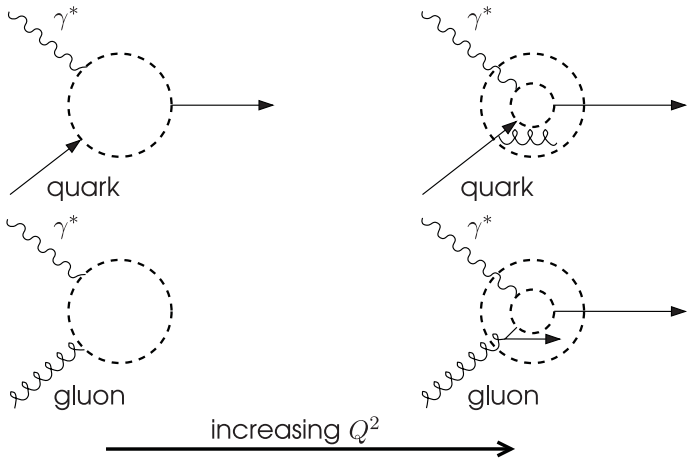


**Figure 2.4:** Improving resolution for increasing $Q^2$.

a photon does not interact with the electrically neutral gluon. With sufficient large $Q^2$ the gluon can be resolved in a quark–antiquark pair and the photon can interact with one of them (see Figure 2.4, bottom-panel).
In leading order perturbative QCD, the structure functions have the same form as in the QPM (Equations (2.1.20)–(2.1.23)):

$$F_1(x,Q^2) = \frac{1}{2}\sum_q e_q^2 q(x,Q^2) \tag{2.1.25}$$

$$g_1(x,Q^2) = \frac{1}{2}\sum_q e_q^2 \Delta q(x,Q^2) \tag{2.1.26}$$

The Callan-Gross relation in Equation (2.1.23) also holds in the so–called QCD improved QPM. Their logarithmic $Q^2$ behaviour is described by the Dokshitzer–Gribov–Lipatov–Altarelli–Parisi (DGLAP) equations [Dok77, GL72, Lip75, AP77].

## 2.2 The Structure of the Nucleon

### 2.2.1 Leading-Twist without Transverse Momenta: $q(x)$, $\Delta q(x)$ and $\delta q(x)$

The handbag diagram representing the hadronic tensor $W^{\mu\nu}$ is shown in Figure 2.5. The virtual photon is absorbed by a quark with initial four momentum p. Thus the four momentum of the outgoing quark is $k = p+q$. Neglecting quark masses, the hadronic tensor from Equation (2.1.5) can be written as [BR03]:

$$W^{\mu\nu} = \sum_{q,\bar{q}} e_q^2 \int d^4p\, \delta((p+q)^2)\, \mathrm{Tr}[\Phi\gamma^\mu(\not{p}+\not{q})\gamma^\nu], \tag{2.2.1}$$

performing the sum over the different quark and antiquark flavours, $q$ and $\bar{q}$. The quark–quark correlation matrix $\Phi_{ij}$ describes the confinement of the quarks inside the nucleon and depends on the four momentum of the quark $p$,

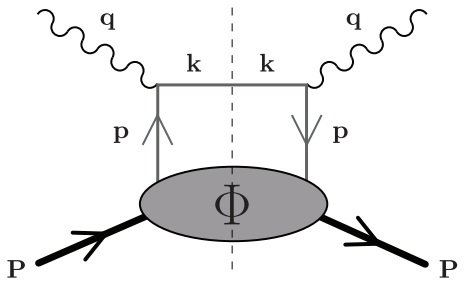


**Figure 2.5:** Handbag diagram for inclusive DIS. $\Phi$ is the quark-quark correlation matrix.

the proton $P$ and the spin of the proton $S$:

$$\Phi_{ij}(p,P,S) = \frac{1}{(2\pi)^4}\int d^4\xi\, e^{ip\cdot\xi}\langle PS|\bar{\Psi}_j(0)\Psi_i(\xi)|PS\rangle. \tag{2.2.2}$$

Here, $\Psi$ is the quark spinor with $i$, $j$ being Dirac indices. The summation over colour is not indicated for clarity. The integration is performed over all possible separations $\xi$ of the $i$th component of the quark spinor. The correlation function can be decomposed in a basis of Dirac matrices,

$$\mathbb{1},\ \gamma^\mu,\ \gamma^\mu\gamma_5,\ i\gamma_5,\ i\sigma^{\mu\nu}\gamma_5, \tag{2.2.3}$$

where $\sigma^{\mu\nu} = \frac{i}{2}[\gamma^\mu,\gamma^\nu]$:

$$\Phi(p,P,S) = \frac{1}{2}\{\mathcal{S}\mathbb{1} + \mathcal{V}_\mu\gamma^\mu + \mathcal{A}_\mu\gamma_5\gamma^\mu + i\mathcal{P}_5\gamma_5 + i\mathcal{T}_{\mu\nu}\sigma^{\mu\nu}\gamma_5\}. \tag{2.2.4}$$

The scalar $\mathcal{S}$, vector $\mathcal{V}_\mu$, axial–vector $\mathcal{A}_\mu$, tensor $\mathcal{T}_{\mu\nu}$, and pseudo–scalar $\mathcal{P}_5$ parameters depend on the vectors $p$, $P$, and $S$. They can be ordered according to powers of $1/P^+$ where the leading term is $(1/P^+)^{-1} = P^+$ and the next–to–leading term is $(1/P^+)^0 = 1$. The different powers correspond to the twist expansion according to [Jaf96], where the leading term is twist–two. If transverse momenta are neglected, in leading twist ( = twist–two), only the vector, axial–vector, and tensor components are non–zero. By the use of the following three real amplitudes $A_i(p^2, p\cdot P)$ satisfying hermiticity and parity invariance:

$$A_1(p^2,p\cdot P) = \frac{1}{2P^+}\mathrm{Tr}(\gamma^+\Phi) \tag{2.2.5}$$

$$\lambda A_2(p^2,p\cdot P) = \frac{1}{2P^+}\mathrm{Tr}(\gamma^+\gamma_5\Phi) \tag{2.2.6}$$

$$S_\perp^i A_3(p^2,p\cdot P) = \frac{1}{2P^+}\mathrm{Tr}(\gamma^+\gamma^i\Phi) \tag{2.2.7}$$

they can be expressed as follows:

$$\Phi(p,P,S) = \frac{1}{2}\{A_1(p^2,p\cdot P)\not{P} + A_2(p^2,p\cdot P)\lambda\gamma_5\not{P} + A_3(p^2,p\cdot P)\not{P}\lambda\gamma_5\not{S}_\perp\}. \tag{2.2.8}$$

where the nucleon spin is $S \approx \lambda\frac{P}{m_N} + S_\perp$ with the nucleon helicity $\lambda$. Integrating the amplitudes $A_i$ over $p$ with the constraint $x = p^+/P^+$, the three leading twist DFs are obtained:

$$q(x) = \int \frac{d^4p}{(s\pi)^4} A_1(p^2,p\cdot P)\,\delta(x - \frac{p^+}{P^+}), \tag{2.2.9}$$

$$\Delta q(x) = \int \frac{d^4p}{(s\pi)^4} A_2(p^2,p\cdot P)\,\delta(x - \frac{p^+}{P^+}), \tag{2.2.10}$$

$$\delta q(x) = \int \frac{d^4p}{(s\pi)^4} A_3(p^2,p\cdot P)\,\delta(x - \frac{p^+}{P^+}). \tag{2.2.11}$$

Here and in the following, the implicit $Q^2$ dependence of the DFs is indicated only when relevant. The integrated quark–quark correlation function over the quark momentum $p$ in leading twist then reads:

$$\Phi(x) = \frac{1}{2}\{q(x)\not{P} + \Delta q(x)\lambda\gamma_5\not{P} + \delta q(x)\not{P}\lambda\gamma_5\not{S}_\perp\}. \tag{2.2.12}$$

Integrating $\Phi(x)$ yields

$$\Phi = \frac{1}{2}\{g_V\not{P} + g_A\lambda\gamma_5\not{P} + g_T\not{P}\lambda\gamma_5\not{S}_\perp\}. \tag{2.2.13}$$

with the well-known vector charge $g_V$, the axial charge $g_A$ and $g_T$ being the tensor charge.

$$g_V = \int_{-1}^{+1} dx\,[q(x) - \bar{q}(x)], \tag{2.2.14}$$

$$g_A = \int_{-1}^{+1} dx\,[\Delta q(x) + \Delta\bar{q}(x)], \tag{2.2.15}$$

$$g_T = \int_{-1}^{+1} dx\,[\delta q(x) - \delta\bar{q}(x)]. \tag{2.2.16}$$

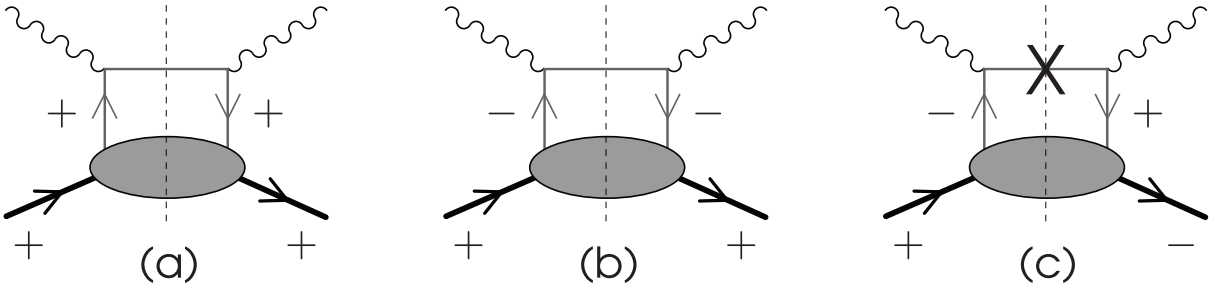


**Figure 2.6:** Handbag diagrams of the three independent configurations of quark and nucleon helicities in inclusive DIS. The configurations (a) and (b) are proportional to $q(x)$ and $\Delta q(x)$, respectively. The configuration (c), which includes helicity flips of quark and nucleon, is proportional to $\delta q(x)$ and forbidden by helicity conservation.

where use of the charge conjugation of the correlators and respectively the distributions has been made [BR03]. Since $g_V$ and $g_T$ contain the difference of quark and antiquark distributions these charges are determined by the valence quark content of the nucleon.
The obtained DFs provide, together, a complete description of the momentum and spin distributions of the quarks within the nucleon at leading-twist level. The first two were already introduced in Subsection 2.1.2: the spin-independent (or momentum) distribution $q(x)$ and the helicity distribution $\Delta q(x)$. These quantities have been measured with high accuracy by a number of experiments in the past decades. In particular the HERMES experiment has played a crucial role in the extraction of the helicity distribution, providing the most precise measurement available to date [A$^+$07a, A$^+$05a]. The third DF $\delta q(x)$, called transversity, has so far remained unmeasured due to its chiral-odd nature. A first extraction of $\delta q(x)$, based on a global fit of the data from HERMES, COMPASS and BELLE, has very recently been reported by [A$^+$07b].

### 2.2.2 Quark-Nucleon Helicity Amplitudes

In the basis of helicity eigenstates ($|+\rangle$, $|-\rangle$) (helicity basis) it is possible to define 16 different quark-nucleon forward amplitudes $A_{\Lambda\lambda,\Lambda'\lambda'}$, where $\lambda\lambda'(\Lambda\Lambda')$ represent quark (nucleon) helicity states. However, imposing helicity conservation and parity and time-reversal invariance, only three independent amplitudes survive:

$$A_{++,--}, \quad A_{+-,+-}, \quad A_{+-,-+}. \tag{2.2.17}$$

The first two are diagonal in the helicity basis, while the third is off diagonal, i.e. requires the helicity flip of the quark and the nucleon. The optical theorem allows to relate these forward quark-nucleon amplitudes to the three leading-twist parton distribution functions derived in Equations (2.2.9)–(2.2.11):

$$q(x) \propto \mathrm{Im}(A_{++,++} + A_{+-,+-}), \tag{2.2.18}$$
$$\Delta q(x) \propto \mathrm{Im}(A_{++,++} - A_{+-,+-}), \tag{2.2.19}$$
$$\delta q(x) \propto \mathrm{Im}(A_{+-,-+}). \tag{2.2.20}$$

The first two are related to the two quark helicity conserving amplitudes and can therefore be diagonalised in the helicity basis. As a consequence they have a precise probabilistic interpretation in this basis (cf. Figure 2.7): $q(x)$ reflects the probability to find quarks, within an unpolarised nucleon, carrying a fraction $x$ of its total longitudinal momentum irrespectively to the spin orientation, and $\Delta q(x)$ reflects the difference in probabilities to find, in a longitudinally polarised nucleon, quarks with their spin aligned or anti-aligned to the spin of the nucleon. Unlike $q(x)$ and $\Delta q(x)$, $\delta q(x)$, being related to a quark helicity-odd amplitude, cannot be diagonalised in the helicity basis and therefore has no probabilistic interpretation in this basis. In particular, since helicity and chirality coincide in the infinite momentum frame, since all masses can be neglected, transversity is a chiral-odd function. Therefore, since electromagnetic and strong interactions conserve chirality, transversity is not measurable in inclusive DIS processes. This can be understood since helicity is a conserved quantity for nearly massless particles and therefore a helicity flip is suppressed by a factor of $m/Q^2$ (cf. Figure 2.6).
However, in a basis of transverse spin eigenstates, which are defined as linear combinations of the helicity eigenstates

$$|\uparrow\rangle = \frac{1}{2}(|+\rangle + i|-\rangle), \quad |\downarrow\rangle = \frac{1}{2}(|+\rangle - i|-\rangle), \tag{2.2.21}$$

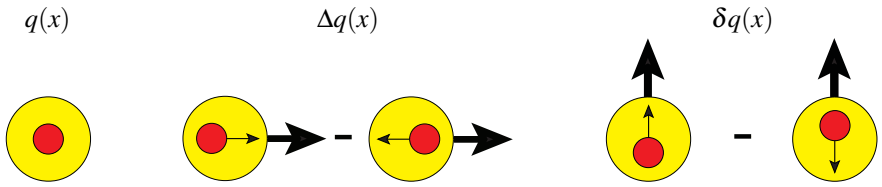


**Figure 2.7:** Probabilistic interpretation of $q(x)$, $\Delta q(x)$ and $\delta q(x)$. The arrows indicate the orientation of the spin with respect to the incident virtual photon are given for quarks (red circle) and the nucleon (yellow circle).

$\delta q(x)$ acquires a probabilistic interpretation and becomes a number density reflecting the difference in probabilities to find, in a transversely polarised nucleon, quarks with their spin aligned or anti-aligned to the spin of the nucleon (cf. Figure 2.7):

$$\delta q(x) \quad \propto \quad \mathrm{Im}(A_{\uparrow\uparrow,\uparrow\uparrow} - A_{\uparrow\downarrow,\uparrow\downarrow}). \tag{2.2.22}$$

Since the basis of transverse spin eigenstates can be transformed into the helicity basis through a simple rotation, only in relativistic regimes, where Lorentz boost and rotation do not commute, differences between $\Delta q(x)$ and $q(x)$ are expected. In addition, unlike the helicity distribution, transversity does not exist for gluons in the nucleon since a hypothetical gluon-transversity would be related to an helicity flip of the gluon-nucleon amplitude, which implies an impossible helicity flip of 2 for a spin-half target. As a consequence, the transversity is a pure valence object. This of course heavily differentiates the $Q^2$ evolution of the transversity and helicity distributions. So, even if at some scale transversity and helicity distribution would coincide, this is not necessarily the case at a different scale. More information about the anomalous dimensions of $\delta q(x)$ and the evolution of $\delta q(x)$ can be found in [AM90, BC03]. The three leading-twist parton distribution functions, which are equally important for a complete description of the momentum and spin distribution of the nucleon at leading-twist level, are related by three important bounds. From the definitions of $q(x)$, $\Delta q(x)$ and $\delta q(x)$, the relation $q(x) = q^+(x) + q^-(x) = q^\uparrow(x) + q^\downarrow(x)$ follows which immediately leads to the first two bounds:

$$|\Delta q(x)| \leq q(x), \quad |\delta q(x)| \leq q(x). \tag{2.2.23}$$

The third, more subtle, bound is known as the Soffer inequality [Sof95]:

$$\delta q(x) \leq \frac{1}{2}(\Delta q(x) + q(x)). \tag{2.2.24}$$

The Soffer inequality is more complicated because the three quantities are not diagonal in the same basis. All three inequalities are preserved by QCD evolution.

### 2.2.3 Transverse Momentum Dependent Distribution Functions

So far the quark transverse momentum $\vec{p}_T$ has been neglected because it is small compared to the longitudinal component. Nevertheless, it remains unchanged by the quark–parton interaction and influences the final momenta of the produced hadrons. For the analysis of semi–inclusive DIS on a transversely polarised target, it will be therefore necessary to consider also quark transverse–momentum dependent DFs. Taking into account non–zero $\vec{p}_T$, in leading twist additional amplitudes $A_i$ appear in the vector $\mathcal{V}_\mu$, axial–vector $\mathcal{A}_\mu$, tensor $\mathcal{T}_{\mu\nu}$ component of the correlation function $\Phi$. All amplitudes are related to eight different $\vec{p}_T$–dependent DFs [MT96]. The functions can be grouped according to their behaviour under chirality and time–reversal operations. Integrating the DFs over the transverse momentum of the quark, most of the functions vanish and the three DFs (2.2.9)–(2.2.11) are retrieved:

$$q(x) = \int d^2\vec{p}_T \, q(x, p_T^2), \tag{2.2.25}$$

$$\Delta q(x) = \int d^2\vec{p}_T \, \Delta q(x, p_T^2), \tag{2.2.26}$$

$$\delta q(x) = \int d^2\vec{p}_T \, \delta q(x, p_T^2). \tag{2.2.27}$$

It is convenient to express integrated cross sections in terms of the following moments of any DF $d_q(x,p_T^2)$:

$$d^{(1/2)q}(x,p_T^2) \equiv \int d^2\vec{p}_T\, d^{(1/2)q}(x,p_T^2) \equiv \int d^2\vec{p}_T \left(\frac{|\vec{p}_T|}{2m_N}\right) d^q(x,p_T^2), \tag{2.2.28}$$

$$d^{(n)q}(x,p_T^2) \equiv \int d^2\vec{p}_T\, d^{(n)q}(x,p_T^2) \equiv \int d^2\vec{p}_T \left(\frac{p_T^2}{2m_N^2}\right) d^q(x,p_T^2), \tag{2.2.29}$$

for integer values $n$.
In the following we want to focus on the chiral-even, naïve T-odd distributions function $f_{1T}^{\perp q}(x,p_T^2)$, termed Sivers DF. DFs which violate time-reversal invariance do not contribute to final cross sections. Since the Sivers DF is a naïve T-odd DF, it can be accessible by the measurement of asymmetries. Poperties of naïve T-odd DF are the subject of the follwing subsection.

### 2.2.4 Gauge Link and naïve T–Odd Distribution Functions

In QCD, a path–dependent link operator $\mathcal{L}$ must be inserted between the quark fields to obtain a gauge invariant correlation function $\Phi$ [BM00, EFP83] (cf. Equation (2.2.2)):

$$\Phi_{ij}(p,P,S) = \frac{1}{(2\pi)^4}\int d^4\xi\, e^{ip\cdot\xi}\langle PS|\bar{\Psi}_j(0)\mathcal{L}(0,\xi)\Psi_i(\xi)|PS\rangle. \tag{2.2.30}$$

The gauge link $\mathcal{L}$, which is also called Wilson line,

$$\mathcal{L}(0,\xi) = \mathcal{P}\left\{exp\Big(-i\sqrt{4\pi\alpha_S}\int_0^\xi ds^\mu A_\mu(s)\Big)\right\} \tag{2.2.31}$$

is a bilocal operator connecting the quark fields $\Psi$ in two different points in space and time, 0 and $\xi$. Here, $\mathcal{P}$ indicates the path–ordering of the integral over the gauge field $A_\mu$. The Wilson line corresponds to the summation of all diagrams with soft gluon exchange. As example, the handbag diagram for one–gluon exchange is shown in Figure 2.8. In the light–cone gauge ($A^+ = 0$) the gauge link is equal to unity for $\xi_T = 0$ and was therefore neglected so far.

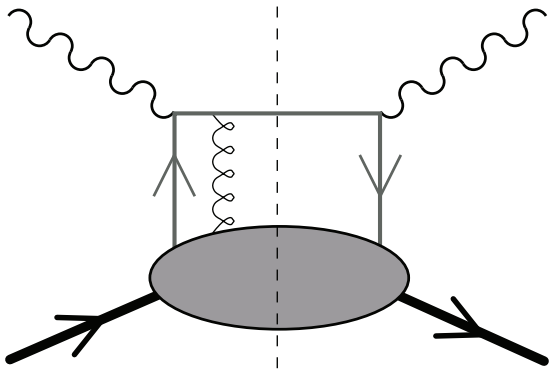

**Figure 2.8:** The handbag diagram with one additional gluon exchanged between quark line and the nucleon remnant.

The Wilson line plays an important role for the existence of time-reversal odd (T-odd) DFs. Invariance under the time-reversal operation which transforms initial states into final states, implies the following constraint on the correlation function $\Phi$ [BR03]:

$$\Phi^*(p,P,S) = \gamma_5 C\Phi(\widetilde{p},\widetilde{P},\widetilde{S})C^\dagger\gamma_5 \tag{2.2.32}$$

where $C = i\gamma^2\gamma^0$ and the tilde four-vectors are defined as $\widetilde{p}^\mu = (p^0,-\vec{p})$. T-odd terms in $\Phi$ will change sign on the left hand side and are therefore forbidden. With the insertion of $\mathcal{L}$ in $\Phi$, time-reversal invariance does not constrain the T-odd Sivers DF $f_{1T}^{\perp q}(x,p_T^2)$ in leading twist to be zero but gives a relation between processes that probe Wilson lines pointing in opposite directions [Col02]. A very comprehensive approach to this feasible topic is given in [Siv06].
Figure 2.8 can also be interpreted in terms of final–state interactions (FSI) via soft gluons [Col02]. The colliding particles interact strongly with non–trivial relative phases and the transformation of interacting final states into

initial states is not as simple as for non–interacting final states. Therefore, time–reversal invariance cannot be implemented by naïvely imposing the condition 2.2.32. T–odd, rather than violating time–reversal invariance, means that the condition in Equation (2.2.32) is not satisfied and is often referred to as naïve T–odd.

### 2.2.5 The Sivers Distribution Function

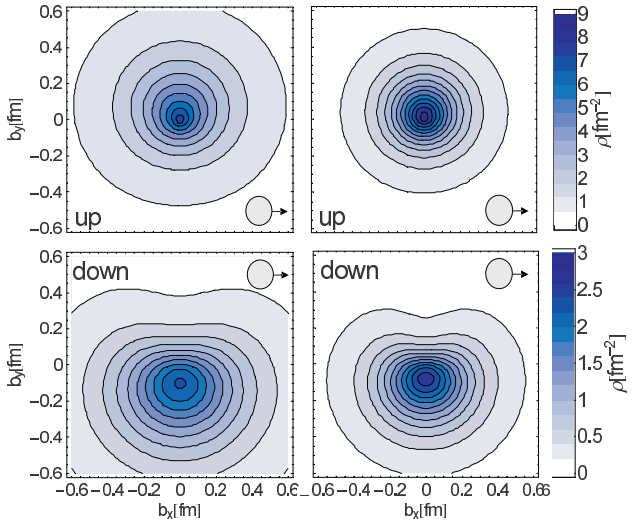


**Figure 2.9:** Geometrical interpretation of the Sivers DF $f_{1T}^{\perp q}(x,p_T^2)$: Densities of unpolarised quarks in transversely polarised nucleon for up (upper plots) and down (lower plots) quarks. The outer arrows indicate respectively the quarks transverse polarisation. **Left-panel**: Lowest moment $n=1$ (cf. Equation (2.2.29)). **Right-panel**: second moment, $n=1$ (cf. Equation (2.2.29)).

The naïve T-odd, chiral-even DF $f_{1T}^{\perp q}(x,p_T^2)$ was first proposed by Sivers [Siv90, Siv91] to explain single-spin asymmetries observed in pion production in proton-proton scattering. It is hence referred to as the Sivers function. This DF describes the correlation between the intrinsic transverse momentum of the quarks and the transverse polarisation of the nucleon (cf. Figure 2.4.3). An interesting prerequisite for a non-zero Sivers function is the existence of orbital angular momentum of the quarks, contributing to the spin of the nucleon [BHS02, Bur04]. As explained in the following, in a semi-classical picture these asymmetries arise from the combination of a spatial distortion of the DFs in the transverse position space together with one gluon exchange FSI, that bends the struck quark in a fixed direction. In the transverse position space representation, the DFs are expressed in terms of the impact parameter $b_\perp$ [Bur02], which is the transverse distance of the quark to the transverse center of momentum. Assuming a non-zero quarks orbital angular momentum (OAM), if the quarks are unpolarised and the nucleon is unpolarised or longitudinally polarised, all the orientations of the OAM are equally likely so that the quark distribution is axially symmetric. On the contrary, when a transverse nucleon (Sivers) polarisation is involved, spin-orbit correlations give origin to a spatial distortion of the quark densities, which appears enhanced on one side or another depending on the OAM orientation, as in Figure 2.9, where the displacement was obtained by a lattice simulation of our Regensburg Group [G$^+$07]. In this representation, when the quark is knocked out from the target, it is still subject to the attractive field of the remaining quarks from the nucleon (spectators), therefore it would experience FSI that deflects the struck quark towards the center of momentum before its fragmentation. In this way the FSI can translate the initial quark transverse position asymmetry into the outgoing quark transverse momentum asymmetry. In conclusion spin-orbit correlations together with attractive final state interactions in a semi-classical framework give rise to a non-zero Sivers function with opposite sign for the up and down quarks.

In order to be consistent with the previous paragraphs, we want to show, how the Sivers DF can be obtained from the correlation matrix $\Phi$ [BM98]. Since it gives the probability to find an unpolarised quark in a transversely polarised nucleon (cf. Figure 2.10) it is part of the $\gamma^+$ trace of the quark correlation matrix:

$$\frac{1}{2}\int \frac{dp^+dp^-}{(2\pi)^4}\,\mathrm{Tr}(\gamma^+\Phi)\delta(p^+-xP^+) = \ldots - \frac{\varepsilon_\perp^{ij}p_{Ti}S_{Tj}}{m_N} f_{1T}^{\perp q}(x,p_T^2) \tag{2.2.33}$$

Following the Trento conventions [BDDM04] the distribution of unpolarised quarks in a polarised proton is given

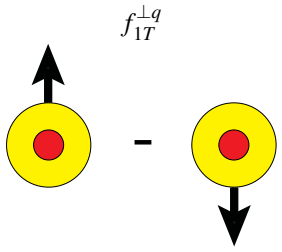


**Figure 2.10:** The probabilistic interpretation of the naïve T-odd, chiral-even Sivers DF. It is one of the leading twist transverse–momentum dependent quark distribution functions. The Sivers DF depends on $x$ and $p_T^2 = |\vec{p}_T|^2$.

by:

$$f_{q/p^\uparrow}(x, p_T) = f_1^q(x, p_T^2) - f_{1T}^{\perp q}(x, p_T^2) \frac{\varepsilon^{\mu\nu\rho\sigma} P_\mu k_\nu S_\rho n_\sigma}{m_N (P \cdot n)} \tag{2.2.34}$$

$$= f_1^q(x, p_T^2) - f_{1T}^{\perp q}(x, p_T^2) \frac{(\widehat{P} \times \vec{p}_t) \cdot \vec{S}}{m_N}, \tag{2.2.35}$$

where $f_1^q$ is the unpolarised quark density and $f_{1T}^{\perp q}$ determines the Sivers effect. Here $\widehat{P}$ is the momentum of the proton (unity vector), $\vec{S}$ is its spin vector and $m_N$ is the mass of the proton. We can see that the inclusion of transverse momenta of quark quarks gives rise to a sine modulation, which originates from the cross product in Equation (2.2.35).

### 2.2.6 The Collins Fragmentation Function

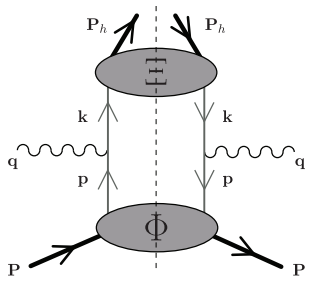


**Figure 2.11:** Extended handbag diagram for Semi–Inclusive DIS.

The Collins FF $H_1^{\perp q \to h}$ describes how the transversely polarised struck quark fragments in the final observed hadron. Beyond being T-odd, $H_1^{\perp q \to h}$ is a chiral-odd function, therefore can be measured only in conjunction with another chiral-odd object, since QCD and hard scattering preserve chirality. One of the experimental way to access the Collins FF is the measurement of Collins asymmetry in SIDIS, in which $H_1^{\perp q \to h}$ is probed in conjunction with the chiral-odd transversity DF, describing transversely polarised quark distribution in a transversely polarised nucleon. Details of such asymmetries are discussed in the next paragraph.

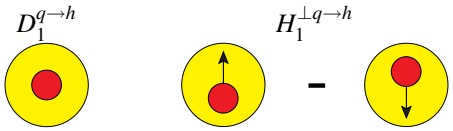


**Figure 2.12:** Leading twist transverse–momentum dependent quark fragmentation functions independent of the produced hadron spin. Both FFs depend on $z$ and $z^2 k_T^2$. The struck quark (produced hadron) is indicated as a red (yellow) circle.

The theoretical deduction is very similar to the case of the Sivers DF. First, one introduces a fragmentation matrix $\Xi$ (cf. Figure 2.11) which is defined in a very similar way to the quark-quark correlation matrix $\Phi$ containing the

quark distribution functions. Similar to the classification of the distribution functions in the quark-quark correlator it is then possible to classify the different fragmentation functions by traces over the according Lorenz projectors acting on the fragmentation matrix.
The resulting two leading twist fragmentation functions are the well known unpolarised FF $D_1^{q\to h}$ which describes the probability for a quark to fragment into a hadron with a certain fraction $z$ of the virtual photon's energy and with transverse momentum $z^2k_T^2$ (where $\vec{k}_T^2 = k_T^2$ is the **final** squared intrinsic transverse momentum of the struck quark), and the Collins FF $H_1^{\perp q\to h}$, which gives the probability for a transversely polarised quark to fragment in an unpolarised hadron. During the fragmentation process the fragmenting hadron gained intrinsic transverse momentum $\vec{P}_{h\perp} = -z\vec{k}_T$. As previously anticipated, the Collins function is chiral-odd, therefore it can be measured only in conjunction with another chiral-odd functions, as the transversity DF $\delta q(x)$. Figure 2.12 shows the probabilistic interpretation of the two DFs.

### 2.2.7 Cross Sections and Azimuthal Asymmetry Moments in Semi-Inclusive DIS

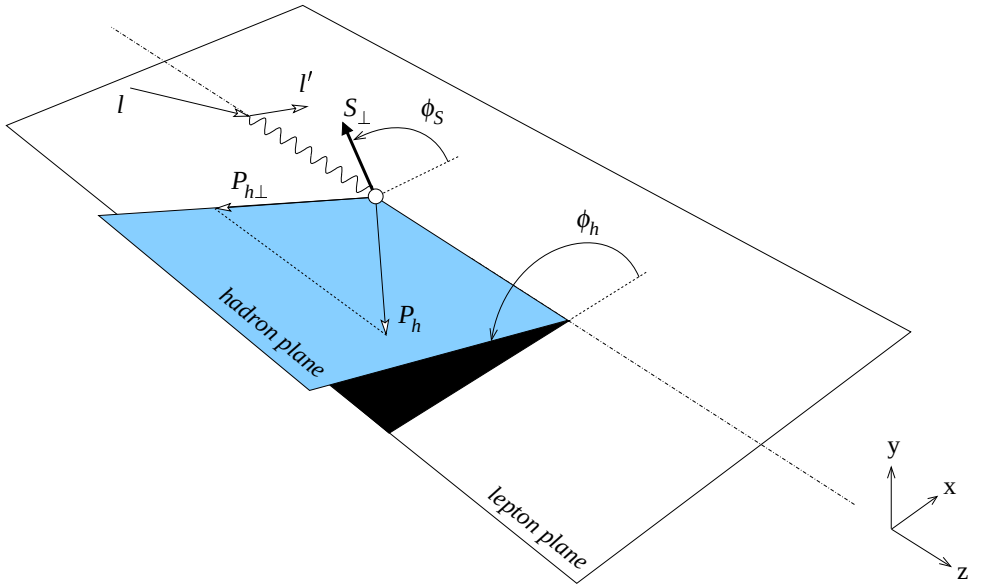


**Figure 2.13:** Definition of the azimuthal angles $\phi$ and $\phi_S$ folloing the Trento conventions [BDDM04]

In a very general description of semi-inclusive processes one has to include the transverse momentum of the hadrons resulting in a 6-fold differential cross section [Bac02]:

$$d^6\sigma \equiv \frac{d^6\sigma}{dx\,dy\,dz\,d\phi_S\,d^2\vec{P}_{h\perp}}. \tag{2.2.36}$$

Here, $\vec{P}_{h\perp}$ is the transverse momentum of the produced hadron and $|\vec{P}_{h\perp}|^2 = P_{h\perp}^2$ must be small compared to $Q^2$ to avoid the introduction of further hard scales [Bac02]. The azimuthal angle $\phi_S$ is defined as the angle around the virtual photon between the target spin $S_T$ and the plane spanned by the incoming and outgoing lepton, as depicted in Figure 2.13 (the angle $\phi_S$ is also called Collins angle refering to [CHL94]). It is convenient to split the cross section into unpolarised and polarised terms:

$$d^6\sigma = d^6\sigma_{UU} + d^6\sigma_{LU} + d^6\sigma_{UL} + d^6\sigma_{LL} + d^6\sigma_{UT} + d^6\sigma_{LT} \tag{2.2.37}$$

Two subscripts are used to indicate beam and target polarisation where $U$ means unpolarised, $L$ longitudinally polarised, and $T$ transversely polarised. Here and in the following, the differential kinematic variables are omitted for clarity. The unpolarised cross section in leading twist contains two products of DF and FF [Bac02]:

$$\begin{aligned} d^6\sigma_{UU} = \frac{2\alpha^2}{sxy^2}\Big\{ & A(y)\sum_{q,\bar{q}} e_q^2\,\mathcal{I}\left(q(x,p_T^2)D_1^q(z,z^2k_T^2)\right) - \\ & B(y)\cos(2\phi)\sum_{q,\bar{q}} e_q^2\,\mathcal{I}\left(\frac{2(\vec{p}_T\cdot\widehat{P}_{h\perp})(\vec{k}_T\cdot\widehat{P}_{h\perp}) - \vec{p}_T\cdot\vec{k}_T}{m_N m_h} h_1^{\perp q}(x,p_T^2)H_1^{\perp}(z,z^2k_T^2)\right)\Big\}, \end{aligned} \tag{2.2.38}$$

where $m_h$ is the mass of the produced hadron and $\widehat{P}_{h\perp}$ is the unit vector of the hadron transverse momentum. The two products of DF and FF appear in the integral,

$$\mathcal{I}[\mathcal{W}\cdot\mathcal{D}\cdot\mathcal{F}] \equiv \int d^2\vec{p}_T\, d^2\vec{k}_T\, \delta\left(\vec{p}_T - \frac{\vec{P}_{h\perp}}{z} - \vec{k}_T\right) \mathcal{W}\cdot\mathcal{D}\cdot\mathcal{F} \tag{2.2.39}$$

defined for any combination of DF $\mathcal{D}$ and FF $\mathcal{F}$ multiplied by the weight $\mathcal{W}$ dependent on $\vec{P}_{h\perp}$, $\vec{p}_T$, $\vec{k}_T$, $x$ and $z$. The kinematic factors $A(y)$ and $B(y)$ used later are defined as

$$A(y) = 1 - y + \frac{y^2}{2} \tag{2.2.40}$$

$$B(y) = 1 - y. \tag{2.2.41}$$

Now, different azimuthal modulations of the unpolarised and polarised cross–section terms can be constructed by:

$$d^6\sigma_{\text{Beam Target}} = \frac{2\alpha^2}{sxy^2} \quad\cdot\quad \text{factor} \quad\cdot\quad \text{modulation} \quad\cdot\quad \sum_{q,\bar{q}} e_q^2\, \mathcal{I}\left[\mathcal{W}\cdot\mathcal{D}\cdot\mathcal{F}\right]. \tag{2.2.42}$$

All twist–two and twist–three cross–section terms can be found for instance in [MT96, BM98, BMP04]. The product of the transversity DF and the Collins FF appears as a $\sin(\phi+\phi_S)$ modulation in the polarised cross section for an unpolarised beam and a transversely polarised target:

$$d^6\sigma_{UT} = -\frac{2\alpha^2}{sxy^2}\,|\vec{S}_T|\,B(y)\,\sin(\phi+\phi_S)\sum_{q,\bar{q}} e_q^2\,\mathcal{I}\left[\frac{\vec{k}_T\cdot\vec{P}_{h\perp}}{m_h}\,\delta q(x,p_T^2)\,H_1^{\perp}(z,z^2k_T^2)\right]. \tag{2.2.43}$$

The same polarised cross section exhibits also a $sin(\phi-\phi_S)$ modulation proportional to the product of the Sivers function and the unpolarised FF:

$$d^6\sigma_{UT} = -\frac{2\alpha^2}{sxy^2}\,|\vec{S}_T|\,A(y)\,\sin(\phi-\phi_S)\sum_{q,\bar{q}} e_q^2\,\mathcal{I}\left[\frac{\vec{p}_T\cdot\vec{P}_{h\perp}}{m_N}\,f_{1T}^{\perp q}(x,p_T^2)\,D_1^q(z,z^2k_T^2)\right]. \tag{2.2.44}$$

Experimentally the measurement of cross–section asymmetries is preferred over the measurement of absolute cross sections or differences thereof as many uncertainties cancel for asymmetry measurements. In order to extract the individual products $\mathcal{D}\cdot\mathcal{F}$ with different azimuthal modulations in the cross section, it is common to measure azimuthal moments:

$$\langle\sin(n\phi+m\phi_s)\rangle_{\text{Beam Target}}(x,y,z) \equiv \frac{\int d\phi_S\, d^2\vec{P}_{h\perp}\,\sin(n\phi+m\phi_s)\,d^6\sigma_{\text{Beam Target}}}{\int d\phi_S\, d^2\vec{P}_{h\perp}\, d^6\sigma_{UU}}, \tag{2.2.45}$$

where $m$ and $n$ can be negative or positive. For the separation of the individual polarised cross–section terms, cross–section differences of opposite spin states are formed in which the unpolarised cross–section component cancels. In our case that is $d^6\sigma_{UT} \equiv \frac{1}{2}(d^6\sigma_{U\uparrow} - d^6\sigma_{U\downarrow})$, where the arrows show the direction of the spin orientation, which can be parallel $\uparrow$ and antiparallel $\downarrow$ to the direction specified by the angle $\phi_S$.
The so–called Collins moment,

$$\langle\sin(\phi+\phi_s)\rangle_{UT} = -|\vec{S}_T|\,\frac{\frac{1}{xy^2}B(y)\sum_{q,\bar{q}} e_q^2\int d^2\vec{P}_{h\perp}\,\mathcal{I}\left[\frac{\vec{k}_T\cdot\vec{P}_{h\perp}}{m_h}\,\delta q(x,p_T^2)\,H_1^{\perp}(z,z^2k_T^2)\right]}{2\,\frac{1}{xy^2}A(y)\sum_{q,\bar{q}} e_q^2\,q(x,p_T^2)D_1^q(z,z^2k_T^2)} \tag{2.2.46}$$

gives access to transversity and the Collins function. The factor 2 in the denominator remains of the integration over the angle $\phi_S$. Unfortunately, the product $\delta q\cdot H_1^{\perp}$ is still embedded in a convolution integral over the transverse momenta of the initial and final quarks and of the produced hadron. The integral cannot be factorised like in the case of the product of unpolarised DF and FF because of the weight $\mathcal{W} = \frac{\vec{k}_T\cdot\vec{P}_{h\perp}}{m_h}$. One ansatz to solve the integral is to assume Gaussian transverse momentum distributions in the DF and FF [Bac02]. With this Gaussian ansatz, transversity and Collins function factorise in the Collins moment:

$$\langle\sin(\phi+\phi_S)\rangle_{UT} = \frac{|\vec{S}_T|}{\sqrt{1+z^2\langle p_T^2\rangle/\langle K_T^2\rangle}}\,\frac{\frac{1}{xy^2}B(y)\sum_{q,\bar{q}} e_q^2\,\delta q(x)\,H_1^{\perp(1/2)}(z)}{2\,\frac{1}{xy^2}A(y)\sum_{q,\bar{q}} e_q^2\,q(x)\,D_1^q(z)} \tag{2.2.47}$$

A different ansatz which avoids any assumption on the transverse momentum distributions, includes $P_{h\perp}$ in the convolution integral for cross section terms with a weight $\mathcal{W}$ proportional to $\widehat{P}_{h\perp}$. In case of the $\sin(\phi+\phi_S)$ modulation, this yields the $P_{h\perp}$ weighted Collins moment:

$$\langle \sin(\phi+\phi_S)\rangle_{UT} = |\vec{S}_T| \frac{\frac{1}{xy^2}B(y)\sum_{q,\bar{q}} e_q^2\,\delta q(x)\,H_1^{\perp(1)}(z)}{2\frac{1}{xy^2}A(y)\sum_{q,\bar{q}} e_q^2\,q(x)\,D_1^q(z)}. \tag{2.2.48}$$

The combination of Sivers function and unpolarised FF can be extracted from the unweighted and $P_{h\perp}$ weighted Sivers moments:

$$\langle \sin(\phi+\phi_S)\rangle_{UT} = -\frac{|\vec{S}_T|}{\sqrt{1+z^2\langle K_T^2\rangle/(z^2\langle p_T^2\rangle)}} \frac{\frac{1}{xy^2}A(y)\sum_{q,\bar{q}} e_q^2\,f_{1T}^{\perp(1/2)q}(x)\,D_1^q(z)}{2\frac{1}{xy^2}A(y)\sum_{q,\bar{q}} e_q^2\,q(x)\,D_1^q(z)}, \tag{2.2.49}$$

$$\langle \sin(\phi-\phi_S)\rangle_{UT} = -|\vec{S}_T| \frac{\frac{1}{xy^2}B(y)\sum_{q,\bar{q}} e_q^2\,f_{1T}^{\perp(1)q}(x)\,D_1^q(z)}{2\frac{1}{xy^2}A(y)\sum_{q,\bar{q}} e_q^2\,q(x)\,D_1^q(z)}. \tag{2.2.50}$$

Note that the factor $\frac{1}{xy^2}A(y)$ may not cancel because numerator and denominator are integrated separately over certain $x$ and $y$ ranges in a measurement. Since the Collins and Sivers functions appear in the above introduced azimuthal asymmetry moments, the possible existence of these asymmetrymoments are often referred to as Collins and Sivers effect, respectively. Latest results on the Sivers- and Collins-moments at HERMES are shown in Figure 2.15 and 2.14 taken from [Die07].

The factorisation of the cross section into the contributions of long–distance and short–distance interaction which allows the application of perturbative calculations, was proven for transverse–momentum independent functions in leading twist already in the 1980s [CSS88]. Only recently proofs were published for the factorisation of twist–two transverse momentum dependent functions at low transverse momenta in semi–inclusive DIS and Drell–Yan [JMY04, JMY05]. Whether factorisation holds also for subleading twist is still unclear. The appearance of the functions under the convolution integral and the inclusion of gauge links is challenging. in [JMY05], the equivalence of hte Twist-three and TMD approach has been shown.

As a consequence of factorisation, universality for twist–two transverse–momentum integrated functions was proven in the 1980s [CSS88]. The proof of universality for transverse–momentum dependent functions was only recently established for T–even functions [CM04]. For twist–two T–odd transverse–momentum dependent DFs, a sign–change between the semi–inclusive DIS and the DY processes,

$$f_{1T}^{\perp q}(x,Q^2)|_{(DIS)} = -f_{1T}^{\perp q}(x,Q^2)|_{(DY)} \tag{2.2.51}$$

is caused by the Wilson line [Col02]. This gauge link which is necessary to allow T–odd functions, is past–pointing in the DY process contrary to the future–pointing Wilson line in the semi–inclusive DIS process.

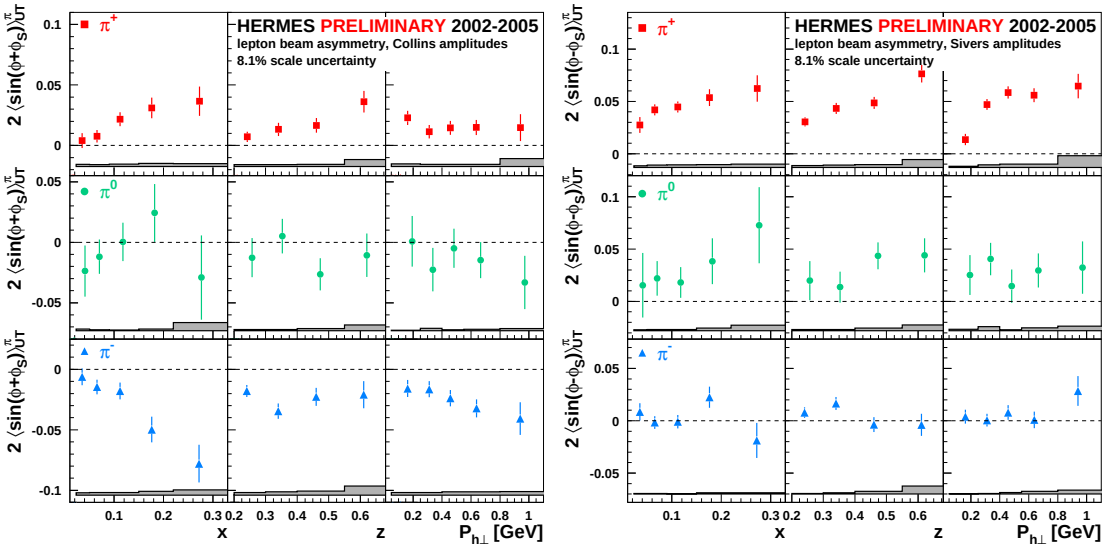


**Figure 2.14:** Collins amplitudes (left column) and Sivers amplitudes (right column) for $\pi$-mesons (as labelled) as function of $x$, $z$ and $P_{h\perp}$. The error bands represent the maximal systematic uncertainty; the common overall 8.1% scaling uncertainty is due to the target polarisation uncertainty.

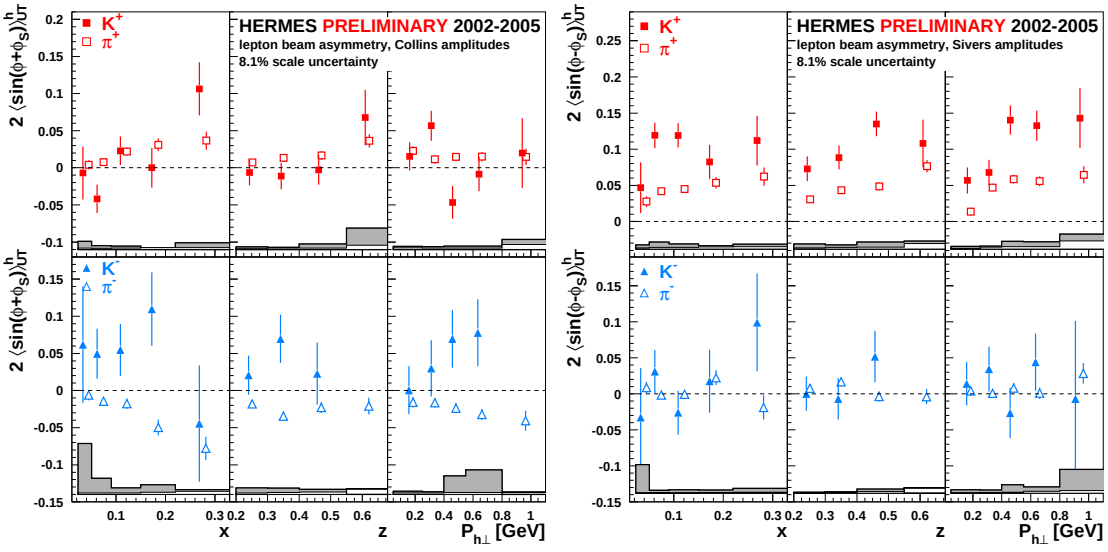


**Figure 2.15:** Collins amplitudes (left column) and Sivers amplitudes (right column) for charged kaons (closed symbols, as labelled) and charged pions (open symbols, as labelled) as function of $x$, $z$ and $P_{h\perp}$. The error bands represent the maximal systematic uncertainty; the common overall 8.1% scaling uncertainty is due to the target polarisation uncertainty.

## 2.3 SSAs in $lp^{\uparrow} \to hX$ and $p^{\uparrow}p \to hX$ Processes

SSAs on a transversely polarised target provide us with rich information on the spin structure of the nucleon, especially on the transverse spin. However, there has been a prejudice that all transverse spin effects should be suppressed at high energies in the past. It was not until in the 1990s, when the E704 Collaboration reported their observation of a left-right asymmetry in $p^{\uparrow}p \to \pi X$ processes. Earlier experiments studied polarised proton collisions $p^{\uparrow}p$ at center of-mass energies $\sqrt{s} \leq 20\,\text{GeV}$ and measured $A_N$ for pion production at moderate transverse momentum $0.5 \leq P_{h\perp} \leq 2.0\,\text{GeV}$. Contrary to the naïve expectation, $A_N$ was found to be 20%–40% for pions produced at large values of Feynman $x$ ($x_F = 2p_L/\sqrt{s}$, where $p_L$ is the longitudinal momentum of the pion) [A$^+$92b, A$^+$92a, A$^+$91, A$^+$04, B$^+$88, B$^+$96, K$^+$76, K$^+$99, S$^+$90]. In [A$^+$06], it was pointed that the Sivers effect is the dominant effect among the Collins and Boer-Mulder-Effect. Similarly, semi-inclusive deep-inelastic lepton scattering experiments [A$^+$00, Bra99] have reported transverse single-spin asymmetries which differ significantly from zero. These results have sparked substantial theoretical activity to understand transverse spin effects within the framework of pQCD.

Due to the complexity of the hadron–hadron process, theorists might as well turn their point to a simpler process, the semi-inclusive deep inelastic scattering (SIDIS) process, which has attracted many interests in recent years [SMM08]. The authors in [SMM08] have analysed the basic quantity of left–right asymmetry in SIDIS processes, following the analysing method of the E704 experiment, in which no weighting functions were multiplied, to see whether a non-zero asymmetry can be obtained (in contrast to the extraction method of Collins- and Sivers-Mometns described above). The "E704" analysing power $A_N$ is defined as:

$$A_N = -\frac{1}{P_B \langle \cos(\phi) \rangle} \frac{N_{\uparrow}(\phi) - N_{\downarrow}(\phi)}{N_{\uparrow}(\phi) + N_{\downarrow}(\phi)}, \tag{2.3.1}$$

where $P_B$ is the beam polarization and $\phi$ is the azimuthal angle between the beam polarisation direction and the normal to the pion-production plane. $N_{\downarrow(\uparrow)}$ is the number of pions produced for the beam spin tagged as positive (negative) normalised to the beam flux. $\phi$ ranges from $-\frac{\pi}{4}$ to $\frac{\pi}{4}$, i.e. only the hadrons produced in a range to the left (right) of the spin plane will be selected. This detection region changes from left (right) to right (left) as the target spin changes from up to down, thus a left–right asymmetry is obtained.

With the current theoretical knowledge, the authors in [SMM08] showed that the Sivers effect plays a key role for SSAs in the $ep^{\uparrow} \to hX$ process and indeed produces a sizable left–right asymmetry in $\pi^{\pm}$ production processes. This is one of the motivations for this thesis, since experimental results can provide data to support their investigation of theoretical studies.

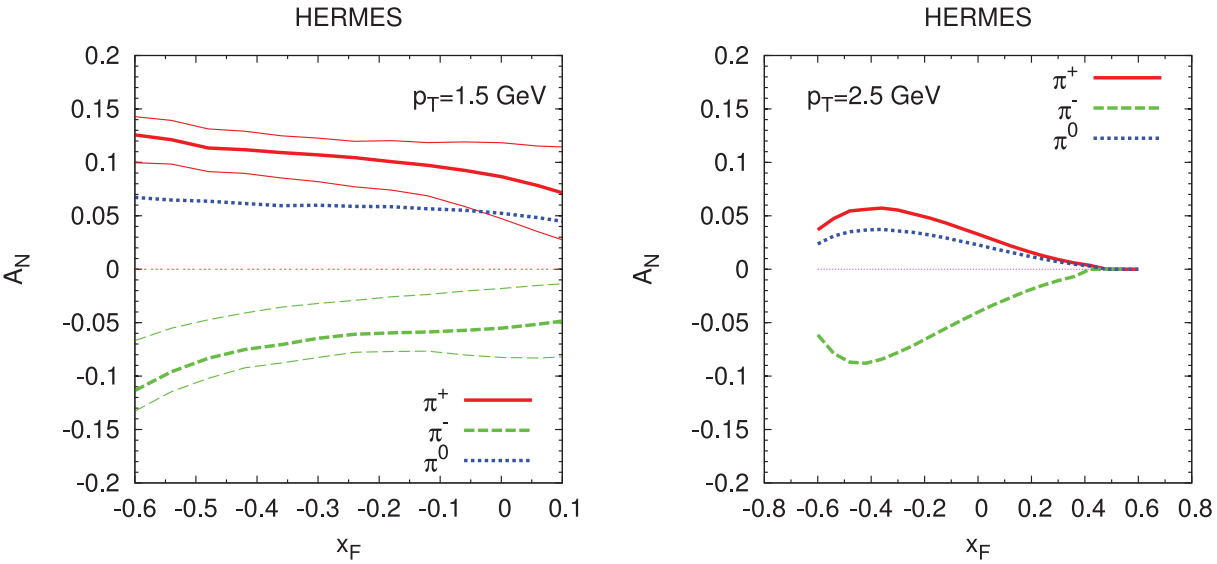


**Figure 2.16:** Predictions for the contribution of the Sivers effect to the analysing power $A_N$ in $lp^{\uparrow} \to \pi X$-processes for $P_{h\perp} = 1.5\,\text{GeV}$ (left) and $P_{h\perp} = 2.5\,\text{GeV}$ (right)

Furthermore, Anselmino et al. studied the analysing power $A_N$ in "inclusive" pion-production $lp^{\uparrow} \to \pi^{\pm} X$ [ABM$^+$09]. The authors' motivation is that a one-scale process, like inclusive meson production, can probe sub-leading-twist

effects in SSAs. SSAs in these processes can thus serve as a check for TMD factorisation and universality. In agreement with [SMM08], they claim that also in inclusive hadron prodcution the Sivers-mechanism should dominate the Collins-effect. Figure 2.16 shows the impact of the Sivers-effect on the anaylsing power $A_N$. For the region around $P_{h\perp} = 1.5\,\text{GeV}$, the model predicts asymmetries of $\sim 10\%$ for positive pions, and relatively large negative asymmetries for negative pions, though. Large $\pi^-$-asymmetries obvously contradict the HERMES results on the Sivers-moments which show clear positive SSAs for the Sivers amplitudes of positively charged mesons and asymmetries compatible with zero for negatively charged hadrons (cf. Figures 2.15 and 2.14).
We emphasize that the predictions of Anselmino et al. for SSAs in $lp^{\uparrow} \rightarrow \pi^{\pm}X$ prcesses are somewhat suprisig from different points of views. First, the predicted SSAs could be potentially compensated by the Collins-mechanism which is nearly equally dominant within the acceptance of the HERMES spectrometer. Second, in purely inclusive measurements of mesons, it is impossible to restrict the hadron sample to a clear kinematic regime. Thus contributions from photoproduction processes (where $Q^2 \approx 0$) dominate statsistics due to the $Q^{-4}$-proportionality of the DIS cross section. So far, no azimuthal SSAs in the photoproduction regime have been measured. One would naïvely assume, that these processes should eliminate the significant asymmetries caused by the Sivers-Effect.

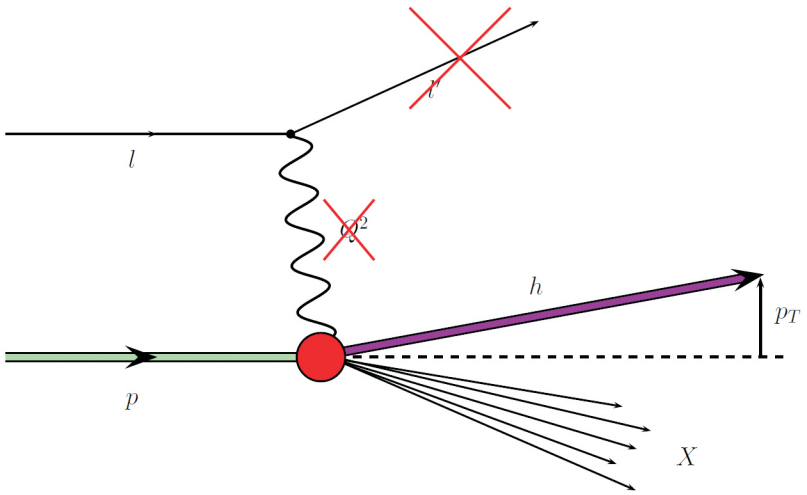


**Figure 2.17:** Schematic overview of a purely inclusive measurement of hadrons in a DIS process.

It is very important to mention that by a purely inclusive measurement of hadrons in a DIS experiment like HERMES all information about the virtual photon is lost. This has dramatic consequences on the theoretical description of the process, as the only kinematic variable, which can be accessed, is the hadron's momentum. Thus one has to be aware of the changes of the underlying kinematics. The changes arising from a purely inclusive measurement of mesons are summarised and compared to SIDIS-kinematics in Table 2.3 and Figure 2.17.

| | $lp^{\uparrow} \to lh^{\pm}X$ | $lp^{\uparrow} \to h^{\pm}X$ |
|---|---|---|
| Scale(s) | $Q^2$, $P_{h\perp}$ | $P_{h\perp}$ |
| Construction-frame of $\vec{P}_{h\perp}$ | $\gamma^* p$ | $lp$ |
| Magnitude of $Q^2$ | $Q^2 > 1\,\mathrm{GeV}^2$ | $Q^2 \approx 0\,\mathrm{GeV}^2$ |
| Magnitude of $\theta$ ($\sin^2(\frac{\theta}{2}) \overset{lab}{\propto} Q^2$) | full range | small |
| Scaling variables | $x_F$, $x_B$ | "poor man's" $x_F = \lvert\vec{P}_{h,z}\rvert / E_{Beam}$ |
| Factorisation | valid for $P_{h\perp}^2 \ll Q^2$ | eventually valid for $1\,\mathrm{GeV} < P_{h\perp}$ |

**Table 2.2:** Overview over the the kinematics in $lp^{\uparrow} \to hX$-processes and the changes compared to Semi-Inclusive DIS.

# Chapter 3

# The HERMES Experiment

This chapter is intended to provide the necessary introduction to the experimental setup with which the data analysed in the following chapters were produced. As we intend to measure azimuthal asymmetry moments the HERMES ("HERA Measurement of Spin") experiment essentially needs three main ingredients. In our case these are a high-energy unpolarised lepton beam, a polarised nucleon target, and a spectrometer with reasonable particle identification and tracking resolution. In the following the various components which used in the HERMES experiment and are relevant for our analysis are beeing described. We will mainly refer to [A$^+$98a].

## 3.1 The HERA Lepton Beam

The HERMES experiment was operated in the east hall of the storage ring facility HERA ("Hadron-Elektron Ringanlage"), which was part of the DESY accelerator complex located in Hamburg. In the two HERA rings sharing a tunnel with a circumference of 6.3 km a lepton beam and a proton beam could be accelerated to energies of 27.5 GeV and 920 GeV, respectively, and stored. HERA was capable of storing electrons or positrons. Positrons were used from 1992 until October 1997 and from June 1999 until the second switch–over to electrons in November 2004. The configuration of the HERA facility is sketched in Figure 3.1. Both beams were brought into collision in the north and the south experimental halls where the two collider experiments H1 and ZEUS were located. The HERA–B experiment in the west hall used only the proton beam until the year 2003, whereas in the east hall the HERMES experiment used the positron beam. Both of these experiments used internal targets in one of the HERA beams.

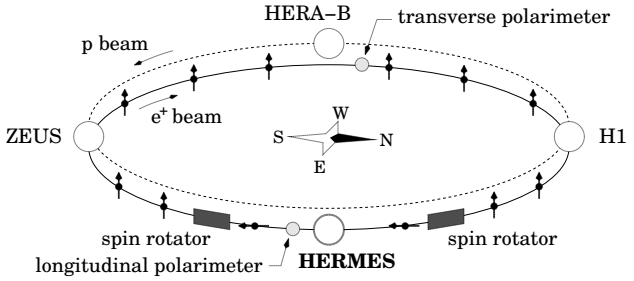


**Figure 3.1:** Schematic view of the HERA storage rings. The spin orientation of the lepton beam is indicated by arrows.

Due to a small asymmetry in the probability of emission of synchrotron radiation, the initially unpolarised leptons become (self-) polarised. This mechanism is called the Sokolov–Ternov effect [ST64]. This effect can theoretically cause polarisations as high as 92.4 %. But due to non-ideal accelarator effects (like e.g. beam-beam-interactions at H1 and ZEUS) during regular operation the routinely obtained polarisation values were at a somewhat lower value around 30—40 %. The typical time constant of the polarisation rise is about 30 min. The spin orientation of the lepton beam is aligned transversely to the beam direction (cf. Figure 3.1) because of the vertical magnetic field of the HERA dipole bending magnets. The polarisation of the beam is continuously measured by two polarimeters, the longitudinal polarimeter LPOL [B$^+$02] and the transverse polarimeter TPOL [B$^+$93], close to the HERA east and west halls. The decrease of the beam currents caused by the scattering of the beam particles requires a refill of

the HERA lepton beam every 8—12 h. The longer life time of the HERA proton beam allows usually more than one lepton fill during a proton fill. Typical beam currents range from 30–40 mA.

## 3.2 The HERMES Target

As the analysis described in the subsequent chapters is performed only on polarised hydrogen data, the following description of the polarised HERMES target [A$^+$05b] will focus on the hydrogen target. A fixed target in a storage ring needs a special setup to preserve a reasonable life time of the stored beam. This is provided by a 40 cm long and 75 $\mu$m thick storage cell. The tube has an elliptical cross section with major and minor axis of 21 mm and 8.9 mm. In order to fulfil the requirements of HERA, an internal gas target was chosen for the HERMES experiment, although solid targets would have provided higher densities. However, a huge advantage of a polarised gas target is that dilutions from unpolarised material, typical for liquid or solid state targets, are not present in the pure gas target. In addition, background from scattering events at the target material container is not present. The target density is approximately $10^{14}$ nucleons/cm$^2$ (integrated over the length of the target cell).
As can be seen in Figure 3.2 the HERMES target consists of the following key components: the atomic beam source (ABS), the storage cell, the target gas analyser (TGA), and the Breit–Rabi Polarimeter (BRP). Furthermore, the target magnet provides a holding field ($B \approx 200$ mT) to define the polarisation axis and to prevent spin relaxation by effectively decoupling the magnetic moments of electrons and nucleons.
The ABS provides the target cell with polarised hydrogen atoms in certain hyperfine states. These states are generated by Stern-Gerlach separation. The atoms with polarised nucleons and unpolarised shell electrons are injected by a powerul system of pumps in the storage cell with fluxes of up to $6.5 \cdot 10^{16}$ atoms/s. For the transversely polarised target at first a spin flip interval of 60 s was used which was later increased to 90 s in order to reduce the dead time during the roughly 1 s long configuration changes. Thanks to this flip systematic uncertainties – those that affect both configurations equally, like e.g. changes in the target density – are averaged out and cancel though.

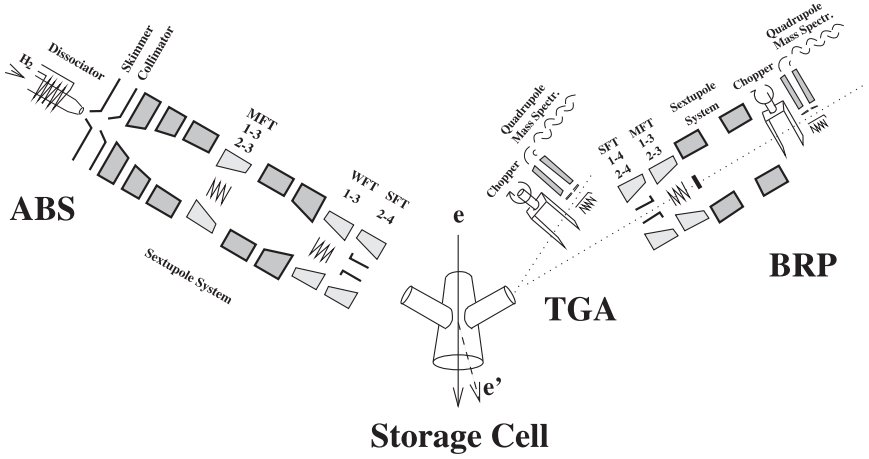


**Figure 3.2:** Schematic view of the polarised target used in the HERMES experiment (without target magnet).

The TGA allows the regular measurement of the atomic and molecular content of the gas sampled the centre of the storage cell. Two values are neccessary for the determination of the density-averaged nuclear polarisation $P_T$. These are the degree of dissociation, also called atomic fraction, in the absence of recombination within the cell, $\alpha_0$, and the fraction of atoms surviving recombination in the cell, $\alpha_R$. They are given by

$$\alpha = \frac{N_H}{N_H + N_{H_2}} \tag{3.2.1}$$

where $N_H$ and $N_{H_2}$ are the normalised nucleon flow rates for atoms and molecules. The PRB provides the value of the realtive population of the the hyperfine states of hydrogen atoms, $P_a$. This value can be related to the polarisation value at the centre of the storage cell, $P_{\mathrm{PRB}}$, by applying a sampling correction $c_P$:

$$P_{\mathrm{PRB}} = c_P \cdot P_a. \tag{3.2.2}$$

Using the BRP and TGA measurements the averaged target polarisation $P_T$ as seen by the electron beam can be calculated:

$$P_T = \alpha_0[\alpha_r + (1-\alpha_r)\beta]P_{\mathrm{BRP}}. \tag{3.2.3}$$

Here, $\beta$ is the ratio of the nuclear polarisation of molecules produced by recombination and the nuclear polarisation of the atoms. Typical target polarisation are $\sim 80\,\%$.

## 3.3 The Spectrometer

The HERMES experiment uses a forward spectrometer for the detection of the scattered lepton and a large fraction of the hadronic final state. It consists of two symmetric halves above and below the horizontal plane in which the HERA beam pipes are located parallel to each other. The top bottom symmetry aids in controlling systematic uncertainties.
In Figure 3.3 a spectrometer cross section in the y–z plane of the HERMES coordinate system is drawn. The z–axis of the right–handed HERMES coordinate system is defined along the lepton beam direction and its x–axis is pointing away from the centre of the HERA rings. The spectrometer magnet provides a vertical field with a deflecting power of $\int B\,dl = 1.3\,\mathrm{T}\cdot\mathrm{m}$. The influence of the field on the HERA beams is minimised by a 11 cm thick steel plate surrounding the beam pipes. The remaining effects are compensated by a correction coil. Field clamps in front of and behind the magnet reduce fringe fields in the adjacent detectors.
The horizontal acceptance of the spectrometer is $\theta_x = \pm 170\,\mathrm{mrad}$. The vertical acceptance $\theta_y = \pm(40\text{–}140)\,\mathrm{mrad}$ has a gap due to the beam pipes embedded in the steel plate.

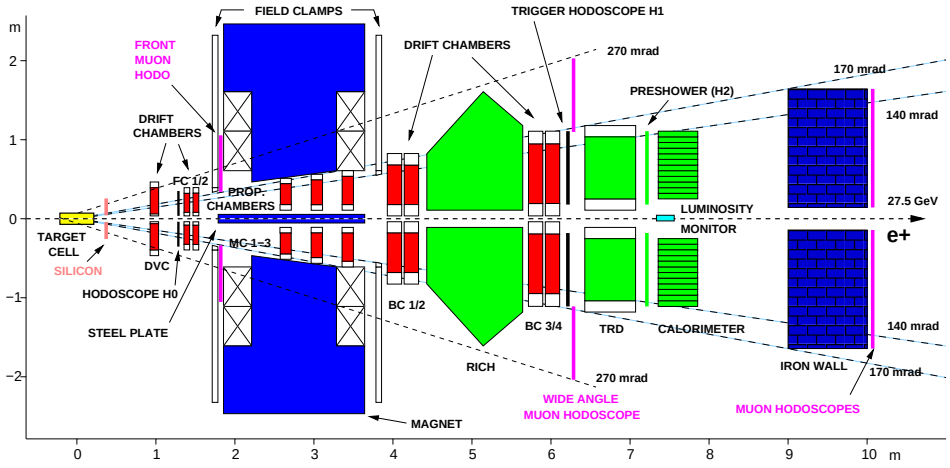


**Figure 3.3:** Side view of the HERMES spectrometer in the configuration operated from 2002 until 2005. The target subsystem containig the target magnet, the atomic beam source, the gas target analyser and the Breit-Rabi polarimeter is not depicted.

A trigger system is used for the very fast discrimination of interesting candidate events from background events and initiates the readout of all spectrometer components. Various first–level triggers are used in the HERMES experiment for DIS events, photo–production events and for calibration and monitoring of the detectors. Throughout this work we use trigger 21 requiring hits in the three hodoscopes H0, H1, and H2 together with an energy deposition in the calorimeter above a threshold energy $E_{\mathrm{thresh}}$, all in coincidence with the HERA beam bunch signal. The threshold energy of the calorimeter is set to 1.4 GeV for data taking with the polarised target.

### 3.3.1 The Tracking System

In front of the spectrometer magnet two drift chambers (FC 1/2) [B$^+$01] are in operation for the reconstruction of the event vertex and the scattering angles with respect to the lepton beam. Each detector consists of $2\times 3$ planes, two planes with wires arranged in the vertical direction, and four wire planes tilted by $\pm 30^\circ$ with respect to the vertical direction. The drift vertex chamber (DVC) enhances the front–track reconstruction. For the track reconstruction behind the magnet two pairs of drift chambers (BC 1/2 and BC 3/4) [B$^+$98] are located in front of and behind the RICH detector. For low–momentum particles which do not reach the rear of the spectrometer three multi–wire proportional chambers (MC 1–3) [A$^+$01] are installed in the gap inside the magnet.

The front and back tracks are reconstructed from the drift chamber hits by a pattern recognition algorithm based on a fast tree search. They are combined if both tracks intersect in the centre of the magnet within a given tolerance. Using look–up tables the momentum of a charged particle is determined from the front and back track parameters. The resolution is given by $\Delta p/p < 2.6\,\%$ and $\Delta\theta < 1.8\,\text{mrad}$. In case of the transverse target holding field the vertex and scattering angle reconstruction has to be corrected for the deflection. To do this the transverse magnet field has to be mapped which was done during the shutdown of 2003. Two different methods for the target magnet correction (TMC) are available, both using the track position information from the DVC and the FCs [AMS+07].

**Correction Method 1** This correction on the particle track is applied based on reference tracks from a database. In a detailed (and time–consuming) tracking calculation a grid of trajectories covering the HERMES acceptance is computed in small steps of momentum, z–vertex and vertical and horizontal angles. From this set the trajectory closest to a measured particle track is selected, based on the tracking information from the DVC and FCs.

**Correction Method 2** This method is based on a ray tracing procedure. Using the reasonable assumption that a trajectory which is in the beginning close to a reference trajectory will also be close to the reference trajectory at the end, a Taylor expansion for the final position in terms of the initial position can be performed. The coefficients provide a quick way to relate the initial position of a track to its final position with the help of a transfer function. For the determination of these transfer coefficients several reference particles had to tracked through the magnet field using the MIT-RAYTRACE program [KE87]. In order to correct the z–vertex position and the scattering angles the right transfer function, which depends on the particle momentum and the z–position from which the particle is assumed to originate, has to be found iteratively until convergence is achieved.

A new tracking code, HTC, is designed to take care of any (known) magnetic field. A test production for the whole 2007 data is available. First results indicate that the resolution and systematic biases are (partially much) better than for tracks reconstructed purely with HRC which is discribed in section 3.4). However, in our analysis we use method 1 for the 03c1 production and method 2 for the 02c1, 04c1 and 05c2 productions.

### 3.3.2 The Particle Identification Detectors

The details relevant for our analysis on aziumuthal SSAs will be addressed in the next chapter. In this subsection we focus on the technical description of the four subsystems of the HERMES spectrometer which give different responses on leptons and hadrons and thus allow a discrimination between the various particle types (order follows the arangement in the spectrometer): a ring–imaging Čerenkov (RICH) detector, a transition radiation detector (TRD), a preshower detector, and an electromagnetic calorimeter.

**The RICH-Detector** This detector operates on the principle that when a charged particle exceeds the speed of light in a medium, it produces a light cone, called Čerenkov light. The opening angle is given by

$$\cos\theta_C = \frac{1}{\beta n}, \tag{3.3.1}$$

where $n$ is the refractive index of the material and the usual $\beta = \frac{v}{c}$. Particles with

$$\beta < \beta_{\text{thresh}} = \frac{1}{n}, \quad \text{which is equivalent to} \quad P < P_{\text{thresh}} = \frac{m}{\sqrt{n^2-1}}, \tag{3.3.2}$$

are below threshhold an cannot emit Čerenkov light. The RICH detector measures the pattern of the Čerenkov photons which permits the reconstruction of the Čerenkov angle $\theta_C$ and thus enables the identification of pions, kaons, and protons in the hadron sample (cf. Figure 3.4). The discrimination between different types of hadrons is accomplished by two carefully selected radiator materials, aerogel (the solid with the lowest refractive index, $n = 1.03$) and $C_4F_{10}$ (the gas with the highest refractive index, $n = 1.0014$). The RICH is also used for the separation of leptons and hadrons.

**The TRD** This Detector serves to distinguish between lepton and hadrons. When a highly relativistic charged particle crosses a dielectric boundary it it has a ceratin likelihood of radiating a photon. Thus the intensity of the emitted radiation is proportional to the particle's Lorentz factor, $\gamma = \frac{E}{m}$. Since the probability for the emission of transition radiation is small for a single boundary many material boundaries are necessary for

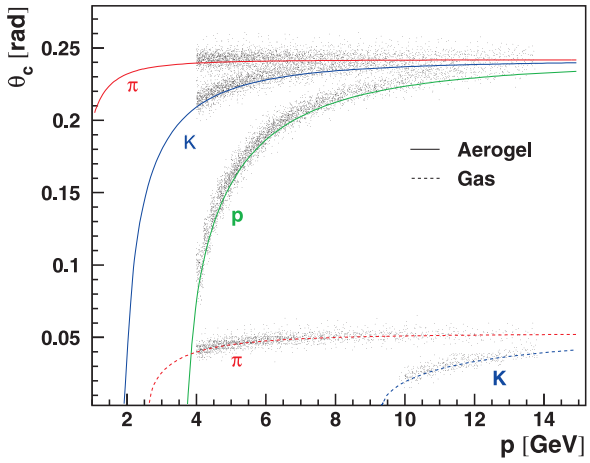


**Figure 3.4:** The angular dependence of RICH photons as a function of hadron momentum. Theoretical curves are overlaid for each hadron type and radiator material. A full pion, kaon, and proton discrimination can thus be made.

the realisation of a TRD. At HERMES polyethylene fibers serve as the radiator material arranged in a plane to form six modules. In the kinematic regime of HERMES only leptons leave significant signals in the TRD, hadrons produce very little signal. Thus the TRD allows a clear discrimination of leptons and hadrons due to their differing energy losses in the TRD.

**The Preshower Detector (H2)** The preshower detector is a scintillating hodoscope with a 11 mm thick curtain of lead in front. The hodoscope (H2) is build from 42 vertical panels of scintillator with a thickness of 1 cm. The panels have an area of $9.3 \times 91\,\mathrm{cm}^2$ and overlap by 2—3 mm for maximum efficiency. The individual panels are read out by photo multipliers (PMTs). For traversing leptons, the passive lead radiator initiates electromagnetic showers which deposit more energy than minimum ionising particles. This results in energy losses of 20–40 MeV for leptons which are $\sim 20$ times larger than those for hadrons.

**The Electromagnetic Calorimeter** In this detector traversing particles lose a (particle-) specific fraction of their energy in an electromagnetic shower. Leptons lose almost all of their energy ($E_{\mathrm{Calo}}/p \approx 1$, where $p = |\vec{p}|$), hadrons lose only a small fraction of their energy ($E_{\mathrm{Calo}}/p < 0.8$, where $p = |\vec{p}|$), due to nuclear interactions and ionisation losses $dE/dx$ (cf. Bethe-Bloch formula [A$^+$08]). The depth of 18 radiation lengths ensures that the shower is almost completely contained in the calorimeter. Each half of the detector is a wall of 420 lead–glass blocks with a cross section of $9 \times 9\,\mathrm{cm}^2$ each.

### 3.3.3 The Luminosity Monitor

Many measurements at HERMES are made by comparing two quantities. In our case, this will be two yields in different target spin configurations. In order to properly normalise these samples, a measure of the relative luminosities of the two samples is necessary. This is accomplished with a pair of small calorimeters each with 12 blocks, placed along the beam pipe. The purpose of this is to measure the rate of either Bhabha scattering (elastic $e^+e^- \rightarrow e^+e^-$) or Møller scattering (elastic $e^-e^- \rightarrow e^-e^-$) from atomic electrons, depending on the beam charge. As the cross sections of these processes are very well known, the luminosity can be determined. The luminosity rate obtained from the monitor is beeing used to calculate the integrated luminosity for each of our samples.

## 3.4 Data Acquisition (DAQ) and Processing

The readout of the detector is carried out by specific readout electronics hosted in Fast-Bus crates which are located in an electronic trailer close to the spectrometer. For the timing and analogue information FastBus TDCs ("Time-to-Digital Converter") and FastBus ADCs ("Analogue-to-Digital Converter") are in use. The data from the FastBus crates are bundled by event builder modules and sent over fast optical links to a Linux cluster, where they are stored on staging disks and on data tapes. So called slow control data, like information from the luminosity monitor, the polarimeters, the target, detector temperatures, voltage settings, etc., is recorded in addition. The slow control data are read out once every 10 s, independent of triggers from the spectrometer. All raw data is buffered in EPIO format

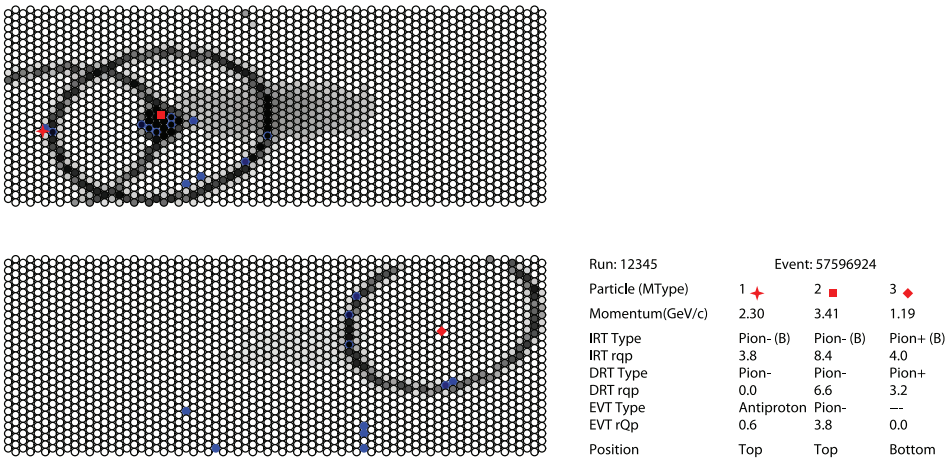


**Figure 3.5:** The RICH EVT algorithm's interpretation of a three track event. Track locations are indicated in red. The EVT algorithm generates hypothetical hit patters (gray) based on the possible hadron identities (dark grey bands) and a simulated background pattern (light gray haze). Hits in the RICH are indicated in blue. The hypothetical patterns are compared with the hit locations to select the most likely hadron identity.

on hard disks in the Linux cluster and backed up regularly on data tapes. It is transferred to a taping robot at the DESY main site after the end of each HERA lepton fill using a FDDI ("Fast Distributed Data Interface") link.

From the electronic detector signals, the hit positions, energy depositions, etc. are determined with the HERMES decoder (HDC) using mapping, geometry and calibration of the individual detectors. All required information is stored in an ADAMO [] database, which is an entity relationship database allowing structured and portable data storage. In a next step the HERMES reconstruction (HRC) program finds tracks in the spectrometer. Using a timing signal that is written to the event data and slow control data streams, both data streams can be synchronised.

It is worth mentioning that HRC knows almost nothing about the RICH and, thus, about the discrimination of the different hadron types. As a consequence it is neccessary to perform additional processing such as running particle identifucation algorithms. Examples of this are Indirect Ray Tracing (IRT) and Direct Ray Tracing (DRT). More details on the RICH PID reconstruction can be found in [Hom03]. The latest development for the RICH is an event level algorithm (EVT) [LH08]. The idea here is to consider all of the tracks in the detector at once. This is done by taking the existing expected patterns from the DRT algorithm and adding them together. The idea is to improve the identification of tracks that are close together and whose Cerenkov rings overlap. This is especially important for analyzers that are specifically looking at multiple track events or events where two tracks are close together. The complication is that there are three mass hypotheses for each track, so the number of combined hypotheses scales like $3^{\#\text{tracks}}$. So, if there are 4 tracks in the detector that's 81 hypotheses to check. Fortunately the number of tracks at HERMES is rarely more than 3. After all these hypotheses are evaluated. The most likely one gives the particle type for all the tracks in the event. An output for an event of the RICH EVT algorithm can be seen in Figure 3.5. At the end of the data processing chain, all synchronised data which is useful for physics analyses, is stored in data summary tables the so called $\mu$DST files ($\mu$DST for "*small* Data Summary Tape").

Different time scales are used in the HERMES data (cf. Table 3.1). The shortest time interval is the event containing all reconstructed tracks which are observed when a trigger is generated. All events recorded within approximately 10 s are grouped into a burst. This is the time scale on which the slow control information is synchronised to the event data. In order to split up the raw data into small enough pieces for storage, bursts are combined into a run with a size of about 450 MB. Dependent on the luminosity, a run lasts around 10 min. The longest time scale, the fill, is determined by the 8–12 h storage time of the HERA lepton beam. Optimum event rates for the DAQ are $\sim$ 300 Hz.

| Name of Scale | Length of Scale | Description |
|---|---|---|
| Fill | 8–12 h | Storage time of HERA lepton beam |
| Run | $>$ 5 min | Time required to collect 450 MB of data, highly correlated with beam current |
| Burst | $\sim$ 10 s | One unit of slow control time |
| Event | none | One single HRC production |

**Table 3.1:** An overview over the different time scales at HERMES.

# Chapter 4

# The Extraction of the Analysing Power $A_{UT}$

The analysing power, discussed in Chapter 3, has been extracted in the analysis of the HERMES data collected during the 2002–2005 running period, in which a transversely polarised hydrogen target was used. To this purpose several checks were applied in order to ensure a high quality of the data before selecting inclusive charged hadrons. The hadron yields were used to construct a single-spin asymmetry (SSA) dependent on the azimuthal angles $\phi$, as reported in Section 2.3 of Chapter 3. The analysing power $A_{UT}$ was then extracted in a binned least square fit. In addition, several tests on the extraction method were performed to estimate the qualitative impact of different sources of systematic errors on the final results.

## 4.1 The Extraction Method

In our approach, each of the kinematic variables $P_{h\perp}$ and $\frac{p_z}{E_{Beam}}$ is binned, together with the azimuthal angle $\phi$ (cf. e.g. Figure 4.1), according to the scheme shown in Table 4.1. In contrast to an usual (SI)DIS analysis at HERMES we can choose a much finer binning since our data set of inclusive charged hadrons luckily does not lack of sufficient statistics. This circumstance allows to choose identical kinematic binnings for kaons and pions making comparisons and interpretations easier.

| Variable | # of Bins | Bin Borders | | | | |
|---|---|---|---|---|---|---|
| $P_{h\perp}$ | 10 | $[0.0,0.2]$ | $]0.2,0.3]$ | $]0.3,0.4]$ | $]0.4,0.5]$ | $]0.5,0.6]$ |
| | | $]0.6,0.7]$ | $]0.7,0.8]$ | $]0.8,1.0]$ | $]1.0,1.2]$ | $]1.2,3.0]$ |
| $\frac{p_z}{E_{Beam}}$ | 10 | $[0.00,0.10]$ | $]0.10,0.13]$ | $]0.13,0.17]$ | $]0.17,0.20]$ | $]0.20,0.23]$ |
| | | $]0.23,0.27]$ | $]0.27,0.30]$ | $]0.30,0.37]$ | $]0.37,0.43]$ | $]0.43,1.00]$ |
| $\phi$ | 18 | $[\frac{\pi}{9},\frac{2\pi}{9}]$ | | $\cdots$ | | $]\frac{17\pi}{9},2\pi]$ |

**Table 4.1:** Binning in the kinematic variables $P_{h\perp}$ and $\frac{p_z}{E_{Beam}}$. For the azimuthal angle $\phi$ an equidistant binning is chosen for all particles.

There are several ways to define the analysing power $A_N$. In former analyis at HERMES [A$^+$00, DNLRS$^+$08] the analysing power $A_N$ was defined in a strict geometric way. Therefore, the detector was divided into two halves – the right and left side in the HERMES coordinate system:

$$A_N(P_{h\perp},\tfrac{p_z}{E_{Beam}}) = \frac{\frac{(N_R^{\uparrow}-N_L^{\uparrow})}{L_P^{\uparrow}} - \frac{(N_R^{\downarrow}-N_L^{\downarrow})}{L_P^{\downarrow}}}{\frac{(N_R^{\uparrow}+N_L^{\uparrow})}{L^{\uparrow}} + \frac{(N_R^{\downarrow}+N_L^{\downarrow})}{L^{\downarrow}}}. \tag{4.1.1}$$

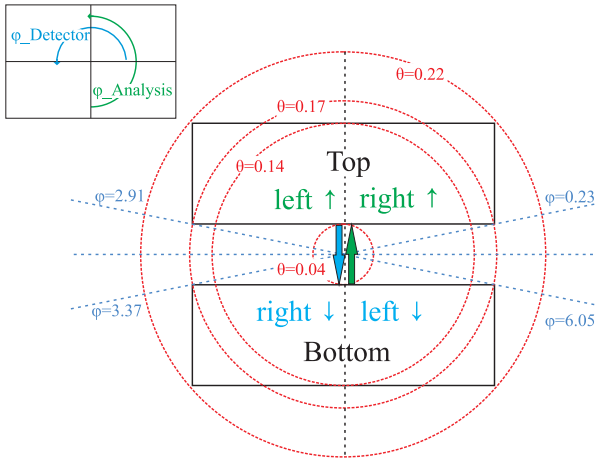


**Figure 4.1:** Front-scheme of HERMES spectrometer: HERMES angular acceptance is delimited in the azimuthal angle $\phi$ by the red dotted circles, and in the polar angle $\theta$ by the blue dotted lines. Note that the angle $\phi$ in our analyis corresponds to $\phi_{Detector} + \frac{1}{2}$, see sketch in the top-left corner.

The subscripts $R$ and $L$ refer to the left and the right side of the spectrometer, the superscripts $\uparrow$ and $\downarrow$ refer to the two target spin states. Of course, this definition dependends on the target spin state, meaning that $A_N$ changes sign when the target spin flips. Recent studies have shown that this definition dramatically depends on acceptance effects of the HERMES spectrometer [DNLRS$^+$08] (cf. Figure 4.1). As a consequence, the analysing power defined in Equation (4.1.1) underestimates the "true" asymmetry. For that reason, in this analyis we decided to adapt an innovative approach, based on the analyis of azimuthal Fourier amplitudes.
Our extraction method of choice follows the technique presented in [A$^+$09]. The yields of a given particle type, namely charged pions and kaons, in a given $P_{h\perp}$, $\frac{p_z}{E_{Beam}}$ and $\phi$ bin and for a given target spin direction ($\uparrow$ upwards or $\downarrow$ donwards) can be expressed as

$$N^{\uparrow(\downarrow)}(P_{h\perp}, \tfrac{p_z}{E_{Beam}}, \phi) = \sigma_0(P_{h\perp}, \tfrac{p_z}{E_{Beam}}) \cdot \left[ L^{\uparrow(\downarrow)} + (-) L_P^{\uparrow(\downarrow)} \cdot A_{UT}^{\sin\phi}(P_{h\perp}, \tfrac{p_z}{E_{Beam}}) \cdot \sin\phi \right] \cdot \Omega(P_{h\perp}, \tfrac{p_z}{E_{Beam}}, \phi), \quad (4.1.2)$$

where $\phi$ is the azimuthal angle about the beam direction between the hadron scattering plane and the $\uparrow$ direction of the target spin, $\sigma_0$ is the unpolarised cross section and $A_{UT}^{\sin\phi} \cong \Delta\sigma(P_{h\perp}, \frac{p_z}{E_{Beam}}) / \sigma_0(P_{h\perp}, \frac{p_z}{E_{Beam}})$, with $\Delta\sigma(P_{h\perp}, \frac{p_z}{E_{Beam}})$ being the $\phi$-independent part of the the asymmetry, defined in (2.2.38). Also, $L^{\uparrow(\downarrow)}$ are the total luminosities in the $\uparrow$ and $\downarrow$ polarisation states, $L_P^{\uparrow(\downarrow)}$ are the luminosities weighted by the magnitude $P$ of the target polarisation, and $\Omega$ is the detector acceptance efficiency in the $(P_{h\perp}, \frac{p_z}{E_{Beam}}, \phi)$ bin. The $\sin\phi$ modulation follows directly from the spin dependent part of the cross section (2.2.35). Equation (2.2.35) applies only to the DIS regime. Our analysis, though, covers the full kinematic range from DIS to photoproduction). The asymmetry was calculated for each $(P_{h\perp}, \frac{p_z}{E_{Beam}}, \phi)$ bin as follow

$$A_{UT}(P_{h\perp}, \tfrac{p_z}{E_{Beam}}, \phi) = \frac{\frac{N^\uparrow}{L_P^\uparrow} - \frac{N^\downarrow}{L_P^\downarrow}}{\frac{N^\uparrow}{L^\uparrow} + \frac{N^\downarrow}{L^\downarrow}}, \quad (4.1.3)$$

where the subscript "$UT$" denotes an unpolarised beam and a transversely polarised target. The advantage of using this fully-differential asymmetry $A_{UT}(P_{h\perp}, \frac{p_z}{E_{Beam}}, \phi)$ in Equation (4.1.3) instead of the more common left-right asymmetry $A_N(P_{h\perp}, \frac{p_z}{E_{Beam}})$ (cf. Equation (4.1.1)) is that the acceptance function $\Omega$ cancels in each $(P_{h\perp}, \frac{p_z}{E_{Beam}}, \phi)$ kinematic bin. This new definition is, thus, more suitable for a detector with limited acceptance, like the HERMES one. It accounts for the contributions of particles which vanish in the acceptance gap (cf. Figure 4.1). Combining (4.1.2) and (4.1.3), the asymmetry can be approximated, for small differences of the two average target polarizations $\langle P^\uparrow \rangle$ and $\langle P^\downarrow \rangle$ as

$$A_{UT}(P_{h\perp}, \tfrac{p_z}{E_{Beam}}, \phi) = A_{UT}^{\sin\phi} \sin\phi + \tfrac{1}{2} \cdot \frac{\langle P^\uparrow \rangle - \langle P^\downarrow \rangle}{\langle P^\uparrow \rangle \cdot \langle P^\downarrow \rangle}. \quad (4.1.4)$$

As shown in Table 4.2, $\langle P^\uparrow \rangle$ and $\langle P^\downarrow \rangle$ are the same for all data taking periods (within the given precision).

| Year | $\langle P^{\uparrow} \rangle$ | $\langle P^{\downarrow} \rangle$ |
|---|---|---|
| 2002 | 0.795 | 0.795 |
| 2003 | 0.795 | 0.795 |
| 2004 | 0.777 | 0.777 |
| 2005 | 0.745 | 0.745 |

**Table 4.2:** Average target polarisations for the four data sets used in this analysis.

For a detector with full $2\pi$-coverage, the $\sin\phi$ amplitude $A_{UT}^{\sin\phi}$ and the left-right asymmetry $A_N$ are related by

$$A_N = \frac{\int_0^{\pi} d\phi\, \Delta\sigma \sin\phi}{\int_0^{\pi} d\phi\, \sigma_0} = \frac{2}{\pi} \cdot A_{UT}^{\sin\phi}. \tag{4.1.5}$$

The $A_{UT}^{\sin\phi}$ amplitudes were extracted with a binned $\chi^2$ fit of the measured asymmetry to a functional form $p1 \cdot \sin\phi + p2$. Our fit routine makes use of the MIGRAD routine of the MINUIT program [JR75]. As already noted, the average polarisations equal only to a certain level of precision. Leaving $p2$ as a free parameter or fixing it to the values given by Equation (4.1.5) and Table 4.2 has no impact on the extracted $\sin\phi$ amplitude $p1 = A_{UT}^{\sin\phi}$.

## 4.2 The HERMES Data Productions

The starting point of all the analyses performed at HERMES is represented by the so-called $\mu$DST files, in which the data, after being processed as described in Section 3.4, is stored. The $\mu$DST files are labeled by the last two digits of the corresponding year of data taking, a letter to indicate the production, and a cipher. In the first production of $\mu$DST files for a new data taking period (a-production), detector calibrations based on the data of the preceding period are used. The a-production allows detailed detector calibrations which serve as input for a re-production of the $\mu$DST files (b-production). In the subsequent c-production, additional corrections which rely on proper calibrations are taken into account. The cipher, which completes the production name, is increased for further fast re-productions which do not require the track reconstruction. Such re-productions are usually carried out when improved slow control information such as beam or target polarisation values becomes available.
The analysis presented here is based on the HERMES full transverse data set, recorded during the 2002–2005 data taking period, in which a transversely polarised hydrogen target was used. The data productions used in the present analysis are: 02c1, 03c1, 04c1 and 05c2.

## 4.3 Burst Level Data Selection

### 4.3.1 Data Quality

Since, depending on the purpose of the analysis, not all the information from the entire experimental set-up is needed, the $\mu$DST files also contain events collected when one or more detectors were not working properly. The first step of each analysis consists in the selection of those events for which all needed parts of the experimental set-up were properly operating. All information about the performance of the detectors, which is stored at the burst level, is combined, by the data-quality group [HER], into the so-called burst lists. These lists contain bit patterns of 32 bits for each burst for both detector halves. Each bit corresponds to a certain detector (or part of the experiment) and is set to "1" if the detector was operating properly and to "0" in the opposite case. For the present analysis all bits were required to be set to "1", with the only exception of the bit #1 and #28, which require a beam polarisation above 30 %. This requirement is left out since the present analysis deals with single spin asymmetries in which only the target (and not the beam) needs to be polarised.

| Data Quality Flag | Burst Selection Criterion |
|---|---|
| 00 | Target spin parallel or antiparallel to beam. |
| 01 | Beam polarisation $> 30\,\%$. |
| 02 | Reasonable DAQ deadtimes. |
| 03 | Reasonable burst lengths. |
| 04 | Beam current reasonably large. |
| 05 | Varies by year. Count rates or target density °uctuations reasonable. |
| 06 | First burst of each run rejected. |
| 07 | Last burst of each run and bursts with unde¯ned DAQ state rejected. |
| 08 | Varies by year. Nominal DAQ or PID detector states. |
| 09 | Runs marked analysable by shift crew. |
| 10 | Polarised target mode. |
| 15 | Polarised target mode (determined from valve state of target). |
| 16 | Target state good. |
| 17 | All calorimeter blocks good. |
| 18 | Hodoscope H2 or Luminosity monitor are good. |
| 19 | TRD data quality good. |
| 20 | No high-voltage trips in wire chambers. |
| 21 | Various problems by year (target, tracking, calorimeter, or RICH). |
| 22 | No trips in RICH. |
| 23 | $\alpha_0$ value is reasonable. |
| 24 | $\alpha_R$ value is reasonable. |
| 25 | RICH data quality good. |
| 26 | Various. Either bad VC synchronisation or target in tensor state. |
| 27 | Valid target polarisation measurement by BRP. |
| 28 | Beam polarisation measurement not older than five minutes. |
| 29 | Target magnet current in reasonable range. |
| 30 | Deadtime in reasonable range. |
| 31 | Varies by year. Middle calorimeter blocks good. |

**Table 4.3:** Format of the burst lists. In our analysis bit #01 & #28 are not set; bits #11, #12, #13 and #14 are equivalent to bit #10 and are redundant.

### 4.3.2 Calculation of the Luminosity

For the caluclation of asymmetries the knowledge of relative luminosities is essential. In addition, unlike when measuring a cross section, a perfectly calibrated, absolute measurement of the luminosity is unnecessary. However, for measuring asymmetries, knowing the relative luminosity of the data collected in the two target spin configurations is essential for properly balancing yields. The calulcation of the luminsity is carried out using the response of the luminosity monitor (cf. Subsection 3.3.3). In our analysis the following formula is used to calculate the luminosity for each burst

$$\mathcal{L} \;=\; \langle R_{\text{Lumi}} \rangle \;\times\; C_{\text{Lumi}} \;\times\; A \;\times\; \tau_{\text{DAQ-up}} \;\times\; t_{\text{Burst}}, \tag{4.3.1}$$

where $\langle R_{\text{Lumi}} \rangle$ is the average rate measured by the luminosity monitor, $C_{\text{Lumi}}$ is a proportionality constant which varies year-to-year relating the rate to the luminosity per nucleon, $A$ is the number of nucleons per nucleus, $\tau_{\text{DAQ-up}}$ is the fractional live-time of the DAQ (in %) and $t_{\text{Burst}}$ is the length of the burst.

## 4.4 Track Level Data Selection

Once the 'good' bursts of a certain data production are selected according to the previously mentioned data quality criteria, several requirements have to be imposed at the track level. Indeed, a number of cuts and constraints have to be applied on the recorded tracks in order to correctly identify Inclusive Charged Hadrons. The tracks that pass all requirements constitute the data set that is used in the physical analysis. In this Section the various selection criteria are discussed. The cuts are described in the order as they are applied in the analysis chain.

### 4.4.1 Geometry Cuts

Before the identification of the particles, several geometry cuts on the particle tracks are applied to ensure that the track reconstruction was not influenced by the edges of the HERMES spectrometer and to suppress background. The longitudinal vertex coordinate $z_{\text{vertex}}$ at which the scattering occurred, is restricted to the dimension of the target cell. In addition, the vertical and horizontal positions of the track are checked at the locations of several detector components which limit the HERMES acceptance (e.g. detector frames, magnetic field-clamps and support structures). All geometry cuts are termed fiducial volume cuts and are listed in Table 4.4. These cuts are only applicable for charged particles. The resulting distributions on spatial variables which are relevant for the analysis are depicted in Figure 4.2.

| | Cut |
|---|---|
| vertex position | $\lvert z_{\text{vertex}}\rvert \leq 18\,\text{cm}$ |
| calorimeter position | $\lvert x_{\text{calo}}\rvert \leq 175\,\text{cm}$<br>$30\text{cm} \leq \lvert y_{\text{calo}}\rvert \leq 108\,\text{cm}$ |
| front field clamp position | $\lvert x_{\text{ffc}}\rvert \leq 31\,\text{cm}$ |
| septum plate position | $\lvert x_{\text{sp}}\rvert > 7\,\text{cm}$ |
| rear fieldclamp position | $\lvert x_{\text{rfc}}\rvert < 54\,\text{cm}$ |
| rear clamp position | $\lvert x_{\text{rc}}\rvert \leq 100\,\text{cm}$<br>$\lvert y_{\text{rc}}\rvert \leq 54\,\text{cm}$ |

**Table 4.4:** The geometrical cuts applied to the detected charged particles.

### 4.4.2 Particle Identification

In this analysis of Inclusve Charged Hadrons presented in this thesis we well only consider charged hadrons, especially charged mesons. Thus, in a first step we have to remove all leptons from the data sample of interest. In a second step we will determine the types of the hadrons which remain in our sample. In the following paragraphs we will try to clarify these two steps.

#### Lepton-Hadron Separation

Combining the responses of the four PID ("Particle Identification") detectors (cf. Subsection 3.3.2) a very good separation between leptons (electrons and positrons) and hadrons is achievable at HERMES. From the response of the particle identification detectors it is possible to generate a likelihood function, *PID* (cf. Equation (4.4.3)), that is related to the probability of a particle to be a hadron or a lepton. In particular, given the energy $E$ deposited in the detector and the momentum $p = |\vec{p}|$ of the particle, the issue is to find the conditional probability $P(H_{l(h)}|E,p,\theta)$ for the hypothesis $H_{l(h)}$ that the particle is a lepton $l$ or a hadron $h$. Bayes theorem relates such a probability to the observable probabilities $P(H_{l(h)}|p,\theta)$, the so called prior probability or particle fluxes, that a particle with momentum $p$ and angular angle $\theta$ is a lepton (hadron), and $P(E|H_{l(h)},p)$, the so called parent distribution, that a

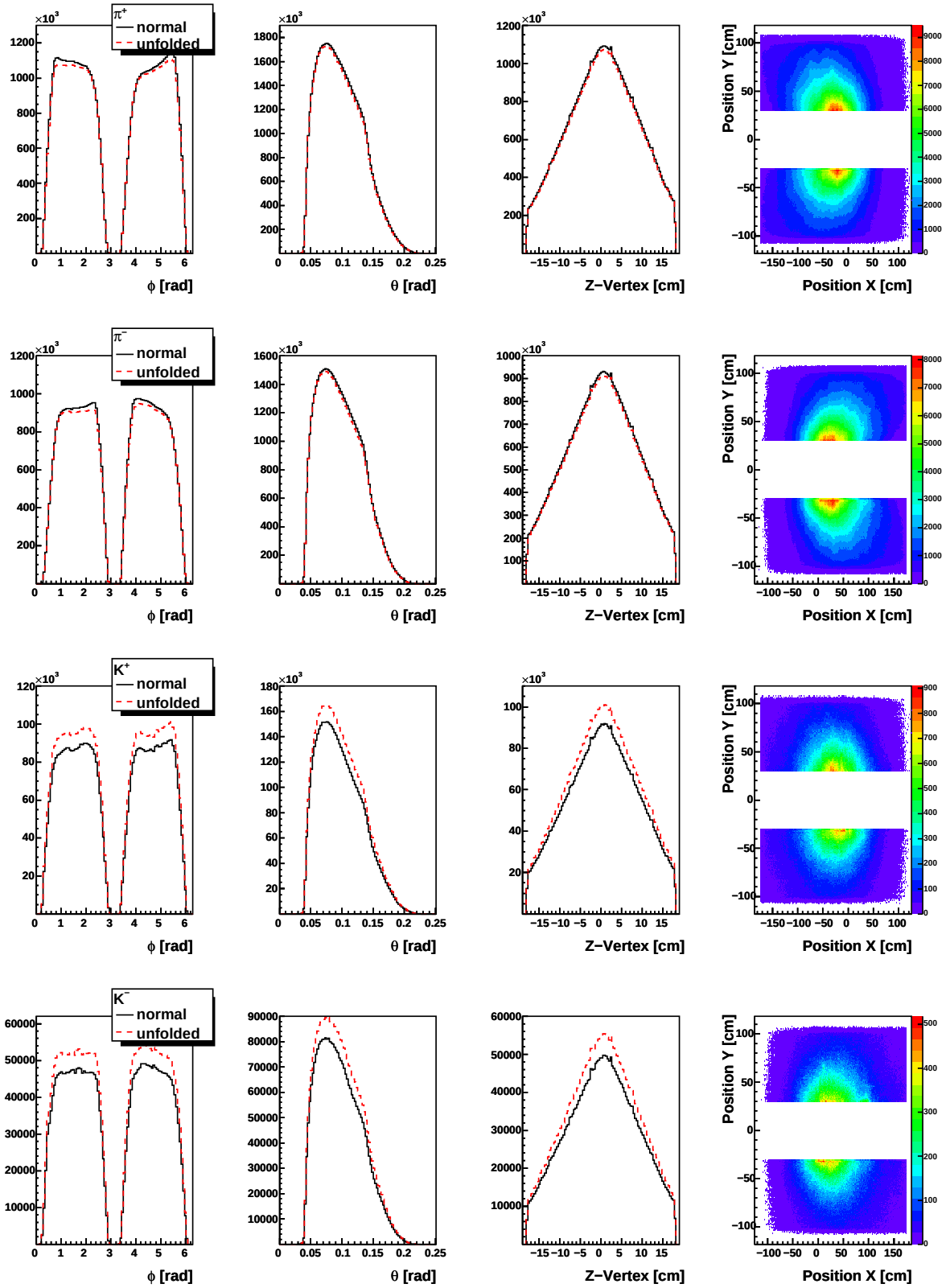


**Figure 4.2:** The distributions of the four hadron types $\pi^+$, $\pi^-$, $K^+$ and $K^-$ (from top to bottom) in the variables $\phi$, $\theta$, $z_{\text{Vertex}}$ and the corresponding hit positions in the calorimeter (from left to right). The black lines correspond to the unweighted distributions, the red lines to the weighted distributions making use of the EVT weights (cf. Subsection 4.4.2, "Charged Hadron Identification"). The gap in the acceptance of the HERMES is clearly visible in the $\phi$-distributions and in the hit positions of the calorimeter. The distributions base on the complete 2002–2005 data set after applying both geometric and kinematic cuts.

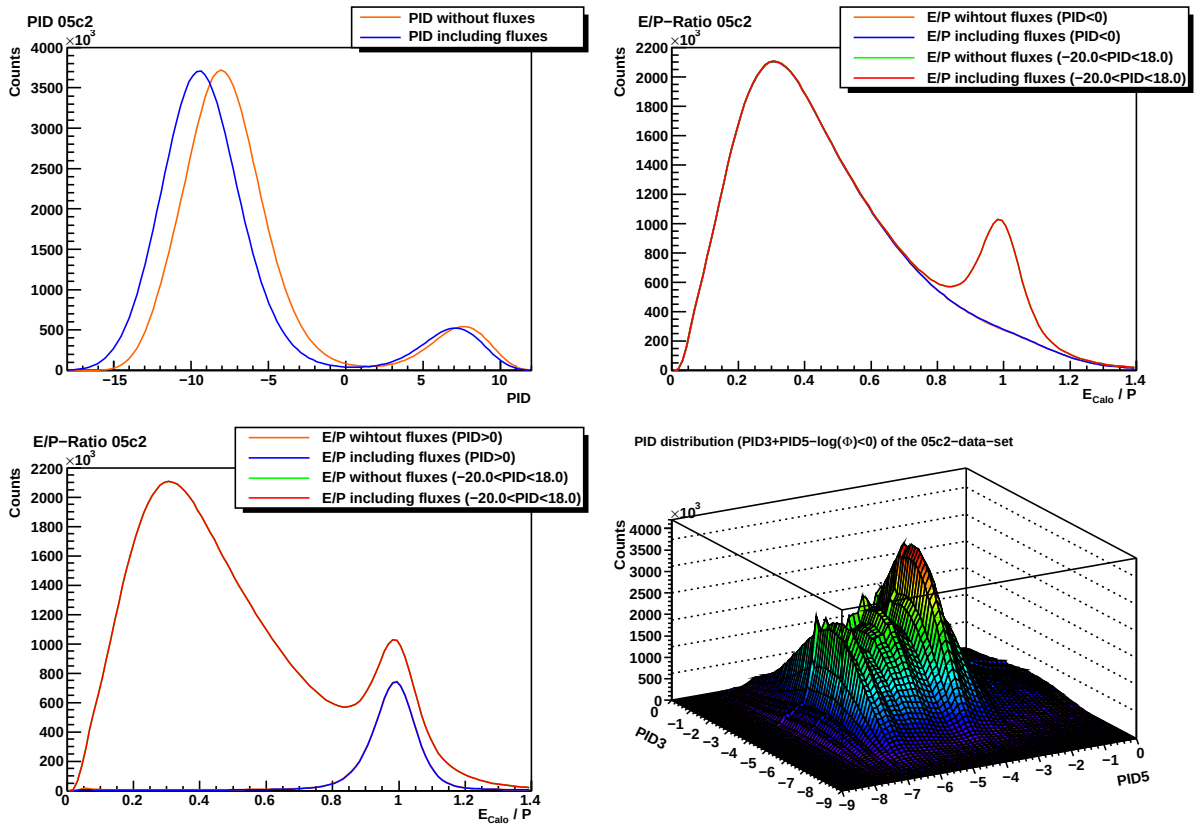


**Figure 4.3:** **Top-left panel**: *PID* distributions of hadrons (left peak) and leptons (right peak), the influence of the fluxes (blue line) is clearly visible compared to a *PID* distribution without including the flux factors $\Phi(p,\theta)$ (red line). **Top-right & bottom-left panel**: $E/p$ distributions of leptons and hadrons. Our cut $PID < 0$ results in a clear lepton-hadron dicrimination and a pure hadron sample. **Bottom-right panel**: two dimensional PID3-PID5-Distributions of the hadron sample within the acceptance of the HERMES spectrometer after passing cut (4.4.8). The histograms rely on the 05c2 production after applying data quality cuts.

lepton (hadron) with a momentum $p$ deposits an energy $E$ in the detector [Wen01]:

$$P(H_{l(h)}|E,p,\theta) = \frac{P(H_{l(h)}|p,\theta)\cdot P(E|H_{l(h)},p)}{P(H_l|p,\theta)\cdot P(E|H_l,p)+P(H_h|p,\theta)\cdot P(E|H_h,p)}. \tag{4.4.1}$$

The fluxes $P(H_{l(h)}|p,\theta)$ and the parent distributions $P(H_h|E,p)$ can be estimated in a test beam facility by measuring the response of the detectors to a beam of leptons or hadrons. A different approach, which is commonly used at HERMES, consists in measuring the response of a given PID detector for a certain type of particle which is selected by the other PID detectors. This method has the advantage of taking into account possible ageing effects of the detectors. The cuts have to be hard enough to define a clean sample but, at the same time, have to ensure reasonable statistics. As a consequence the cut ranges vary for each data production, being tighter for the productions with higher statistics and less tight for those with a lower statistics. Combining the probabilities $P(H_l|E,p)$ and $P(H_h|E,p)$, defined in Equation (4.4.1), to a logarithmic ratio one obtains the *PID* value which, in our analysis, is calculated for each track:

$$PID = \log_{10}\frac{P(H_l|E,p,\theta)}{P(H_h|E,p,\theta)} = \log_{10}\frac{P(H_l|p,\theta)\cdot P(E|H_l,p)}{P(H_h|p,\theta)\cdot P(E|H_h,p)} = PID_{\text{Detector}} - \log_{10}\Phi, \tag{4.4.2}$$

where

$$PID_{\text{Detector}} = \log_{10}\frac{P(E|H_l,p)}{P(E|H_h,p)} \quad \text{and} \quad \Phi \equiv \Phi(p,\theta) = \log_{10}\frac{P(H_h|p,\theta)}{P(H_l|p,\theta)} = \frac{\Phi_h(p,\theta)}{\Phi_l(p,\theta)}. \tag{4.4.3}$$

The particle's momentum $p$ and its polar angle $\theta$ are provided by the tracking system. The hadron (lepton) fluxes $\Phi_h(p,\theta)$ ($\Phi_l(p,\theta)$) are calculated with an iterative procedure. Although the contribution of the fluxes to

the absolute *PID* value is small, they certainly increase the efficiency of the hadron (lepton) identification and decrease the contamination of the data sample by the opposite, unwanted particle species. This is subject of the next paragraph, though. In general the combined $PID_{\text{Detectors}}$ value for more than one detector is given by:

$$PID_{\text{Detectors}} = \log_{10} \prod_{\text{Detectors}} \frac{P_{\text{Detector},i}(E|H_l,p)}{P_{\text{Detector},i}(E|H_h,p)} = \sum_{\text{Detectors}} PID_{\text{Detector,i}}. \tag{4.4.4}$$

Practically, in our analysis we use two distinct *PID* values for the lepton-hadron discrimination:

$$PID3 \equiv PID_{\text{Calo}} + PID_{\text{Pre}} + PID_{\text{RICH}} \tag{4.4.5}$$

$$PID5 \equiv PID_{\text{TRD}}, \tag{4.4.6}$$

where we combine the signals of the PID detectors mentioned in Subsection 3.3.2. Combining Equation (4.4.2) with (4.4.5) and (4.4.6) yields:

$$PID = PID3 + PID5 - \log_{10}\Phi = \log_{10}\frac{\mathcal{P}_l}{\mathcal{P}_h}, \tag{4.4.7}$$

which represents the logarithm of the probability ratio that a given particle is a lepton or a hadron. By definition, the quantity in (4.4.7) is positive if the probability of being a lepton is higher than that of being a hadron, and negative in the opposite case. In this analysis we therefore apply the following cut to the combined *PID* values in order to obtain a pure hadronic data sample:

$$PID3 + PID5 - \log_{10}\Phi < 0. \tag{4.4.8}$$

Figure 4.3 shows that our choice of the *PID* cut results in $E/p$-distributions which are typical for hadrons at HERMES (cf. 3.3.2, "The Electromagnetic Calorimeter"). Furthermore, the contribution of the fluxes $\Phi$ to the *PID* value is shown.

**PID Efficiencies and Contaminations**

A cut on the *PID* value is always connected to efficiency losses and contaminations. The efficiency of hadron identification is defined by the fraction of true hadrons which pass the cut on the *PID* value whereas the contamination is the fractional contribution of leptons to the sample identified by the same cut. A high cut value ensures that the true hadrons are contained in the identified hadron sample with a large fraction, but the contamination by leptons becomes high at the same time. The higher the cut value, the lower the contamination of leptons in the hadron sample at the expense of a lower efficiency for hadrons. By a low cut value a high purity of the hadron sample can be obtained but the measurement of azimuthal asymmetries of Inclusive Charged Hadrons requires not only a clean sample but also correct count rates. In this analysis the cut on the *PID* value is chosen at $PID_h = 0$ (cf. Equation (4.4.8)) to keep lepton contamination low and hadron efficiency high at the same time.
The calculation of efficiencies $\mathcal{E}$ and contaminations $\mathcal{C}$ requires integrations over the lepton distribution $N_l$ and the hadron distribution $N_h$:

$$\mathcal{C}(PID_h) \equiv \frac{\int_{-\infty}^{PID_h} dPID\, N_l}{\int_{-\infty}^{PID_h} dPID\,(N_h + N_l)} \tag{4.4.9}$$

$$\mathcal{E}(PID_h) \equiv \frac{\int_{-\infty}^{PID_h} dPID\, N_h}{\int_{-\infty}^{\infty} dPID\, N_h}, \tag{4.4.10}$$

According to the definition of *PID*, $PID = \log_{10}\frac{P(H_l|E,p,\theta)}{P(H_h|E,p,\theta)}$ (cf. Equation (4.4.2)), the *PID* value is connected to the ratio of probabilities for a particle being a lepton and being a hadron, and, thus, to the fractional contributions of leptons and hadrons. Using this Equation in combination with the unity condition

$$P(H_l|E,p,\theta) + P(H_h|E,p,\theta) = 1, \tag{4.4.11}$$

the distributions $N_l$ and $N_h$ required by Equations (4.4.9) and (4.4.10) can be derived:

$$N_l = P(H_l|E,p,\theta) = \frac{10^{PID}}{1+10^{PID}} \tag{4.4.12}$$

$$N_h = P(H_h|E,p,\theta) = \frac{10}{1+10^{PID}}. \tag{4.4.13}$$

Figure 4.4 shows the distributions of the *PID* value and the contributions of leptons and hadrons according to Equations (4.4.12) and (4.4.13). Figure (4.5) illustrates the resulting lepton contaminations and hadron efficiencies according to Equations (4.4.9) and (4.4.10). Efficiencies above 99.93 % are reached, the contaminations lie far below 0.4 %.

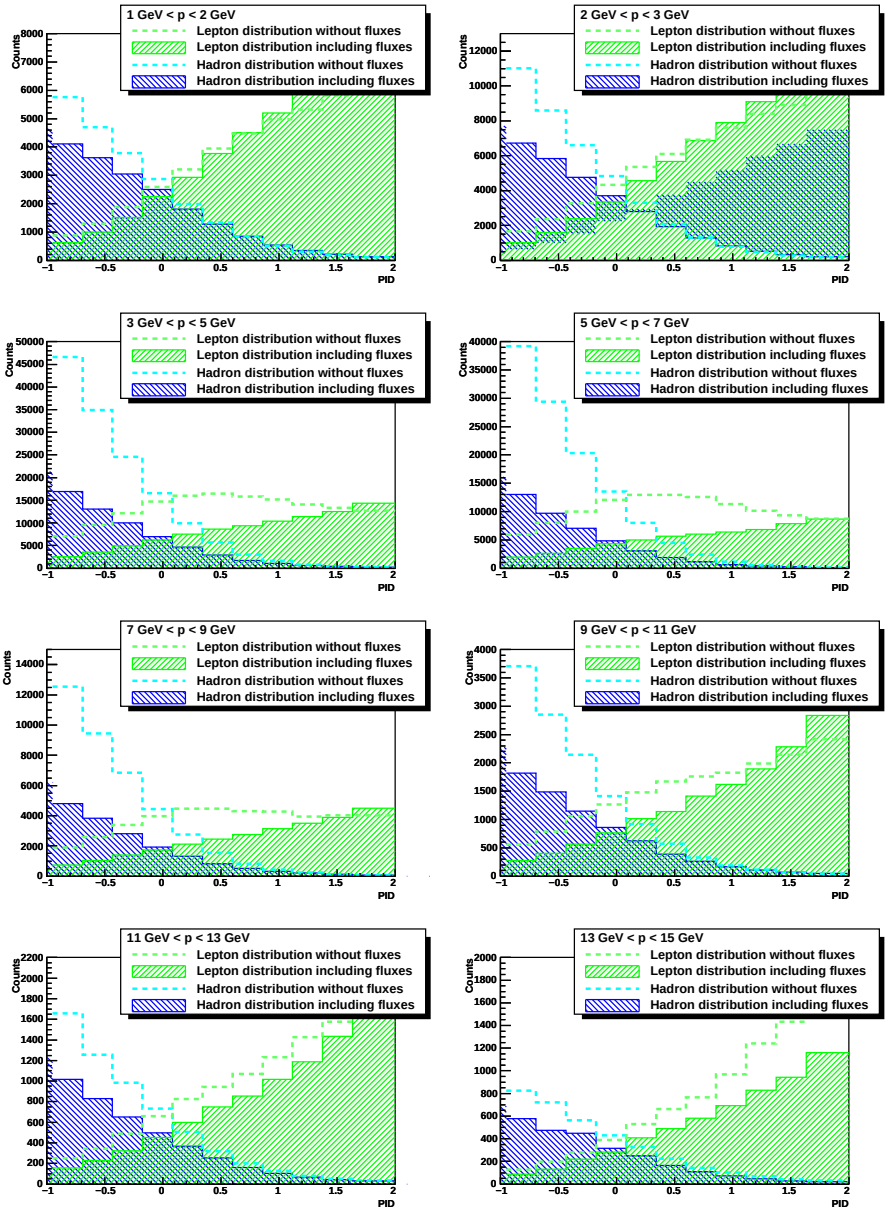


**Figure 4.4:** Distributions of leptons $N_l$ (green) and hadrons $N_h$ (blue) according to Equations (4.4.12) and (4.4.13) in momentum bins $1\,\text{GeV} < p < 16\,\text{GeV}$. The dashed curves illustrate the influence of the fluxes on the distributions. By including fluxes to the *PID* value, an improved discrimination between leptons and hadrons is obtained. The histograms rely on the 05c2 production after applying data quality cuts.

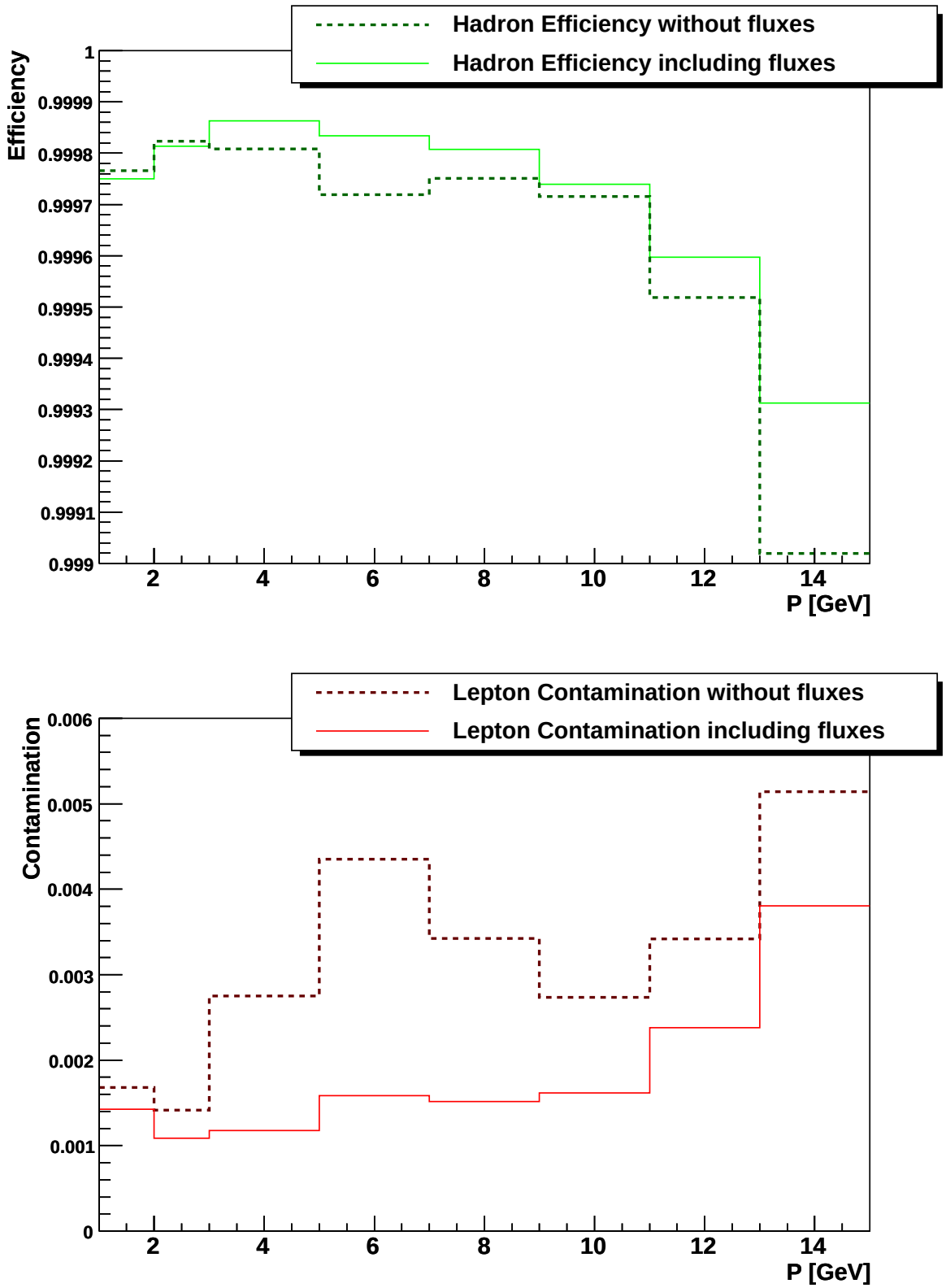


**Figure 4.5:** Lepton efficiency and hadron contamination of Inclusive Hadron sample calculated using Equations (4.4.10) and (4.4.9). The histograms rely on the 05c2 production after applying data quality cuts.

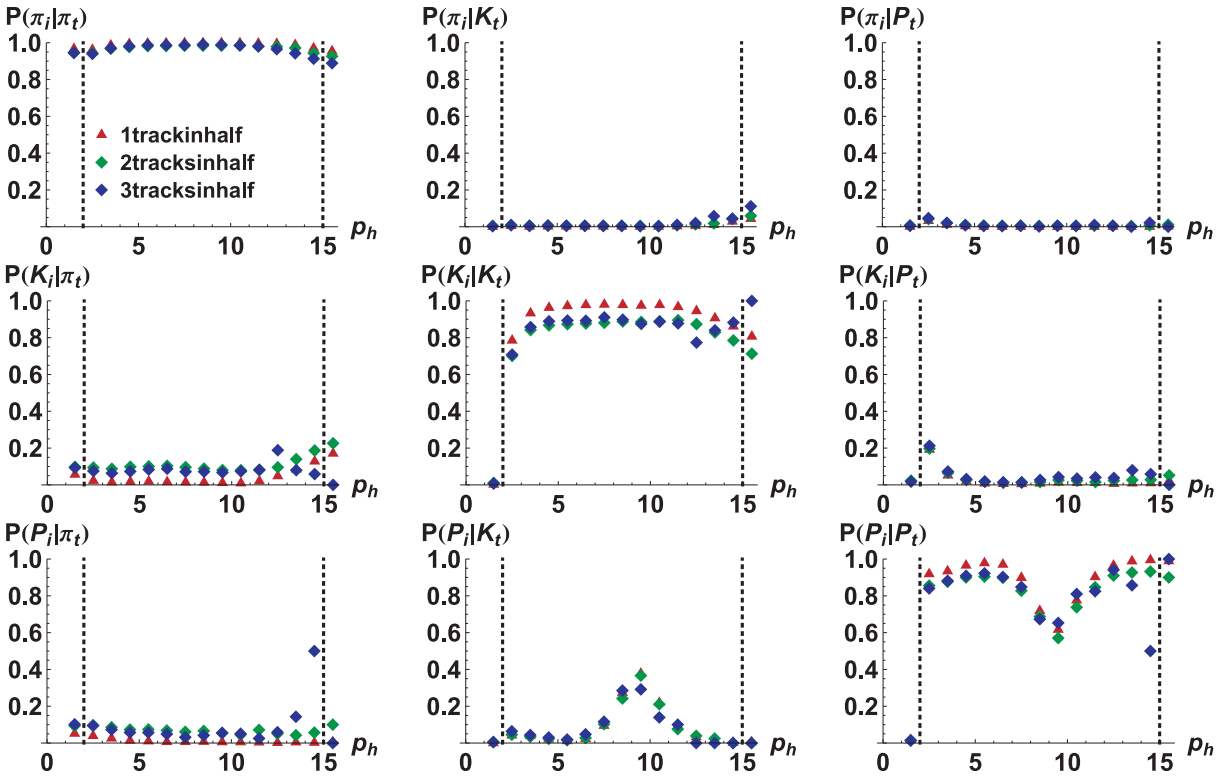


**Figure 4.6:** The $P$–matrix, dependent on the momentum of the particle, for the HERMES RICH detector obtained from a Monte Carlo simulation [LH08]. Plotted are the conditional probabilities that a given hadron of true type $h_t$ is identified as a pion, kaon, or proton, respectively. The different plot symbols represent the dependence on the number of charged particle tracks per detector half.

### Charged Hadron Identification

The dual-radiator ring imaging Cerenkov counter (RICH) is the subsystem which is responsible for the discrimination between different hadron types. Because of its carefully selected radiator materials, it has the ability to differentiate kaons, and protons over the momentum range $2\,\mathrm{GeV} < p < 15\,\mathrm{GeV}$, for pions even in the range $1\,\mathrm{GeV} < p < 15\,\mathrm{GeV}$. With the RICH, a probability is produced for each of the three possible hypotheses: pion, kaon, or proton. As described below, weights are calculated for each hypothesis and fractional counts are then recorded in yield histograms during data analysis.
The success of the identification of a hadron track is assured by requiring a positive value of the quality parameter $Qp$ which is defined as the logarithm of the likelihood ratio of the most and the second most likely hadron types, $h_1$ and $h_2$:

$$Qp = \log_{10} \frac{P(h_1)}{P(h_2)} > 0. \tag{4.4.14}$$

If the identification algorithm could not find a most probable hadron type the quality parameter is set to zero.

In order to account for inefficiencies and hadron identification contaminations of the RICH detector, a $\mathcal{P}$-matrix is provided by the HERMES RICH group which is used to produce weights for all different hypotheses, providing more accurate yields [LH08]. The $\mathcal{P}$-matrix contains the conditional probabilities, $P(h_i|h_t)$ that a hadron of true identity, $h_t$, is identified by the RICH as being of type $h_i$. The $\mathcal{P}$-matrix is produced by comparing RICH-identifed Monte Carlo tracks with their true identities, and it is binned in the two variables on which it has been found to depend: track momentum, and the multiplicity of tracks in the relevant half of the detector. The probability entries of the $\mathcal{P}$-matrix are plotted in Figure 4.6. From this one can write:

$$\vec{N}_i = P\vec{N}_t, \tag{4.4.15}$$

where

$$\vec{N}_i = \begin{pmatrix} N_i^\pi \\ N_i^K \\ N_i^p \end{pmatrix}, \vec{N}_t = \begin{pmatrix} N_t^\pi \\ N_t^K \\ N_t^p \end{pmatrix} \quad \text{and} \quad P = \begin{pmatrix} P(\pi_i|\pi_t) & P(K_i|\pi_t) & P(p_i|\pi_t) \\ P(\pi_i|K_t) & P(K_i|K_t) & P(p_i|K_t) \\ P(\pi_i|p_t) & P(K_i|p_t) & P(p_i|p_t) \end{pmatrix}, \tag{4.4.16}$$

where $N^h_{i(t)}$ being an identified (true) yield of hadrons of type $h$. From Equation (4.4.15), one can see then that a yield of identified hadrons can be mapped back to the true yield using the inverted $\mathcal{P}$-matrix as follows:

$$\vec{N}_t = \mathcal{P}^{-1}\vec{N}_i. \tag{4.4.17}$$

Because of this, the inverted $\mathcal{P}$-matrix can be applied to the RICH's hypothesis (a yield vector, if you like, with a single column as it's only non-zero entry) to produce the vector of weights to be added to the final hadron yield histograms. It should be noted that unlike the $\mathcal{P}$-matrix, its inverse $\mathcal{P}^{-1}$ does not contain probabilities. Its entries are not necessarily bounded by one and can also be negative. For instance, a track identified as $h_i$ is weighted by $(\mathcal{P}^{-1})_{\pi_t|h_i}$ in the true pion count rate and by $(\mathcal{P}^{-1})_{K_t|h_i}$ in the true kaon count rate. The sum of these weights over all tracks $l = \sum_{l_i} l_i$ with identified hadron type $(h_i)_{l_i}$ yields the number of true hadrons:

$$N^h_t = \sum_{l_i} (\mathcal{P}^{-1})_{h_t,(h_i)_{l_i}} = \sum_{l_i} \omega_{h,l_i} \tag{4.4.18}$$

used in the analysis.

### 4.4.3 Kinematic Cuts

As we are not interested in scattered leptons, e.g. from (SI)DIS processes, the selected cuts are very limited and listed in Table 4.5. The cuts applied to the momenta of the detected pions and kaons are due to the RICH detector. A clear hadron discrimination can only be accomplished for pions in the momentum range $1\,\text{GeV} < p < 15\,\text{GeV}$ and for kaons in the range $1\,\text{GeV} < p < 15\,\text{GeV}$ [LH08]. As we only look at Inclusive Charged Hadrons we lose all the information about the scattered lepton and , thus, of the virtual photon. The usual cuts on (SI)DIS-events, like four–momentum transfer of more than $1\,\text{GeV}^2$, i.e., larger than the squared proton mass, cannot be applied. Furthermore, events from the resonance region $W < 4\,\text{GeV}^2$ are included as well in the data sample. As a consequence, we have to keep in mind that the major contribution on our selected data sample come from the photoproduction region. The resulting distributions on kinematic variables which are relevant for our analysis are depicted in Figure 4.7.

| | Cut |
|---|---|
| Pion Momentum | $1\,\text{GeV} \leq p_{\text{Pion}} \leq 15\,\text{GeV}$ |
| Kaon Momentum | $2\,\text{GeV} \leq p_{\text{Kaon}} \leq 15\,\text{GeV}$ |

**Table 4.5:** The kinematic cuts applied to the detected charged particles.

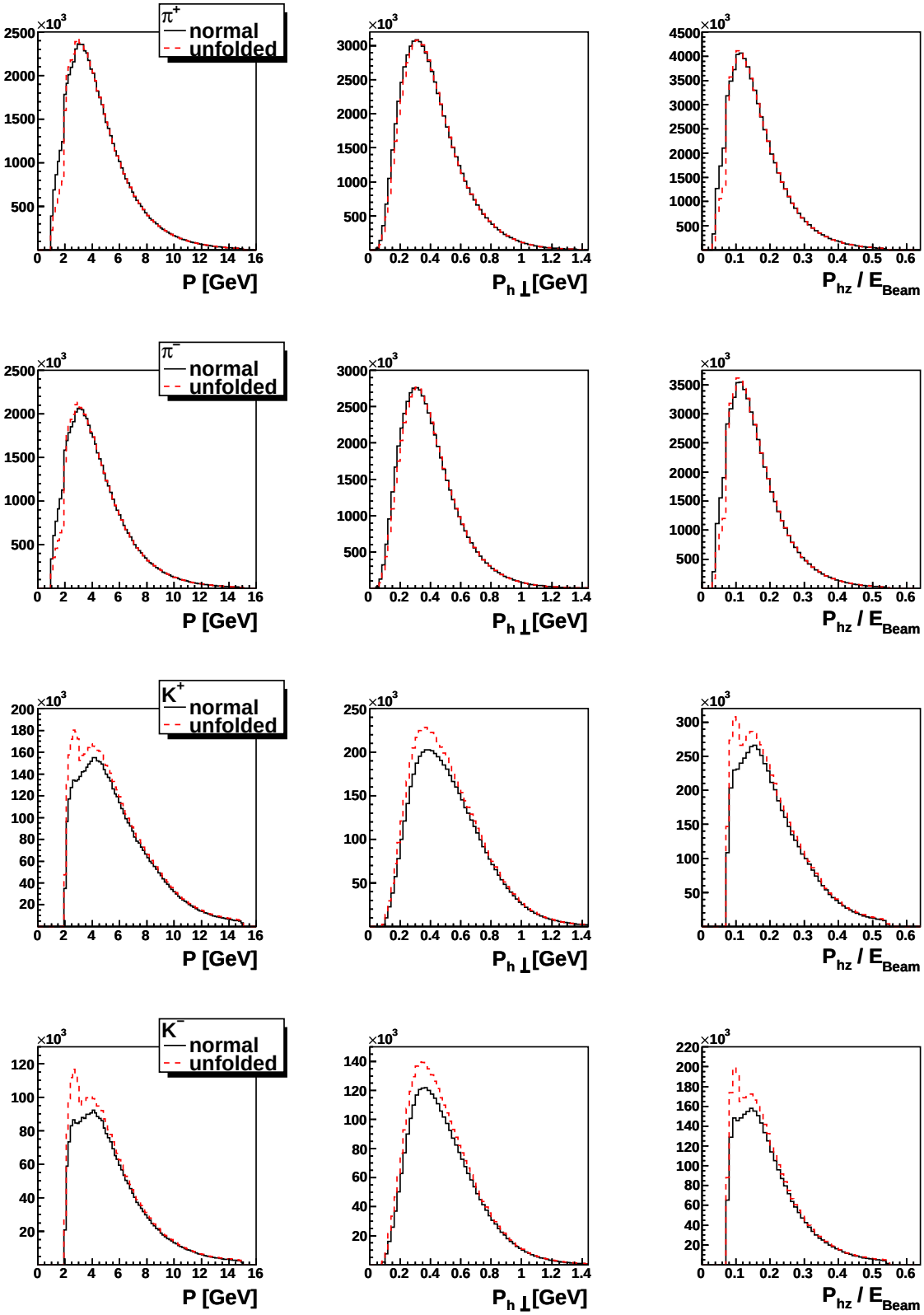


**Figure 4.7:** The distributions of the four hadron types $\pi^+$, $\pi^-$, $K^+$ and $K^-$ (from top to bottom) in the variables $p$, $P_{h\perp}$ and $\frac{p_z}{E_{\text{Beam}}}$ (from left to right). The black lines correspond to the unweighted distributions, the red lines to the weighted distributions making use of the EVT weights (cf. Subsection 4.4.2, "Charged Hadron Identification"). The distributions base on the complete 2002–2005 data set after applying both geometric and kinematic cuts.

### 4.4.4 Yields of Inclusive Charged Hadrons

All the hadron tracks which have passed both the geometric and the kinematic cuts contribute to the final yields to be used for the extraction of the azimuthal asymmetries. Table 4.6 reports the corresponding yileds for each hadron type $h$ and each production. The resulting statistics are extraordinary big and rather unique for a HERMES analyis. Thus the management of this huge amount of data was one of the major challenges during the analyis.

| Production | Nr. of Runs | Nr. of Bursts | Particle-Type | Nr. of Particles (no EVT-sums!) |
|---|---|---|---|---|
| 02c1 | 2.870 | 235.111 | $\pi^+$ | 4.179.233 |
| | | | $\pi^-$ | 3.566.769 |
| | | | $K^+$ | 351.561 |
| | | | $K^-$ | 188.819 |
| 03c1 | 1.227 | 191.531 | $\pi^+$ | 3.160.424 |
| | | | $\pi^-$ | 2.677.996 |
| | | | $K^+$ | 263.817 |
| | | | $K^-$ | 141.065 |
| 04c1 | 11.579 | 524.814 | $\pi^+$ | 18.896.594 |
| | | | $\pi^-$ | 16.080.406 |
| | | | $K^+$ | 1.564.830 |
| | | | $K^-$ | 841.089 |
| 05c2 | 30.719 | 1.050.906 | $\pi^+$ | 40.092.145 |
| | | | $\pi^-$ | 34.416.158 |
| | | | $K^+$ | 3.332.584 |
| | | | $K^-$ | 1.819.223 |

**Table 4.6:** Final yields for Inclusive Charged Hadrons after passing all track level cuts. Note, that, in this Table, the sums are no sums of EVT weight from the $\mathcal{P}$-matrix. This has nearly no influence on the pion yields, but the kaon yields decrease between 20–30% compared to the EVT unfolded yields.

## 4.5 Systematic Studies

In order to test the stability of the results and to estimate a systematic error which accounts for all the possible sources of biases, the analysing power $A_{UT}$ can be extracted under different conditions. The systematic studies reported in the next Subsections are based on the full HERMES data set with a transversely polarized target (data productions 02c1, 03c1, 04c1 and 05c2). The subsequent Subsections only show some selected studies on a qualitative base. A complete systematic study which accounts for all possible sources of errors would definetly exceed the extent of this thesis. For a complete systematic study one would have to consider the following scenarios:

- Contribution of other azimuthal moments, like $\sin(2\phi)$ amplitudes
- Hadron identification with the RICH: usage of different sets of $\mathcal{P}$-matrices
- Effects of beam polarization
- Fake asymmetries
- Detector acceptance and smearing effects based on Monte Carlo simulations

### 4.5.1 Effect of the Target Magnet Correcion (TMC)

The measurement of the analysing power $A_{UT}$ requires a transversely polarised target. The transverse holding field which provides the polarisation axis for the nuclei causes a bending of the trajectories of the produced hadrons due to the Lorentz force. The reconstructed partial particle tracks in front of the spectrometer magnet do not yield the correct vertex positions and scattering angles when they are extrapolated into the target cell by a straight line. Two different TMC methods are used for the correction of the obtained positions and angles which regain the reconstruction resolution without transverse magnet field almost completely. Even though the correction of the vertex positions and scattering angles is possible and always applied, the influence of uncorrected particle tracks on the extracted asymmetry amplitudes is studied. The amplitudes with and without tracking corrections are compared, for pions in Figure 4.8 and for kaons in Figure 4.9. Although differences in the statistical uncertainties are visible, the conclusion of the extracted amplitudes remains unchanged. Thus, the correction of the influence of the magnetic field is necessary but has not a strong impact on the extracted asymmetry amplitudes. To allow the identification of systematic discrepancies, deviations between the two data taking periods are computed as:

$$\text{deviation} = \frac{A_{UT}^{\sin\phi}(\text{TMC}) - A_{UT}^{\sin\phi}(\text{no TMC})}{\sqrt{\sigma^2(\text{TMC}) + \sigma^2(\text{no TMC})}}. \tag{4.5.1}$$

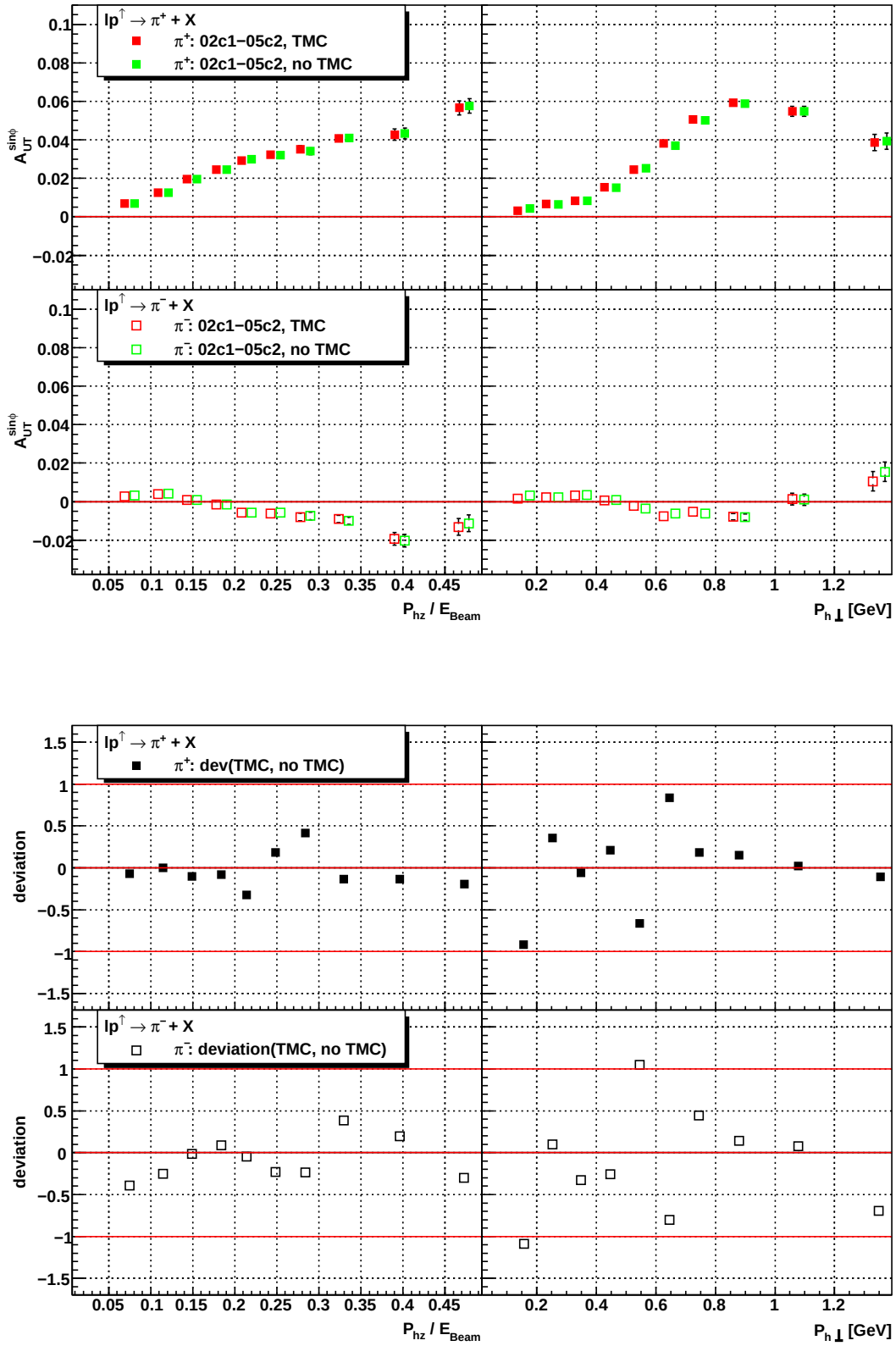


**Figure 4.8:** Comparison of the asymmetry amplitudes for $\pi^+$ and $\pi^-$ with and without tracking corrections for the transverse target field.

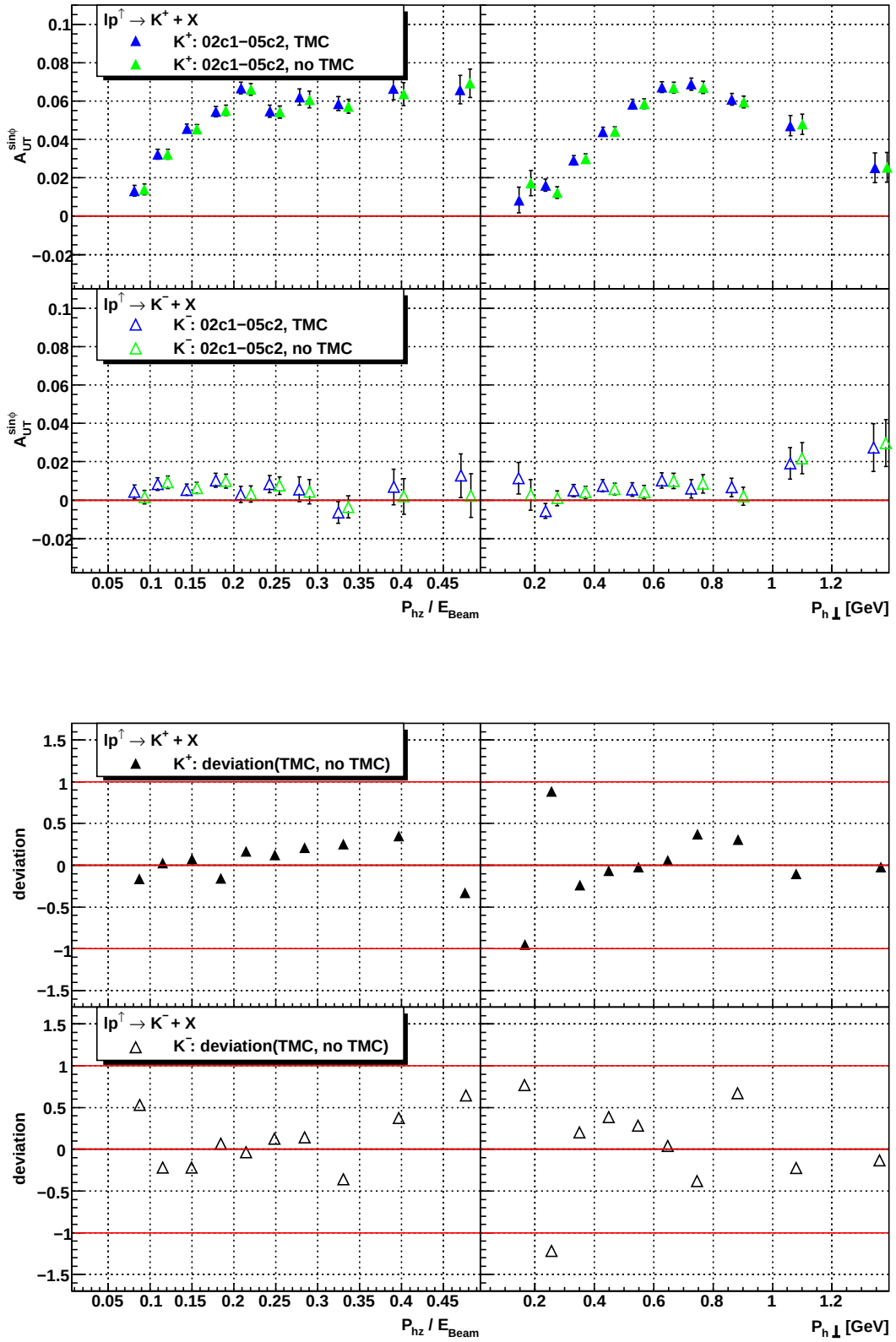


**Figure 4.9:** Comparison of the asymmetry amplitudes for $K^+$ and $K^-$ with and without tracking corrections for the transverse target field.

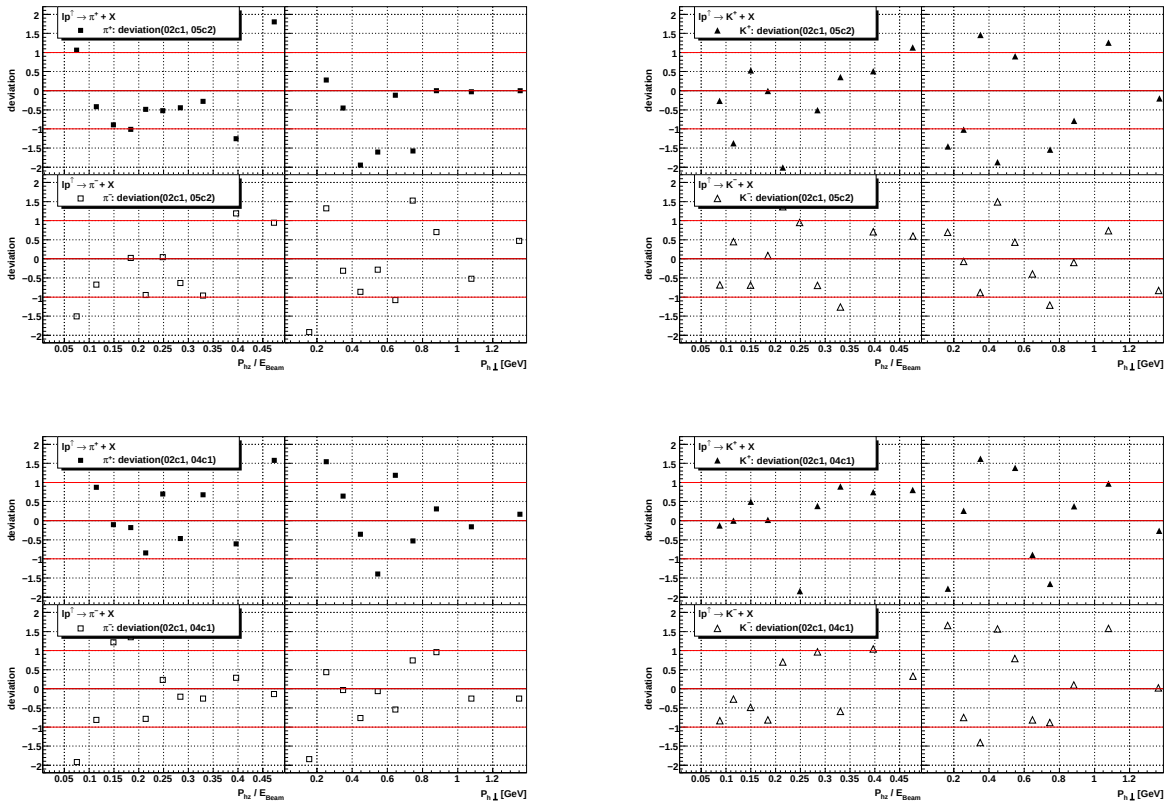


**Figure 4.10:** Deviations between the periods 02c1/05c2 and 02c1/04c1 (from top to bottom) for Pions (left panel) and Kaons (right panel).

### 4.5.2 Compatiblity between productions

The data analysed in this chapter were recorded during a period over four years. Within this time changes of the HERMES spectrometer, e.g., in the alignment or the efficiencies of the detectors, may occur which can influence the extracted asymmetry amplitudes. As a check, results from the single periods are compared with each other. To identify systematic discrepancies, deviations between the two periods are computed as:

$$\text{deviation} = \frac{A_{UT}^{\sin\phi}(\text{Period1}) - A_{UT}^{\sin\phi}(\text{Period2})}{\sqrt{\sigma^2(\text{Period1}) + \sigma^2(\text{Period2})}}. \tag{4.5.2}$$

Figures 4.10–4.11 show that they fluctuate around zero and do not show systematic trends. Consequently, the data taking periods are consistent with each other.
A complementary way to check the compatibilites of the data sets is to compare the corresponding kinematic distributions, e.g. in $P_{h\perp}$. The Ratios of the average values per bin allow to reveal systematic trends as well. Figures 4.12–4.14 manifest the results obtained from the previous, direct check on the asymmetries.

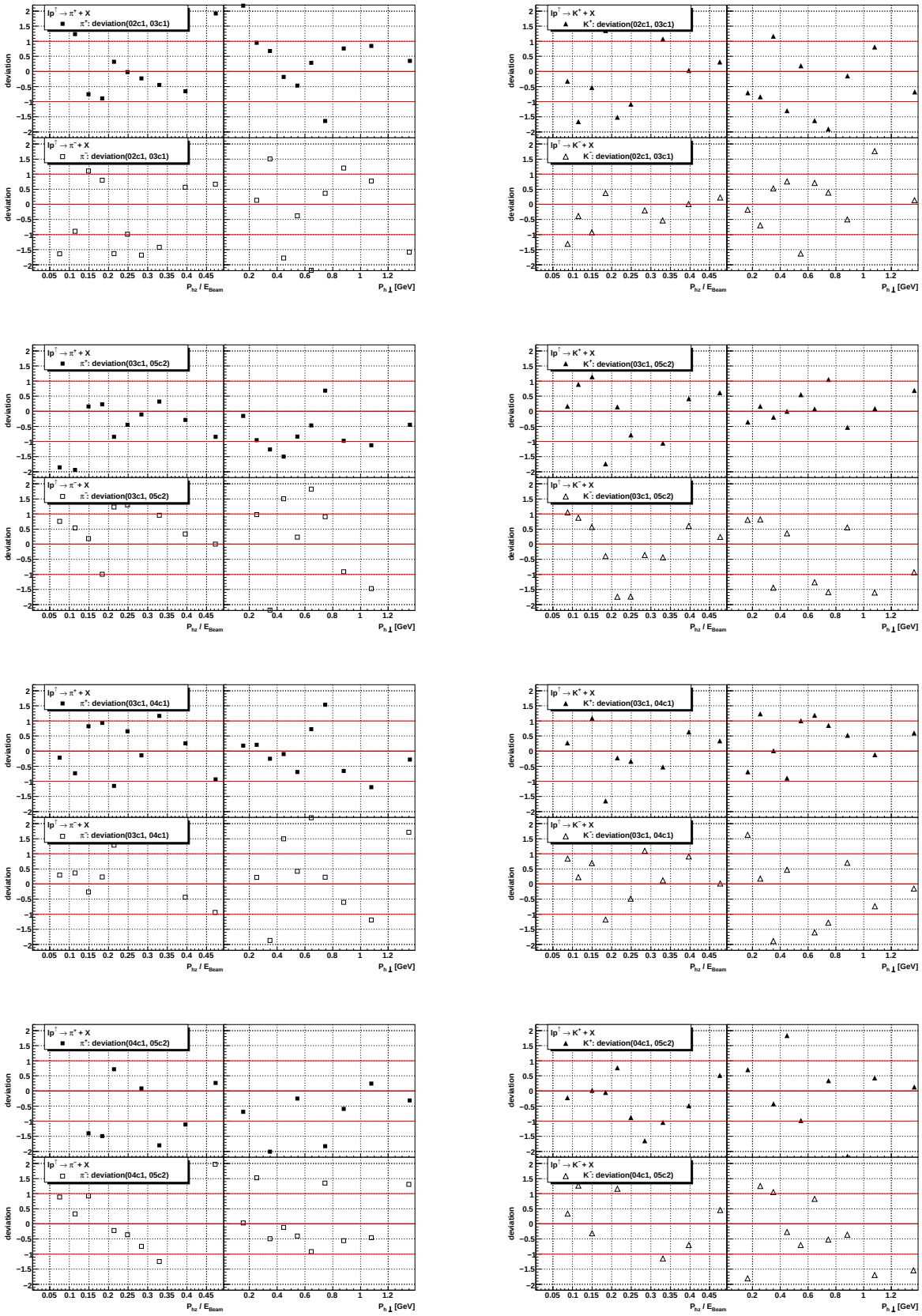


**Figure 4.11:** Deviations between the periods 02c1/03c1, 03c1/04c1, 03c1/05c2, 04c1/05c2 (from top to bottom) for Pions (left panel) and Kaons (right panel).

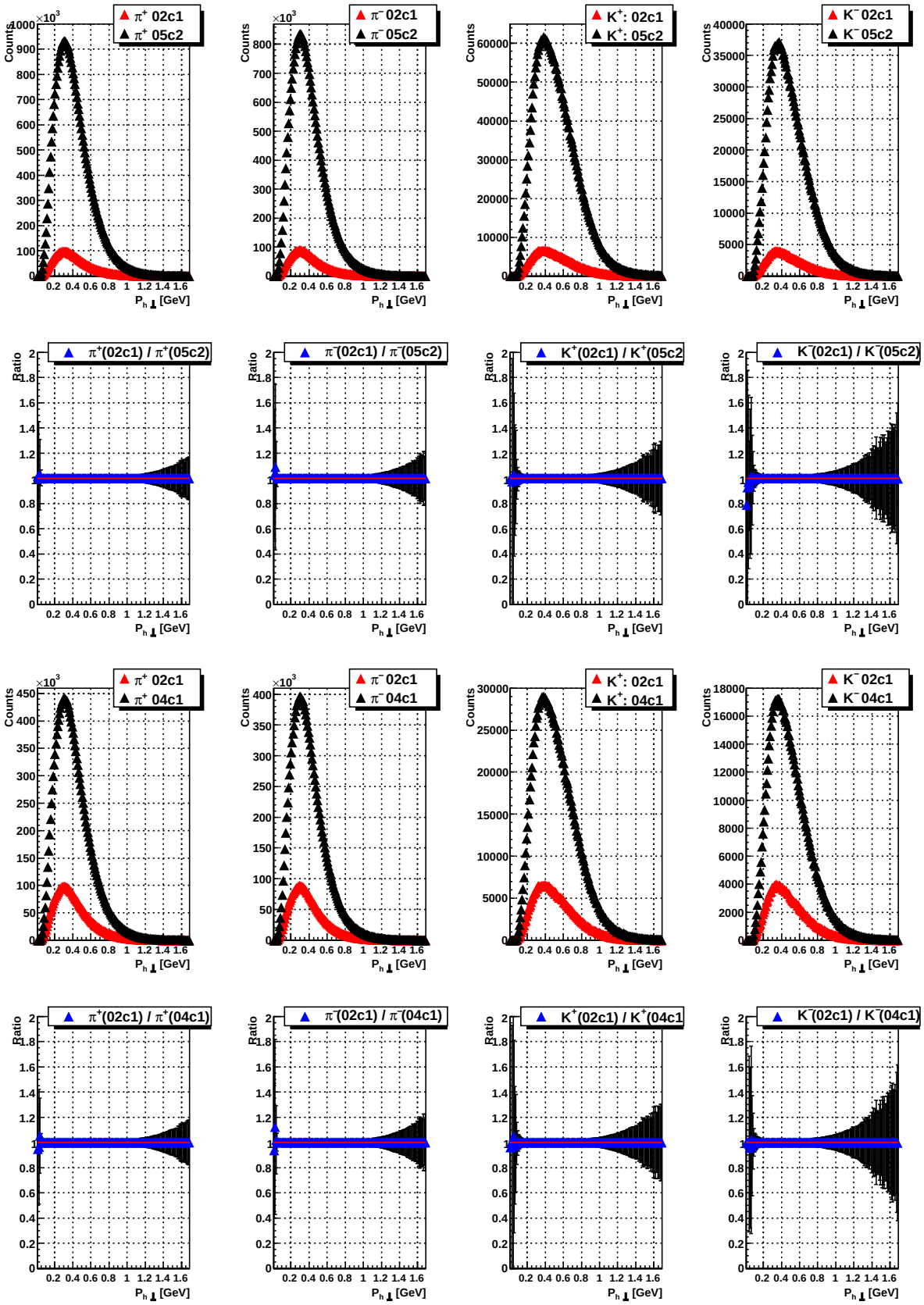


**Figure 4.12:** Ratios of the distributions on $P_{h\perp}$ for Pions and Kaons. The productions 02c1/05c2 and 02c1/04c1 (from top to bottom) are compared.

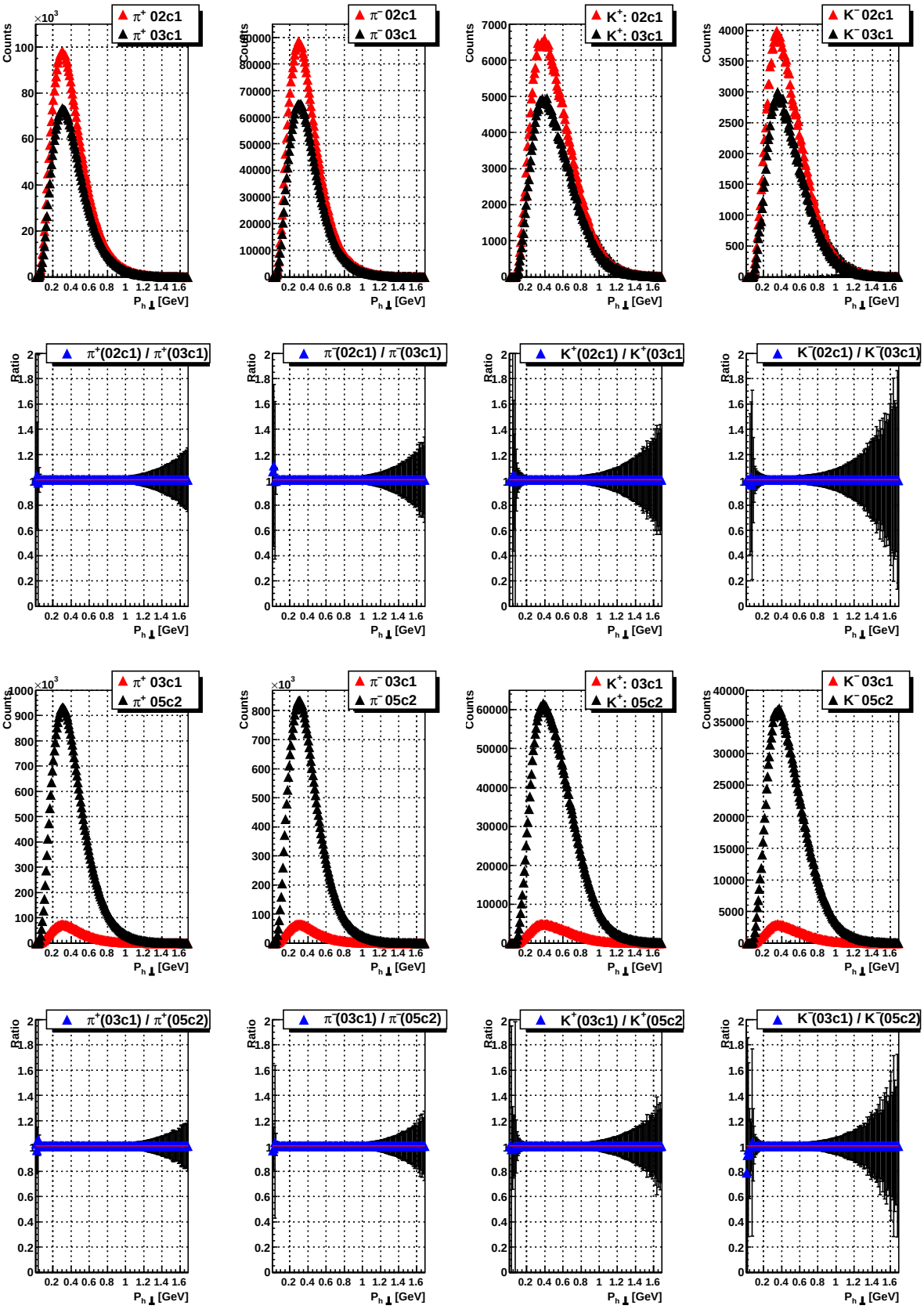


**Figure 4.13:** Ratios of the distributions on $P_{h\perp}$ for Pions and Kaons. The productions 02c1/03c1 and 03c1/04c1 (from top to bottom) are compared.

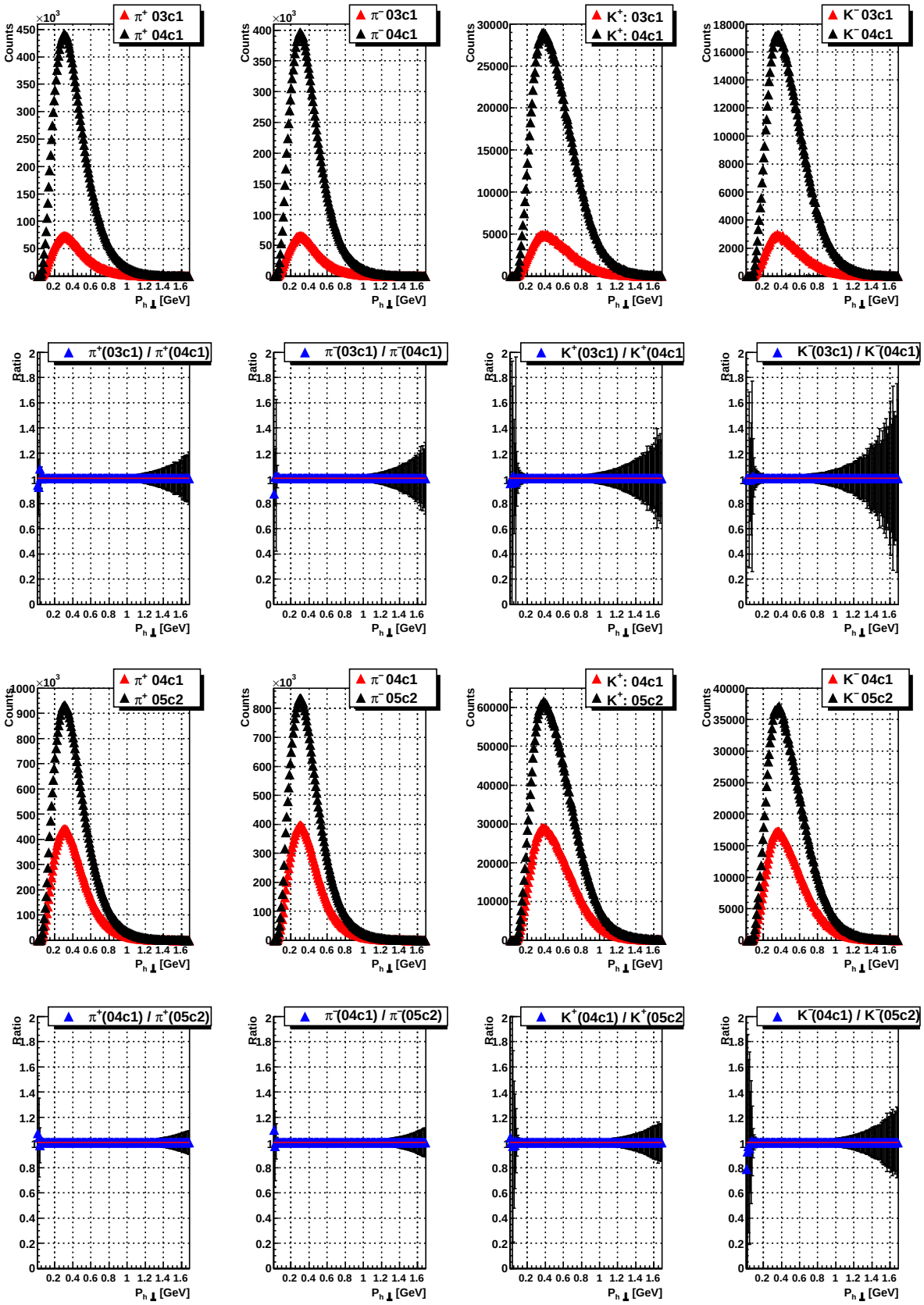


**Figure 4.14:** Ratios of the distributions on $P_{h\perp}$ for Pions and Kaons. The productions 03c1/04c1 and 04c1/05c2 (from top to bottom) are compared.

# Chapter 5

# Results and Discussion

## 5.1 The Integrated Analysing Power $A_{UT}$

The extracted data set which contains all data taken on a transversely polarised hydrogen target at HERMES contains $\sim 61 \cdot 10^6$ positive pions, $\sim 43 \cdot 10^6$ negatively charged pions, $\sim 5.5 \cdot 10^6$ negatively charged kaons, $\sim 2.9 \cdot 10^6$ negatively charged kaons. The average kinematics of the successfully identified particels is listed in Table 5.1.

| Particle Type | $\langle P_{h\perp} \rangle$ | $\langle P_{hz}/E_{Beam} \rangle$ | Yields |
|---|---|---|---|
| $\pi^+$ | 0.411 | 0.161 | $\sim 61 \cdot 10^6$ |
| $\pi^-$ | 0.398 | 0.158 | $\sim 43 \cdot 10^6$ |
| $K^+$ | 0.526 | 0.207 | $\sim 5.5 \cdot 10^6$ |
| $K^-$ | 0.493 | 0.105 | $\sim 2.9 \cdot 10^6$ |

**Table 5.1:** Overview of the averaged kinematic variables of charged mesons of the data taking period on a transversely polarised from 2002 until 2005.

The resulting integrated analysing powers $A_{UT}$ for inclusive charged pions an kaons can be found in Table 5.2. Integrated asymmetries refer to the pure left-right asymmetry without accounting for kinematic dependencies. Thus an integrated measurement averages over the whole kinematic range.

| Particle Type | $A_{UT}$ |
|---|---|
| $\pi^+$ | $0.0189 \pm 0.0003$ |
| $\pi^-$ | $0.0001 \pm 0.0003$ |
| $K^+$ | $0.0448 \pm 0.0009$ |
| $K^-$ | $0.0060 \pm 0.0001$ |

**Table 5.2:** Overview of the fully integrated analysing power $A_{UT}$ for inclusive charged pions and kaons. Systematic errors are not taken into account.

The results show significant positive integrated asymmetries for positvely charged kaons and pions. The measured asymmetry for positive kaons is larger than the asymmetry of positive pions by a factor of 2. The fully integrated analysing power for negative pions equals zero. Negative kaons, though, show a slightly positive trend. Figure 5.1 shows the integrated analysing powers for all charged pions and kaons. Although we do not yet restrict the

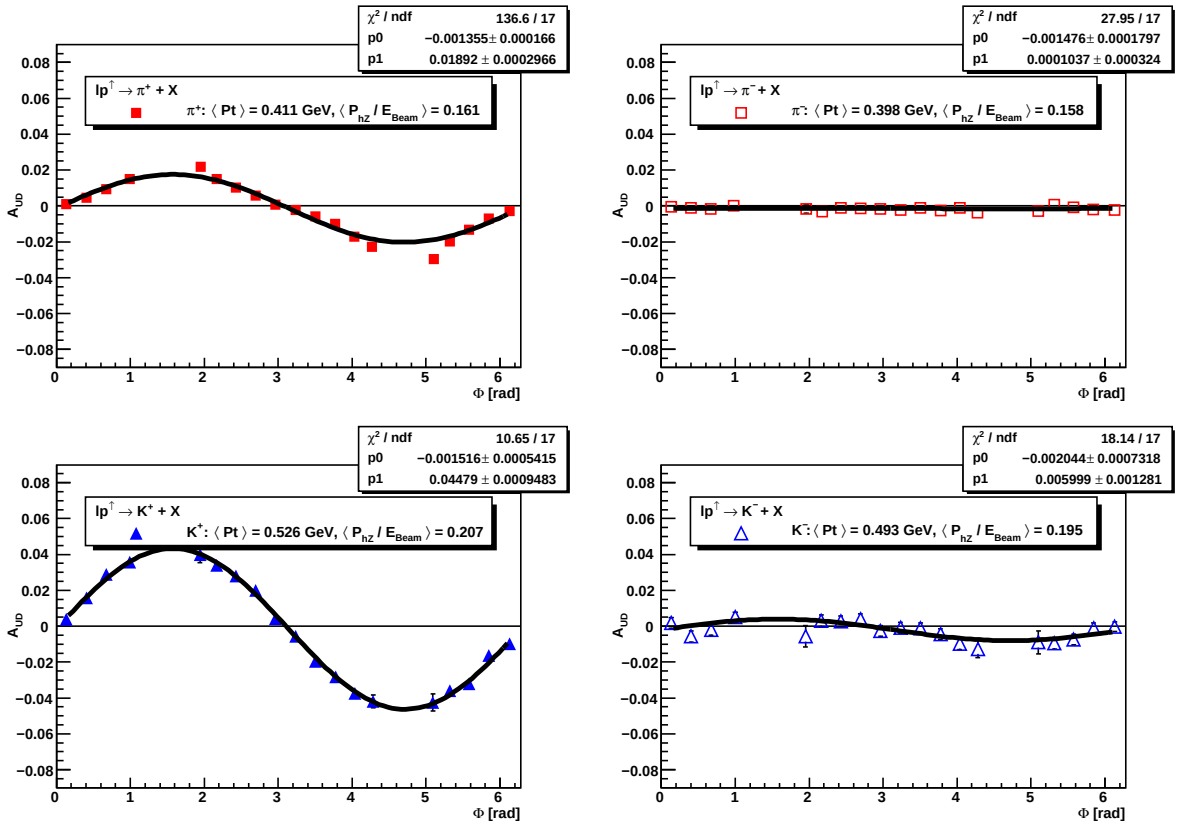


**Figure 5.1:** The integrated Fourier amplitudes of charged pions and kaons of the complete transverse data set from 2002 until 2005. The statistical errors cannot be resolved in this plot. Therefore, we refer to table 5.1.

analysing power to a certain kinematic regime, the predicted sine modulations are already visible and significant (for positively charged mesons). For further studies on the underlying physics processes it is necessary to investigate the kinematic-dependent analysing power $A_{UT}$ as a function of $P_{h\perp}$ and $P_{hz}/E_{Beam}$.

## 5.2 The Analysing Power $A_{UT}(P_{h\perp}, P_{hz}/E_{Beam})$

The discussion presented in this Section refers to Figure 5.2. The analying power for postive pions is positive over the complete observed kinematic range. Studying the $P_{h\perp}$-dependence reveals the following. The asymmetry sets in after exceeding a threshold of $P_{h\perp} \sim 0.4\,\text{GeV}$ and peaks in the region between 0.8 GeV and 1.0 GeV at at a maximum level of $A_{UT} \sim 6\%$. The $P_{hz}/E_{Beam}$-dependent asymmetry rises constantly, nearly linearly. The positive $\pi^+$-asymmetries follow the trend of the theoretical predictions of the Anselmino group (cf. Figure 2.16, [ABM+09]) ($8\% \leq A_{UT}^{theory} \leq 13\%$) but differ in a $\sim 50\%$ smaller asymmetry..
For negative pions no clear $P_{h\perp}$-dependent asymmetry can be observed. The $P_{hz}/E_{Beam}$-dependent analysing power shows a slightly negative trend, though, with a maximum value at $A_{UT} \sim 2\%$. This negative asymmetry might be caused by the Collins effect (cf. Figure 2.15). Our asymmetries for negative pions contradict the calculations of the Anselmino group 2.16 which predict large negative asymmetries for negative pions.
For positive kaons, the analysing power is similar to the one of positive pions. It is clearly visible that the asymmetry rises more steeply in $P_{hz}/E_{Beam}$ compared to the pion-case. The asymmetry seems to saturate at $A_{UT} \sim 6\%$ above $P_{hz}/E_{Beam} \sim 0.2$. The $P_{h\perp}$-dependent $A_{UT}$-threshold is below 0.2 GeV which can be explained by the bigger mass of the kaon compared to the pion mass. The analysing power $A_{UT}$ peaks between 0.6 GeV and 0.8 GeV at a maximum value $A_{UT} \sim 7\%$. Thus, the maximum asymmetry of the positively charged kaons is larger than the one of positive pions. The asymmetry of negative kaons does not show any specific features. It equals zero over a wide kinematic range, both in $P_{h\perp}$ and in $P_{hz}/E_{Beam}$. For $P_{h\perp} > 1.0\,\text{GeV}$ a slightly positive asymmetry above $A_{UT} \sim 2\%$ is observable. In conclusion, we can state to be within the trend of measured Sivers amplitudes at HERMES which were collecetd in a SIDIS region (cf. Figure 2.15 and Figure 2.14). The analysing power $A_{UT}$ is

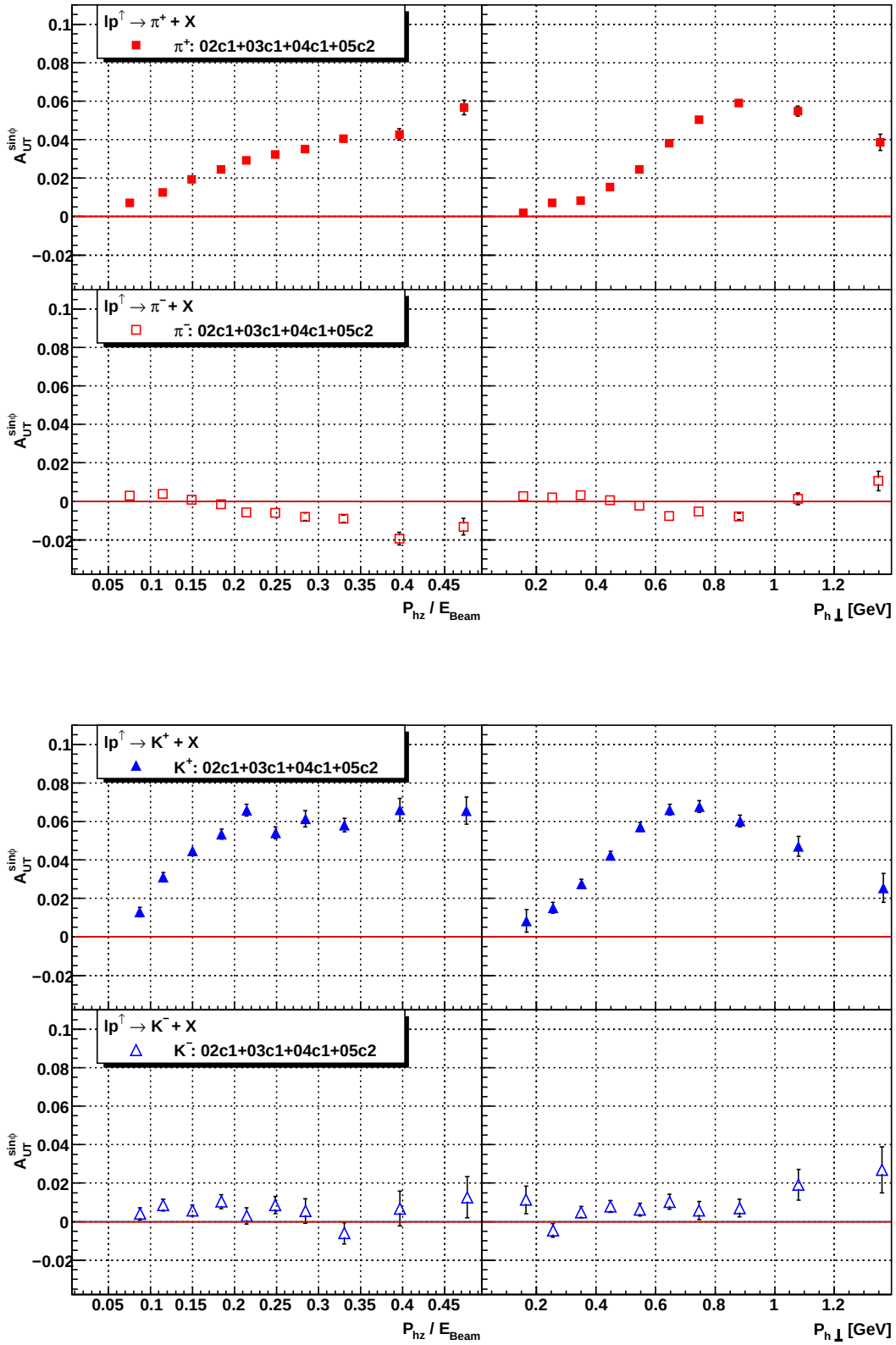


**Figure 5.2:** The analysing power $A_{UT}$ for charged pions (top-panel) and kaons (bottom-panel). For charged mesons there is clear positive asymmetry. The results for negatively charged kaons is compatible with zero, for negative pions there's a slightly negative trend.

not able to reproduce the large asymmetry difference of $\sim 5\%$ between the Sivers amplitudes of positive pions and kaons.

### The High-$P_{h\perp}$ Behaviour

This discussion refers to Figure 5.3. In order to investigate the behaviour in the High-$P_{h\perp}$-region, the cut $P_{h\perp} > 0.65\,\text{GeV}$ was applied. As our analysis luckily provides enough statistics, we further chose a finer $P_{h\perp}$-binning. For positive pions, this cut gives rise to a $P_{hz}/E_{Beam}$-dependent asymmetry with surprisingly constant values above $A_{UT} \sim 4\%$. The peak region around $P_{h\perp} \sim 0.8\,\text{GeV}$ is nicely shaped by the cut. This confirms the rise of the analysing power $A_{UT}$ in the "soft" $P_{h\perp}$-regime below $P_{h\perp} \sim 0.8\,\text{GeV}$ and the drop in the "hard" $P_{h\perp}$-region above $P_{h\perp} \sim 0.8\,\text{GeV}$. This also applies for the analysing power of positive kaons with the difference that the impact of the new binning on the asymmetry is not so large in the $P_{hz}/E_{Beam}$-dependence.
For negatively charged mesons no additional features can be resolved by this finer High-$P_{h\perp}$binng.

## 5.3 The Disentanglement of Sub-Processes

The peak in the asymmetries for positevly charged mesons indicates an overlap of different physics processes contributing to the observed overall asymmetry. For a better understanding of the underlying processes it is necessary to define regions which allow an unique theoretical description of the observed SSA. To achieve this ones has to apply (anti-)tagging cuts on the selection of the relevant events. We, thus, decided for two regions. The first is the SIDIS-region which is investigated in recent studies on the Collins- and Sivers-moments at HERMES. The SIDIS kinematic region can be accessed by means of pQCD.
The second sub-process of interest is the photoprodction region. In this region only soft events are included (meaning events for the region $Q^2 \ll 1\,\text{GeV}^2$). So far, no theories or models exist which are capable to deduce significant SSAs in the photoproduction-regime. The so-called vector meson dominance (VMD) model [Sak69] provides a phenomenological access to this kinematic regime. In the deep–inelastic scattering process, the exchanged virtual photon interacts with a quark of the nucleon. Besides the so–called bare part of the photon, which couples to the electromagnetic charge of the quarks, the virtual photon can also fluctuate into aquark–antiquark pair. This pair can live long enough to create a cloud of gluons around the quarks, such that the state develops into a hadronic state which then interacts with the nucleon. This interaction of the hadronic part of the photon with the nucleon can be described only phenomenologically in terms of models for hadron–hadron interactions. In the VMD model, the hadronic part of the photon is interpreted as fluctuations into the vector mesons $\rho^0$, $\omega$ and $\phi$. Besides the hadronic part, the photon exhibits also a so–called anomalous part which is a fluctuation into a quark–antiquark pair with a larger virtuality than the vector meson. Alternatively, this can be viewed as an excited higher resonance of a vector meson which scatters from the nucleon into a vector meson. These states are taken into account by the Generalised VMD (GVMD) [SS72].

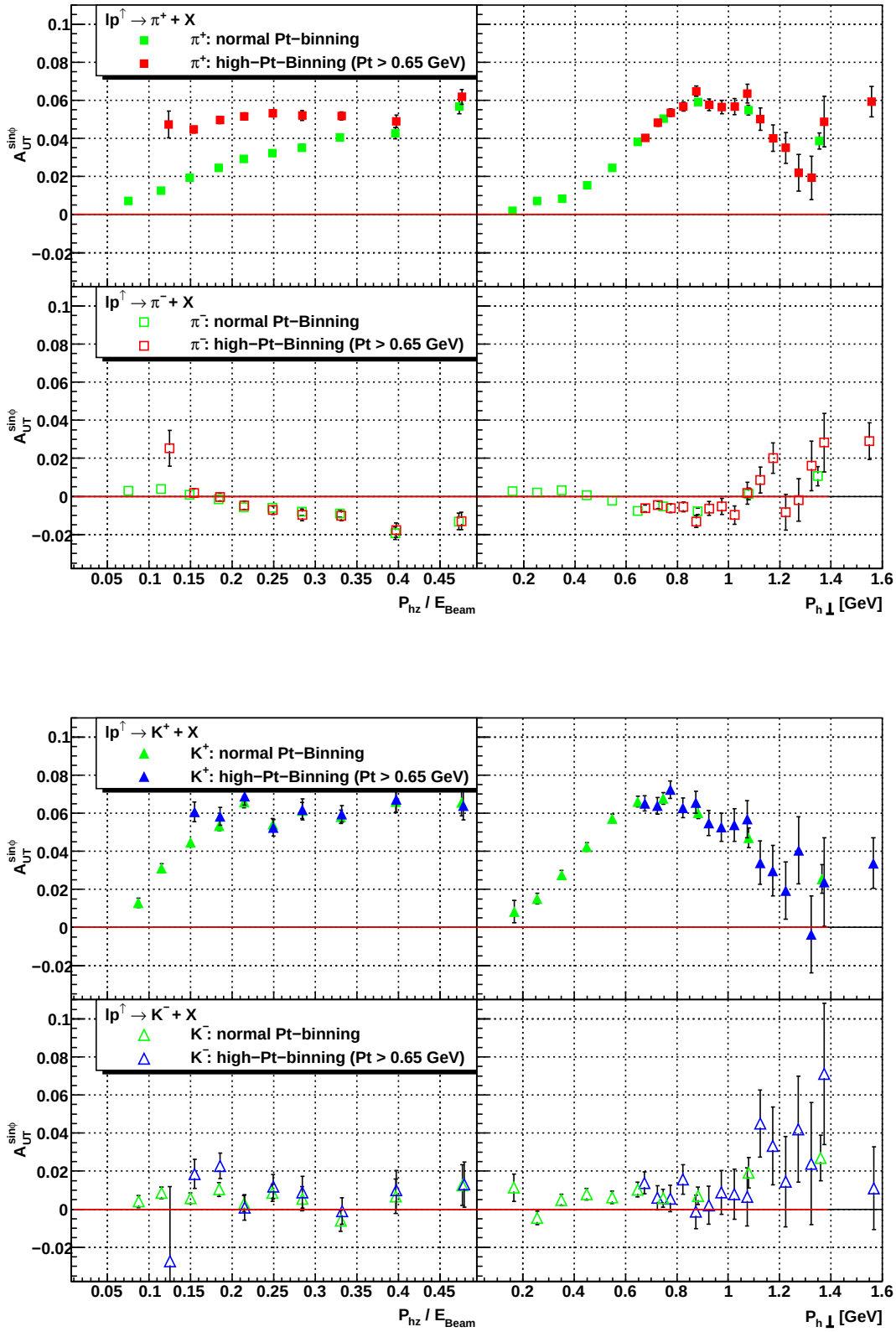


**Figure 5.3:** The analysing power $A_{UT}$ for charged pions (top-panel) and kaons (bottom-panel). The High-$P_{h\perp}$ is studied (blue and red points) and directly compared to the results without a high-$P_{h\perp}$-cut (green data points).

### 5.3.1 The SIDIS-Region

The following discussion refers to the results shown in Figure 5.4. The selection of events was performed the following way. We only took events with at least one detected lepton. When the leading (scattered) lepton fulfilled the cuts $Q^2 > 1\,\mathrm{GeV}^2$, $W^2 > 10\,\mathrm{GeV}^2$, $0.1 < y < 0.95$ and $0.023 < x_B < 0.4$ it was accepted and all produced hadrons from the corresponding event were included in our analysis. These cuts reduce our statistics signifantly.
For positive pions a rise of the analysing power $A_{UT}$ both in $P_{h\perp}$ and in $P_{hz}/E_{Beam}$ can be observed, in the $P_{hz}/E_{Beam}$-dependent asymmetry this rise is nearly linear though. The turning point of the purely inclusive measurement between 0.8 GeV and 1.0 GeV is not caused by events from the SIDIS region. The asymmetry reaches a maximum value of $A_{UT} \sim 15\%$ in the hard $P_{h\perp}$-regime. This result is in better agreement with the prediction of Anselmino et al. [ABM$^+$09], cf. Figure 2.16. In the soft $P_{h\perp}$-region the asymmetry nearly equals the results from the purely inclusive measurement. For negative pions we observe a negative asymmetry. This is in better agreement with the theoretical predictions presented in [ABM$^+$09], as well. Nevertheless, one has to keep in mind that this negative $\pi^-$-asymmetry can be a result of a superposition of Sivers and Collins moments within the HERMES acceptance.
In the SIDIS-Regime, the analysing power of $K^+$ behaves in a very similar way to the one of the positive pions. The maximum value of the asymmetry is $A_{UT} \sim 15\%$ in the hard $P_{h\perp}$-regime, though. The asymmetry of negative kaons equals zero within the statistical uncertainties over the complete kinematic range.
In conclusion, we are capable to state that the main contributions to the positive analysing power $A_{UT}$ in inclusive hadron production is caused by the leading-twist Sivers DF $f_{1T}^{\perp q}$. As a consequence, the leading twist character of the Sivers DF is emphasized. Thus the suppression of the large asymmetries caused by SIDIS processes in the hard $P_{h\perp}$-regime in Figure 5.2 must be caused by higher-twist effects. In the following Subsection we will address this low-energetic kinematic regime and look at the resulting analysing power $A_{UT}$.

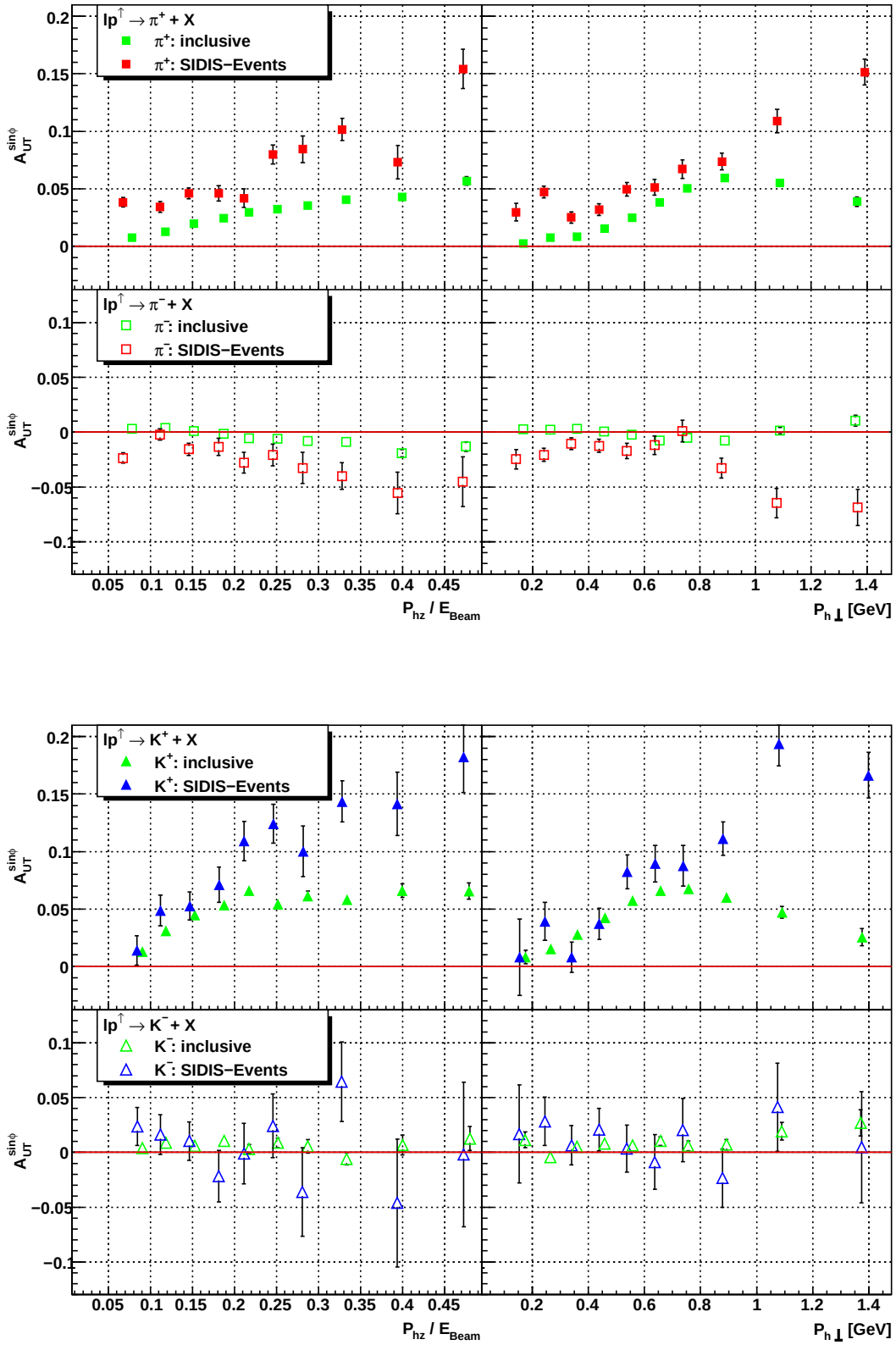


**Figure 5.4:** The analysing power $A_{UT}$ for charged pions (top-panel) and kaons (bottom-panel). Only hadrons from SIDIS-events are selected. The resulting asymmetry (red points for charged pions and blue points for charged kaons) are compared to the asymmetry of the purely inclusive measurement (green points).

### 5.3.2 The Photoproduction-Region

This discussion refers to the results shown in Figure 5.5. For the data selection the following criterium was used. In order to select only these events from a small $Q^2$ scattering event, one has to anti-tag leptons. As $Q^2 \propto \sin^2(\theta/2)$, we are interested in small scattering angles $\theta$. Since the lower bound of the acceptance in the polar angle of the HERMES spectrometer is 40 mrad, leptons from low-$Q^2$ events simply vanish in the acceptance gap (cf. Figure 4.1) and cannot be detected anymore. These events contribute most to the overall statistics, though. A "veto" on leptons can be regarded as a complementary approach of the SIDIS-tagging in the previous Subsection.
The changes of the asymmetries reached by the anti-tagging of leptons, are almost negligible compared to the inclusive measurements. For positive charged pions the $P_{h\perp}$-dependent analysing power peaks in the region between 0.8 GeV and 1.0 GeV. The rise of the asymmetry in the soft $P_{h\perp}$-region is the same as in the purely inclusive case. The drop of the asymmetry in the hard $P_{h\perp}$-region is steeper and seems to reach zero at lower values of $P_{h\perp}$. This confirms our assumption that the positve asymmetries in the hard $P_{h\perp}$-region are caused by leading-twist effects, namely the contribution of the Sivers DF $f_{1T}^{\perp q}$. For the analysing power $A_{UT}$ of negative pions, no new features can be observed.
For positive charged kaons the $P_{h\perp}$-dependent asymmetry peaks in the region between 0.6 GeV and 0.8 GeV. Also here – compared to the purely inclusive measurement – the drop of the asymmetry in the hard $P_{h\perp}$-region is steeper and seems to reach zero at lower values of $P_{h\perp}$.
By the selection of charged hadrons from the photoproduction regime we can confirm the assumption from the previous Subsection (where we tagged SIDIS events): the main contribution to the positive analysing power $A_{UT}$ originates from leading twist effects of the Sivers DF $f_{1T}^{\perp q}$. Sub-leading twist effects suppress the contributions from the SIDIS-regime in the hard $P_{h\perp}$-region. The Sivers DF can be regarded as a leading-twist dominated DF.

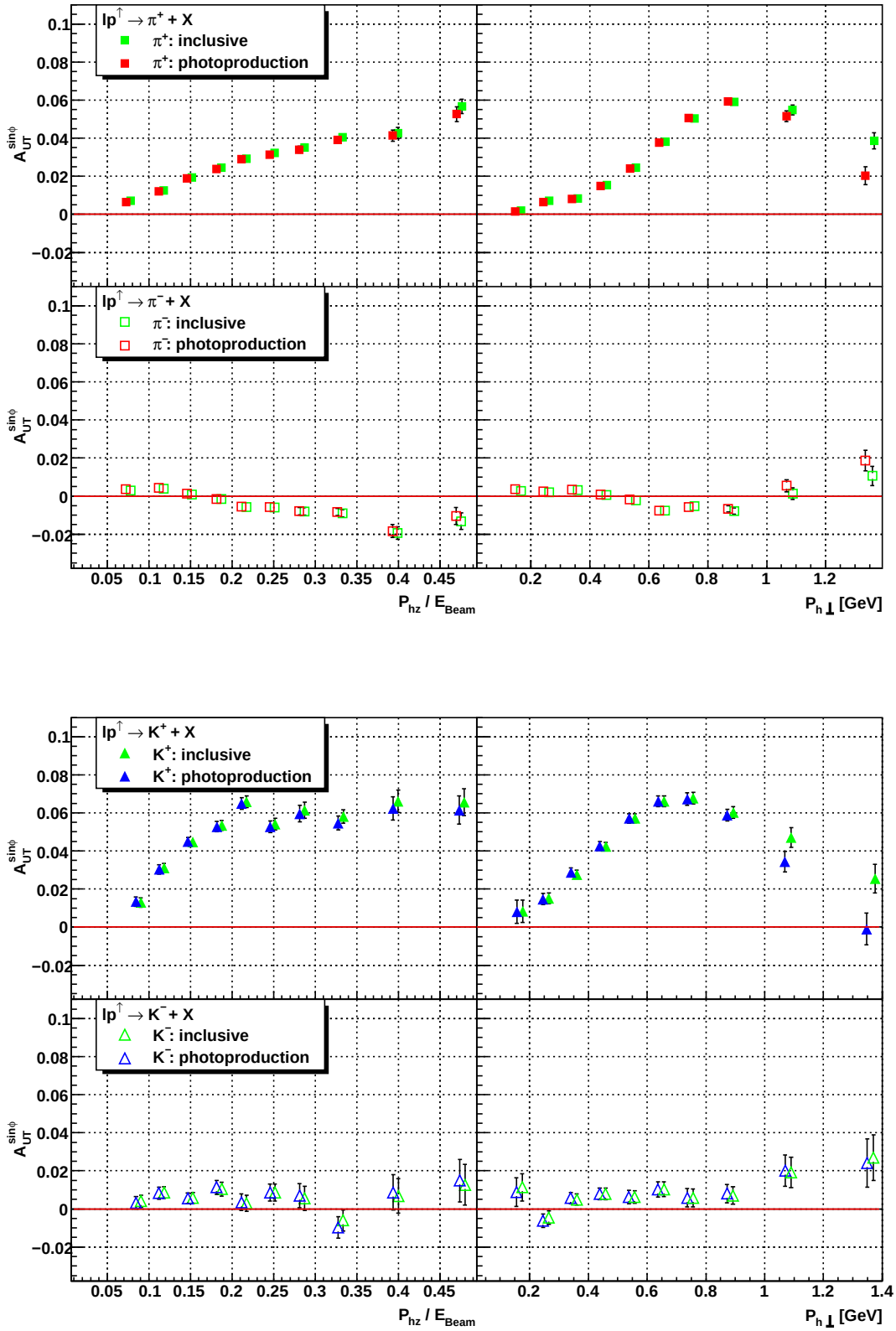


**Figure 5.5:** The analysing power $A_{UT}$ for charged pions (top-panel) and kaons (bottom-panel). Only hadrons arising from photoproduction processes (i.e. $Q^2 \sim 0$) are selected. The resulting asymmetry (red points for charged pions and blue points for charged kaons) are compared to the asymmetry of the purely inclusive measurement (green points).

# Part II

# The Spin Structure of the $\Lambda^0$ Baryon on the Lattice

# Chapter 6

# Motivation

The $\Lambda^0$ hyperon is an especially interesting particle in spin physics. It is the lightest strange baryon ($M_\Lambda = 1115.684\,\text{MeV}$) and thus can only decay weakly ($\tau = 2.632 \times 10^{-10} s$), the dominant decay channels being $\Lambda \to p\pi^-$ (63.9%) and $\Lambda \to p\pi^0$ (35.8%). We will focus on the charged decay channel, since e.g. in the HERMES experiment $\Lambda$ particles can only be detected via this channel. As the weak decay is parity violating, the proton is being emitted preferentially into the direction of the $\Lambda^0$ spin. The angular distribution of the decay nucleon in the $\Lambda^0$ rest frame has the form

$$\frac{dN}{d\Omega_P} \propto 1 + \alpha \vec{P}^\Lambda \cdot \widehat{k}^P. \tag{6.0.1}$$

Here, $\widehat{k}^P$ is the unit vector along the proton momentum in the $\Lambda^0$ rest frame, $\vec{P}^\Lambda$ is the polarisation of the $\Lambda^0$ and $\alpha = 0.642 \pm 0.013$ [A$^+$08] is the asymmetry parameter of the weak decay. Information about the $\Lambda^0$ polarisation can therefore be directly obtained from the angular distribution of the decay particles.

With the advent of deep inelastic spin physics many authors have examined the potential role of $\Lambda^0$'s as a probe of nucleon spin substructure [JJ91]. Since polarised strange quarks are relatively rare in the nucleon and their squared charge is only $1/9$, the prospect for using $\Lambda^0$'s to probe polarised strange quarks in the nucleon is not too good. On the other hand, polarised up quarks are abundant in the nucleon and their squared charge is $4/9$. It is easy to see that even a small correlation between the spins of the up quarks and the $\Lambda^0$'s into which they fragment would make them dominant over strange quarks and potentially useful as probes of the polarised up quark distributions in the nucleon.

In the naive QPM all the spin of the $\Lambda^0$ is carried by the strange quark ($\Delta s^\Lambda = 1$), the up and down quark forming a spin singlet, meaning that $\Delta u^\Lambda = 0$ and $\Delta d^\Lambda = 0$. On the other hand the $\Lambda^0$ is a member of the hyperon octet and based on $SU(3)$ flavor symmetry all the quark contributions to the spin of the $\Lambda^0$ are related to those of all other members in the octet including the proton and the neutron. The nucleon data tell us that only a small fraction of the nucleon spin originates from the spins of its quarks, $\Delta\Sigma \approx 0.2$, in contrast to the naive QPM prediction, $\Delta\Sigma = 1$. As a consequence, also the up and down quarks should be expected to give sizeable contributions to the spin of the $\Lambda^0$ hyperon [BJ93]. The assumption $\Delta\Sigma^P \approx 0.18$, together with the values for the weak decay constants $F$ and $D$ and the weak axial charge $g_a = g_A/g_V$ resulted in the estimate: $\Delta u^\Lambda = -0.2$, $\Delta d^\Lambda = -0.2$ and $\Delta s^\Lambda = 0.58$ (from Reference [BJ93]). Lattice-QCD calculations of the spin structure of the $\Lambda^0$ hyperon [G$^+$02], however, predict very small values of $\Delta u^\Lambda$ and $\Delta u^\Lambda$ compatible with zero, whereas $\Delta s^\Lambda \approx 0.68$.

Thus, there is ample motivation to perform further lattice calculations which provide information on the spin-structure of the $\Lambda^0$. As the previous lattice calculations were performed in the quenched limit of lattice QCD (that means that quark loops are neglected and only valence quarks contribute to physical observables), it would be very stimulating to update the existing lattice results with dynamical fermions. This dynamical simulation is the subject of the subsequent Chapters. First we will give a compact insight in lattice-QCD. Then we will describe how to caluclate the relevant observables, namely the matrix elements of choice, for the $\Lambda$ spin structure. Finally, we will give a status report on the persisting calculations of the two- and three-point functions.

# Chapter 7

# Lattice Quantum Chromo-Dynamics

In the course of this chapter, we introduce the formulations of lattice QCD which we use. This consists mainly in giving the defnitions of the various actions for the gluons and the quarks. Most of it can be found in textbooks and reviews, e.g. [Gup98, PS95]. The continuum action for these fields will be the starting point. Afterwards, the basic notation for the lattice on which the theory is discretised is subject of Section . The standard lattice gauge actions are introduced in Section 7.4. The various discretisations rely on the fact that only the continuum limit of the theory is fxed. At finite lattice spacing, there is a certain arbitrariness which can be utilised to improve the properties of the theory. In Section we will be describing the discretisations of the fermion part of the QCD action. It has long been believed that it is impossible to construct a theory with chiral symmetry and the correct continuum limit on a lattice. The main problem has always been the appearance of so-called doublers. These are degenerate and unwanted particles which do not vanish in the continuum limit. The first cure to this problem has been given by Wilson. He suggested an action which gives the doublers a mass which grows in the continuum limit; hence they decouple. Unfortunately, this action breaks chiral symmetry explicitly.

## 7.1 Continuum Quantum Chromodynamics

Quantum Chromodynamics is the theory of quarks and their interaction by the exchange of gluons. One of its most fundamental properties is local gauge invariance under color-$SU(3)$. Our starting point is the plain fermionic Lagrangian:

$$\mathcal{L}_f = \sum_{f=1}^{6} \bar{\Psi}_f(x)(i\gamma^\mu - m_f)\Psi_f(x) \tag{7.1.1}$$

containing free quarks only, one can construct the full QCD Lagrangian by demanding this symmetry. It originates from the fact that physics must not depend on man-made coordinate systems, here for the color degrees of freedom. In general local gauge invariance means that the Lagrangian shall be invariant under a gauge transformation $g(x)$:

$$\Psi(x) \to \Psi'(x) = g(x)\Psi(x) = e^{-i\Theta_a(x)T_a}\Psi(x), \tag{7.1.2}$$

where $T_a$ are the generators of the gauge group. This invariance can only be true if we replace the standard derivative $\partial$ by a covariant derivative $D$:

$$D_\mu \to \partial_\mu + iA_\mu(x). \tag{7.1.3}$$

The transformation properties of the additional term

$$A_\mu(x) \to A'_\mu(x) = g(x)\left(A_\mu(x) - i\partial_\mu\right)g^{-1}(x) \tag{7.1.4}$$

are built in a way to render $D$ covariant

$$D_\mu \to D'_\mu = g(x)D_\mu g^{-1}(x) \tag{7.1.5}$$

and thus the whole Lagrangian invariant. However, postulating a new symmetry does not come for free. We have introduced a new vector field $A_\mu(x)$. Up to now the Lagrangian does not involve any derivatives of $A_\mu(x)$. Deriving the classical equations of motion using Euler-Lagrange

$$\partial_\mu\left(\frac{\partial\mathcal{L}}{\partial(\partial_\mu\Psi)}\right) = \frac{\partial\mathcal{L}}{\partial\Psi}, \qquad \partial_\mu\left(\frac{\partial\mathcal{L}}{\partial(\partial_\mu A^\nu)}\right) = \frac{\partial\mathcal{L}}{\partial A^\nu} \tag{7.1.6}$$

would lead to a theory with infinitely many parameters $A_\mu(x)$. Therefore we need to promote $A^\mu(x)$ to physical degrees of freedom by adding a kinetic term to the Lagrangian. It will have to be invariant under gauge transformations $g(x)$. For that reason we exploit the covariance of $D$ to build a new vovariant Field $F^{\mu\nu}$:

$$F^{\mu\nu} = -i[D^\mu, D^\nu]. \tag{7.1.7}$$

The simplest nonzero invariant scalar using the constructed field is $\mathrm{Tr}\, F^{\mu\nu}F_{\mu\nu}$ such that the total Yang-Mills Lagrangian with some gauge coupling parameter $g$ (not the gauge transformation $g(x)$!) looks like

$$\mathcal{L}_f = \sum_{f=1}^{6} \bar{\Psi}_f(x)(i\not{D} - m_f)\Psi_f(x) - \frac{1}{2g^2}\,\mathrm{Tr}\, F^{\mu\nu}F_{\mu\nu}. \tag{7.1.8}$$

Finally the action is defined as

$$\mathcal{S}[\bar{\Psi}, \Psi, A] = \int d^4x \mathcal{L}[\bar{\Psi}, \Psi, A](x). \tag{7.1.9}$$

There are at least two ways to obtain a quantum theory from the above action. One possibility is canonical quantisation which imposes suitable commutation relations. A short introduction to this can be found in reference [PS95]. The most powerful formalism is quantisation by functional methods using the Feynman path integral. In this formalism the expectation value of any operator $\mathcal{O}[\bar{\Psi}, \Psi, A]$ can be obtained via

$$\langle \mathcal{O}[\bar{\Psi}, \Psi, A] \rangle = \frac{\int \mathcal{D}\bar{\Psi}\mathcal{D}\Psi\mathcal{D}A\, \mathcal{O}[\bar{\Psi}, \Psi, A] \exp\{i\mathcal{S}[\bar{\Psi}, \Psi, A]\}}{\int \mathcal{D}\bar{\Psi}\mathcal{D}\Psi\mathcal{D}A \exp\{i\mathcal{S}[\bar{\Psi}, \Psi, A]\}} \tag{7.1.10}$$

Here the integration measures are formally defined as a product over all possible degrees of freedom: For fermions this is the color $c$, the flavor $f$ and the spinor index $\alpha$ for every single space-time point $x \in \mathbb{R}^4$, while for vector bosons we have the directions $\mu$ for every generator $T_a$ and every single space-time point $x \in \mathbb{R}^4$:

$$\begin{aligned} \mathcal{D}\Psi &= \prod_{f,c,\alpha} \prod_{x\in\mathbb{R}^4} d\Psi_f^{\alpha,c}(x), \\ \mathcal{D}\bar{\Psi} &= \prod_{f,c,\alpha} \prod_{x\in\mathbb{R}^4} d\bar{\Psi}_f^{\alpha,c}(x), \\ \mathcal{D}A &= \prod_{a,\mu} \prod_{x\in\mathbb{R}^4} dA_\mu^a(x). \end{aligned} \tag{7.1.11}$$

Beyond gauge invariance there are a number of other symmetries of our action. The Dirac operator

$$D(m) = i\not{D} - m \tag{7.1.12}$$

has a very peculiar property in the massless limit. It obeys

$$D(0)\gamma_5 + \gamma_5 D(0) = 0, \tag{7.1.13}$$

meaing the massless action is invariant under chiral transformations

$$\begin{aligned} \Psi(x) &\to \Psi'(x) = e^{i\varepsilon\gamma_5}\Psi(x), \\ \bar{\Psi}(x) &\to \bar{\Psi}'(x) = \bar{\Psi}(x)e^{i\varepsilon\gamma_5}. \end{aligned} \tag{7.1.14}$$

This symmetry and its spontaneous breaking are a central property of low-energy QCD.

## 7.2 Discretisation I: The Lattice

The basic idea of lattice QCD is to actually evaluate the Feynman path integral (7.1.10) in a computer. We want to do this by Monte Carlo methods. Unfortunately the Boltzmann weight factors $e^{iS}$ in that path integral may be oscillating rapidly, prohibiting the use of statistical sampling. We need to write these factors in a form $e^{-S'}$, where $S'$ is real and bounded from below. We can do this by switching from Minkowskian spacetime to Euclidean spacetime: To this end we let $x^0$ become purely imaginary:

$$x^0 = -ix^4 \tag{7.2.1}$$

This implies $\partial_0 = i\,\partial_4$. With this formal substitution the plain fermionic action becomes:

$$\begin{aligned} i\,\mathcal{S}_f =& i\int d^4x\,\bar{\Psi}_f(x)(i\gamma^\mu - m_f)\Psi_f(x) \\ =& -\int_E d^4x_E\,\bar{\Psi}_f(x)(i\gamma^E_\mu + m_f)\Psi_f(x) \\ =& -\mathcal{S}^E_f \end{aligned} \tag{7.2.2}$$

From now on we work in Euclidean spacetime and drop the $E$ labels. Still, performing infinitely many integrals in a computer as prescribed in formula (7.1.11) is not possible. In order to renormalise our theory we need a regulator anyway, so we replace the continuous 4-dimensional spacetime with a hypercubic lattice

$$x = a(n_1, n_2, n_3, n_4) \quad \text{with} \quad n_\mu \in 0, 1, \ldots, N_\mu - 1, \tag{7.2.3}$$

where the regulator $a$ is the lattice spacing and $N_\mu$ si the number of lattice sites. It is essentially a UV-cutoff which limits momenta to the first Brillouin zone $|p_\mu| < \pi/4$. On the boundaries we continue the lattice periodically in all four dimensions such that we obtain a 4-Torus.

## 7.3 Discretisation II: Fermions on the Lattice

The fermions, being Grassmann degrees of freedom, have to obey antiperiodic boundary conditions in time direction. We need this to be able to use the transfer matrix formalism which we introduce in Section 7.7. For the spatial boundary conditions we choose periodic ones, i.e.

$$\begin{aligned} \Psi(x_1 + aN_1, x_2, x_3, x_4) &= +\Psi(x_1, x_2, x_3, x_4), \\ \Psi(x_1, x_2, x_3, x_4 + aN_1) &= -\Psi(x_1, x_2, x_3, x_4), \end{aligned} \tag{7.3.1}$$

Now, our integration measures for the fermions looks like

$$\begin{aligned} [d\Psi &= \prod_{f,c,\alpha}\prod_n d\Psi^{\alpha,c}_f(an), \\ [d\bar{\Psi}] &= \prod_{f,c,\alpha}\prod_n d\bar{\Psi}^{\alpha,c}_f(an). \end{aligned} \tag{7.3.2}$$

Derivates and integrations turn into (which is just an example since there exist several possibilities)

$$\int d^4x \to a^4 \sum_n, \tag{7.3.3}$$

$$\partial_\mu \Psi(x) \to \frac{\Psi(x + a\hat{\mu}) - \Psi(x - a\hat{\mu})}{2a}. \tag{7.3.4}$$

Next we factor all dimensions, such that all variables turn dimensionless, i.e.

$$m \to a^{-1} m, \tag{7.3.5}$$

$$\Psi(x) \to a^{3/2}\Psi(n), \tag{7.3.6}$$

$$\partial_\mu \Psi(x)(x) \to \frac{a^{-3/2}}{2a}(\Psi(n + a\hat{\mu}) - \Psi(n - a\hat{\mu})). \tag{7.3.7}$$

### 7.3.1 The Naïve Discretisation

Now we can write down the fermionic lattice action:

$$\begin{aligned} \mathcal{S} =& \frac{1}{2}\sum_n \bar{\Psi}(n)\gamma_\mu(\Psi(n + a\hat{\mu}) - \Psi(n - a\hat{\mu})) + m\sum_n \bar{\Psi}(n)\Psi(n) \\ =& \sum_{n,m} \bar{\Psi}(n)K(n,m)\Psi(m) \end{aligned} \tag{7.3.8}$$

We implicitly defined the naive lattice Dirac operator $D^{\text{naïve}} = K$:

$$D^{\text{naïve}}(n,m) = \sum_\mu \frac{1}{2}\gamma_\mu(\delta_{n+\mu,m} - \delta_{n-\mu,m}) + \mathbb{1}m\delta_{n,m}. \tag{7.3.9}$$

There is, however, a problem with this Dirac operator. It is called the fermion doubling problem. The problem becomes apparent when we calculate the propagator of this naïve Dirac operator in momentum space. To this end we Fourier transform the operator by

$$\begin{aligned}\widetilde{K}(k,l) =& \sum_{n,m} e^{-ikn} K(n,m) e^{+ilm} \\ =& \sum_{n,m} e^{-i(k-l)n} \left( \frac{1}{2} \sum_{\mu} \gamma_\mu (e^{il_\mu} - e^{-il_\mu}) + \mathbb{1}, \right) \\ =& N \delta_{kl} \widetilde{K}(l)\end{aligned} \tag{7.3.10}$$

where $N$ is the total number of lattice sites and

$$\widetilde{K}(l) = \mathbb{1}m + i \sum_{\mu} \gamma_\mu \sin(l_\mu) \tag{7.3.11}$$

being the Fourier transformed Dirac operator. Its inversion yields the quark propagator

$$\widetilde{K}^{-1}(l) = \frac{\mathbb{1}m - i \sum_\mu \gamma_\mu \sin(l_\mu)}{m^2 + \sum_\mu}. \tag{7.3.12}$$

This object does have the right continuum limit near $l = 0$:

$$\lim_{a\to 0} a\widetilde{K}^{-1}(l \approx 0) = \lim_{a\to 0} a \frac{\mathbb{1}am_{\text{phys}} - i \sum_\mu \sin(l_\mu)}{a^2 m_{\text{phys}}^2 + \sum_\mu \sin^2(q_\mu a)} = \frac{\mathbb{1}m_{\text{phys}} - i\not{q}}{m_{\text{phys}}^2 + q^2} = S(q). \tag{7.3.13}$$

with a pole i Minkowski space at $q^2 = m_{\text{phys}}^2$, corresponding to a particle with mass $m_{\text{phys}}$. But within the first Brillouin zone the full continuum limit consists of 15 more poles at $q_i$, where

$$\begin{aligned} q_i \in \Big\{ & \left(\frac{\pi}{a},0,0,0\right), \left(0,\frac{\pi}{a},0,0\right), \ldots, \\ & \left(\frac{\pi}{a},\frac{\pi}{a},0,0\right), \ldots, \\ & \left(\frac{\pi}{a},\frac{\pi}{a},0,0\right), \ldots, \\ & \left(\frac{\pi}{a},\frac{\pi}{a},\frac{\pi}{a},0\right) \Big\}. \end{aligned} \tag{7.3.14}$$

These additional poles can be interpretated as additional (unphysical) fermions and are thus calls fermion doublers. They are unwanted lattice artifacts and have to be removed in order to obtain proper physics from lattice QCD.

### 7.3.2 Wilson Fermions

The idea of Wilson fermions [Wil74] is to give the doublers a mass which grows in the continuum limit, e.g., $m \propto 1/a$. This is done by adding a term to the naïve action Equation (7.3.1):

$$\mathcal{S}_{\text{Wilson}} = a^4 \sum_n \left[ (m + \frac{4r}{a}) \bar{\Psi}(n) \Psi(n) - \frac{1}{2a} \sum_\mu \bar{\Psi}(n+\hat{\mu})[r+\gamma_\mu]\Psi(n) \right]. \tag{7.3.15}$$

The parameter $r$ can take any value $0 < r < -1$. For $r = 0$ the naïve action Equation (7.3.1) is recovered. In practical simulation one frequently – as we did – takes $r = 1$. If we now change the normalisation of the fermion fields

$$\sqrt{a^3(am+4r)}\Psi \to \Psi \quad \text{and} \quad \sqrt{a^3(am+4r)}\bar{\Psi} \to \bar{\Psi} \tag{7.3.16}$$

we can bring this action into the standard form

$$\mathcal{S}_{\text{Wilson}} = \sum_n \left[ \bar{\Psi}(n)\Psi(n) - \kappa \sum_\mu \bar{\Psi}(n+\hat{\mu})[r+\gamma_\mu]\Psi(n) \right]. \tag{7.3.17}$$

Here we introduced the hopping parameter $\kappa$ which now encodes the bare mass of the fermion

$$\kappa = \frac{1}{2am + 8r}. \tag{7.3.18}$$

In the free theory the chiral limit $am_q \to 0$ is performed by

$$\frac{1}{\kappa} \to 8r \equiv \frac{1}{\kappa_c^{\text{free}}}. \tag{7.3.19}$$

In a realistic simulation with interacting fermions it has to be determined experimentally which quark mass a given value of $\kappa$ corresponds to. The value of $\kappa$ which gives a zero quark mass is called the critical hopping parameter $\kappa_c$. It is not possible to determine it unambiguously. The standard procedure is to look at observables which vanish in the chiral limit as the pion mass or the PCAC quark mass. The perturbative expression [GHI+96]

$$am_q = 0.56(\frac{1}{\kappa} - \frac{1}{\kappa_c}). \tag{7.3.20}$$

relates $\kappa$ and the quark mass. This relation depends crucially depends on the gauge coupling $\beta = \frac{6}{g_0^2}$
On the lattice, however, the Fourier transformed Wilson Dirac operator looks like

$$\widetilde{D}_{\text{Wilson}}(l) = \mathbb{1}m + i\sum_\mu \gamma_\mu \sin(l_\mu) + \mathbb{1}\sum_\mu (1-\cos(l_\mu)). \tag{7.3.21}$$

There is, however, one crucial problem with the Wilson action. It does explicitly break chiral symmetry even at vanishing quark mass, as

$$\left\{D^{-1}_{\text{Wilson}}, \gamma_5\right\} \neq 0 \quad \text{for} \quad m = 0. \tag{7.3.22}$$

This breaking of chiral symmetry of $\mathcal{O}(a)$ leads to a number of other difficulties: Fluctuations in the eigenvalues of the Dirac operator induced by this breaking increase the computational effort in obtaining propagators for low quark masses. Additionally exceptional configurations show up which lead to difficulties in dynamical simulations. So in practical calculations one is restricted to rather large quark masses. Even more problematic is the fact that recovering chiral symmetry in the continuum limit can only be achieved by a fine tuning of the quark mass due to additive mass renormalisation.

### 7.3.3 Clover-Wilson Fermions

In order to reduce discretisation effects of the fermionic action, Sheikholeslami and Wohlert [SW85] proposed to add a special term to the Wilson action:

$$\mathcal{S}_{\text{Wilson}} \to \mathcal{S}_{\text{Wilson}} + c_{\text{SW}} \frac{i}{4} a\bar{\Psi}(x)\sigma_{\mu\nu}F_{\mu\nu}\Psi(x). \tag{7.3.23}$$

This goes under the name clover improvement as the common discretisation of $F_{\mu\nu}$ has the form of a clover leaf. It includes the plaquettes that are attached to $x$ in the $\mu-\nu$-plane. The coefficient $c_{\text{SW}}$ of the clover term has to be determined nonperturbatively. This has been done by [SW85, EHK98] for a couple of lattice spacings. They provide an interpolation formula that enables the prediction of $c_{\text{SW}}$ at a large range of $\beta$ values. Of course, there exist plenty of more types of fermion lattice action, like e.g. Staggered Fermions [KS87] or Chirally improved fermions (Ginsparg-Wilson fermions) [GW82]. For our simulation, we chose Clover-Wilson Fermions, though.

## 7.4 Discretisation III: Gluons on the Lattice

In Section 1 we have derived the gauge field and its interaction with fermions by postulating local gauge invariance. Now we repeat that procedure for the lattice. To this end we need to render the fermionic action

$$\mathcal{S} = \sum_{n,m} \bar{\Psi}(n) D(n,m) \Psi(m) \tag{7.4.1}$$

invariant under the gauge transformations

$$\begin{aligned} \Psi(n) &\to \to \Psi'(n) = g(n)\Psi(n), \\ \bar{\Psi}(n) &\to \bar{\Psi}(n) = g^{-1}(n)\Psi(n). \end{aligned} \tag{7.4.2}$$

Therefore the Dirac operator must transform as

$$D(n,m) \to D'(n,m) = g(n)D(n,m)g^{-1}(m). \tag{7.4.3}$$

If we remember e.g. the naive Dirac operator

$$D^{\text{naïve}}(n,m) = \sum_{\mu} \frac{1}{2}\gamma_{\mu}(\delta_{n+\mu,m} - \delta_{n-\mu,m}) + \mathbb{1}m\delta_{n,m}. \tag{7.4.4}$$

we see that we need to modify the discretised derivative and turn it into a covariant one. We need to modify each $\delta_{n,m}$ to a $\delta_{n,m}U(n,m)$, where $U(n,m)$ transforms just the way we need, namely

$$U(n,m) \to U'(n,m) = g(n)U(n,m)g^{-1}(m). \tag{7.4.5}$$

In the continuum this factor is well known as the Schwinger line integral

$$U(x,y) = \mathcal{P}\left\{\exp\left(i\int_x^y dz_{\mu}A^{\mu}(z)\right)\right\}. \tag{7.4.6}$$

Discretising it on the lattice by

$$\begin{aligned} U_{\mu}(n) &= U(n,n+\widehat{\mu}) = U(x,x+a\widehat{\mu}) \approx \exp iaA_{\mu}(n), \\ U_{-\mu}(n) &= U(n,n-\widehat{\mu}) = U(x,x-a\widehat{\mu})^{\dagger} \approx U_{\mu}(n+\widehat{\mu}), \end{aligned} \tag{7.4.7}$$

we see that the $U$ field does not live on the sites of the lattice like the fermions but rather links from one site to the next, by transporting the gauge. In lattice language these object are therefore called link variables. The Schwinger line integral becomes a product of links along a path $\mu_1,\mu_2,\ldots\mu_k$ connecting $n$ and $m$:

$$U(n,m) = U_{\mu_1}(n)U_{\mu_2}(n+\widehat{\mu}_1)\ldots U_{\mu_k}(n+\widehat{\mu}_k). \tag{7.4.8}$$

Using these gauge transporters to construct gauge invariant quark bilinears $\bar{\Psi}(n)U(n,m)\Psi(m)$ we can write down the covariant version of the naive Dirac operator

$$D^{\text{naïve}}(n,m) = \sum_{\mu} \frac{1}{2}\gamma_{\mu}(U_{\mu}(n)\delta_{n+\mu,m} - U_{-\mu}(n)\delta_{n-\mu,m}) + \mathbb{1}m\delta_{n,m}, \tag{7.4.9}$$

or the covariant version of the Wilson Dirac operator:

$$D_{\text{Wilson}}(n,m) = \mathbb{1}m\delta_{n,m} + \sum_{\mu}\frac{1}{2}\gamma_{\mu}(U_{\mu}(n)\delta_{n+\mu,m} - U_{-\mu}(n)\delta_{n-\mu,m}) - \mathbb{1}\sum_{\mu}\frac{1}{2}(U_{\mu}(n)\delta_{n+\mu,m} - 2\,\delta_{n,m} + U_{-\mu}(n)\delta_{n-\mu,m}). \tag{7.4.10}$$

We see that the Dirac operator depends only on the gauge fields and is completely decoupled from the fermion fields.

### 7.4.1 The Naïve Discretisation

As in the continuum we had to introduce new degrees of freedom to obtain an action that is invariant under local gauge transformations. We need to give them a kinetic term. As in the continuum we use the most simple nonzero gauge invariant object we can construct. The gauge transporters transform as

$$U(n,m) \to U'(n,m) = g(n)U(n,m)g^{-1}(m), \tag{7.4.11}$$

so we can take any closed path to build such an invariant object by

$$\text{Tr}\,U(n,n) \to \text{Tr}U'(n,n) = \text{Tr}\left(g(n)U(n,n)g^{-1}(n)\right) = \text{Tr}U(n,n) \tag{7.4.12}$$

The most simple paths we can take on the lattice are the plaquettes, squares with edge length $a$ along links $\mu$ and $\nu$ starting at $n$. So we define:

$$U_{\mu\nu}(n) = U_{\mu}(n)U_{\nu}(n+\widehat{\mu})U_{-\mu}(n\widehat{\mu}+\widehat{\nu})U_{-\nu}(n\widehat{\mu}). \tag{7.4.13}$$

From this quantity Wilson constructed the Wilson gauge action [Wil74], for $SU(N)$ defined as

$$\mathcal{S}_{\text{Wilson,G}} = \beta\sum_{n}\sum_{\mu<\nu}\left(1 - \frac{1}{N}\text{Re}\,\text{Tr}\,U_{\mu\nu}(n)\right), \tag{7.4.14}$$

where the connection between $\beta$ and the bare coupling is

$$\beta = \frac{2N}{g^2} \tag{7.4.15}$$

Indeed it can be shown by expanding Equation (7.4.14) to order $\mathcal{O}(a^2)$ that Wilson's gauge action is a discretised version of the continuum gauge action:

$$\mathcal{S}_{\mathrm{W,G}} = -\frac{1}{2g^2}\int d^4x \,\mathrm{Tr}\, F_{\mu\nu}(x)F_{\mu\nu}(x) + \mathcal{O}(a^2). \tag{7.4.16}$$

To reduce these discretisation effects, Lüscher and Weisz [LW85] constructed a gauge action that for on shell quantities has $\mathcal{O}(a^2)$ errors only. As we will not generate gauge configurations in our simulation, but will use existing ones, namely dynamical gauge configuration, we end up here.

## 7.5 Expectation Values on the Lattice

Now that we know which action

$$\mathcal{S}[\bar{\Psi},\Psi,U] = \mathcal{S}_{\mathrm{Fermion}}[\bar{\Psi},\Psi,U] + \mathcal{U}_{\mathrm{Gauge}}[U] \tag{7.5.1}$$

to use we are almost ready to perform a lattice QCD simulation by calculating some path integral expectation value

$$\langle \mathcal{O}[\bar{\Psi},\Psi,U]\rangle = \frac{\int [d\bar{\Psi}][d\Psi][dU]\,\mathcal{O}[\bar{\Psi},\Psi,U]\,e^{-[\bar{\Psi},\Psi,U]}}{\int [d\bar{\Psi}][d\Psi][dU]\,e^{-\mathcal{S}[\bar{\Psi},\Psi,U]}}. \tag{7.5.2}$$

We have to integrate over all possible gauge and fermion fields:

$$\begin{aligned}
\mathcal{D}\Psi &= \prod_{f,c,\alpha}\prod_n d\Psi_f^{\alpha,c}(x),\\
\mathcal{D}\bar{\Psi} &= \prod_{f,c,\alpha}\prod_n d\bar{\Psi}_f^{\alpha,c}(x),\\
\mathcal{D}U &= \prod_\mu \prod_n dU_\mu(n).
\end{aligned} \tag{7.5.3}$$

As already mentioned above, a full evaluation of this integral is too expensive, so one hast to use Monte Carlo methods. The gauge fields can be sampled relatively easily. The fermion fields are a little more difficult to treat as they are Grassmann variables: We integrate out the fermion fields analytically:

$$\begin{aligned}
\langle \mathcal{O}[\bar{\Psi},\Psi,U]\rangle =& \frac{\int [dU]\,e^{-\mathcal{S}_{\mathrm{Gauge}}[U]}\left(\int [d\bar{\Psi}][d\Psi]\,\mathcal{O}[\bar{\Psi},\Psi,U]\,e^{\sum_f \bar{\Psi}_f D_f[U]\Psi_f}\right)}{\int [dU]\,e^{-\mathcal{S}_{\mathrm{Gauge}}[U]}\left(\int [d\bar{\Psi}][d\Psi]\,e^{-\sum_f \bar{\Psi}_f D_f[U]\Psi_f}\right)}\\
=& \frac{\int [dU]\,e^{-\mathcal{S}_{\mathrm{Gauge}}[U]}\left(\mathcal{O}[D_f^{-1}[U],U]\prod_f \mathrm{det}D_f[U]\right)}{\int [dU]\,e^{-\mathcal{S}_{\mathrm{Gauge}}[U]}\left(\prod_f \mathrm{det}D_f[U]\right)}\\
=& \langle \mathcal{O}[D_f^{-1}[U],U]\rangle
\end{aligned} \tag{7.5.4}$$

In the literature, this integration of the fermion fields is often referred to as fermion contraction. The operator $\mathcal{O}$ is now a functional of gauge fields only. This forces us to evaluate propagators $D_f^{-1}[U]$ on each configuration. A tremendous simplification of the numerical effort is obtained by using the quenched approximation

$$\mathrm{det}D_f[U] = \mathrm{const.} \tag{7.5.5}$$

Setting the fermion determinant constant essentially means to neglect quark loops. The gauge configurations we use for our simulation were generated dynamically. This means that quark loops (i.e. vacuum polarisations) were taken into account.

## 7.6 Propagators

One big difficulty in obtaining results from lattice calculations is that simulations at small quark masses are expensive in computer time. In the process of a Monte Carlo simulation one computes observables using the generated configurations. To include fermions one has to invert the Dirac operator $D[U]$ on each of these configurations to obtain the quark propagators $D^{-1}[U]$. The Dirac operator is a huge matrix with edge length $V \cdot N_c \cdot N_d \approx 10^6$. A full inversion of such a matrix is prohibitively expensive. Fortunately, in most lattice simulations one can use properties like $\gamma_5$-hermiticity such that only few columns of the full propagator are necessary. This works well for calculations where only connected diagrams appear but fails when disconnected diagrams show up. In this case one is forced to estimate the full propagator using stochastic methods. Nevertheless the computation of a single column of the full matrix $M = D[U] + m$ or equivalently the solution $v$ for some source $b$ by

$$M v = b \tag{7.6.1}$$

is still not cheap. In most cases the solution is computed iteratively by conjugate gradient methods [GBK96] which analytically converge in $n = V N_c N_d$ steps.

## 7.7 Extraction of Masses

The most elementary results one can get from a lattice simulation are masses of composite particles. This is done using correlators or two-point functions. The transfer matrix formalism, which is nothing but an application of the Euclideanised version of the time-evolution operator $e^{-iHt}$, predicts for the two-point functions:

$$\langle B(t_1)\bar{B}(t_1)\rangle = \frac{1}{Z}\mathrm{Tr}\left(S^{N_t-t_2/a} B S^{(t_2-t_1)/a} \bar{B} S^{t_1/a}\right), \tag{7.7.1}$$

where $Z = \mathrm{Tr}\, S^{N_t}$ and $Nt = L_t/a$ is the number of sites in time direction. We use $N_S = L_S/a$ for the number of sites a spatial direction. In the continuum one usually works with the standard normalisation convention

$$\langle N(\vec{p})|\bar{N}(\vec{p}')\rangle = 2E_{\vec{p}}(2\pi)^3\delta^{(3)}(\vec{p}-\vec{p}'). \tag{7.7.2}$$

On the lattice, however, it is much easier to normalise all states to 1. Using this lattice normalisation we insert identities $\mathbb{1} = \sum_\nu |\nu\rangle\langle\nu|$ given by the ordered set of energy eigenstates $|\nu\rangle$ of $S$ with energies $E_\nu$:

$$\begin{aligned}\langle B(t_1)\bar{B}(t_1)\rangle =& \frac{1}{Z}\sum_{\nu_1\ldots\nu_5}\langle\nu_5|S^{N_t-t_2/a}|\nu_1\rangle\langle\nu_1|B|\nu_2\rangle\langle\nu_2|S^{(t_2-t_1)/a}|\nu_3\rangle\langle\nu_3|\bar{B}|\nu_4\rangle\langle\nu_4|S^{t_1/a}|\nu_5\rangle \\ =& \frac{1}{Z}\sum_{\nu_1\ldots\nu_5} e^{-(L_t-(t_2-t_1))E_{\nu_1}}\langle\nu_1|B|\nu_2\rangle e^{-(t_2-t_1)E_{\nu_2}}\langle\nu_2|\bar{B}|\nu_1\rangle.\end{aligned} \tag{7.7.3}$$

For $L_t \to \infty$ and the energies chosen such that $E_0 = 0$ only few terms survive $Z \to 1$:

$$\langle B(t_1)\bar{B}(t_1)\rangle = \langle 0|B|0\rangle\langle 0|\bar{B}|0\rangle + \sum_{\nu>0}\langle 0|B|\nu\rangle\langle\nu|\bar{B}|0\rangle e^{-(t_2-t_1)E_\nu} + \sum_{\nu>0}\langle 0|B|\nu\rangle\langle\nu|\bar{B}|0\rangle e^{-(L_t-(t_2-t_1))E_\nu}. \tag{7.7.4}$$

The most reasonable procedure on the lattice is to create the particle at time zero and to measure it at a variable time $t$. This defines a correlator:

$$C(t) = \langle B(t)\bar{B}(0)\rangle = \langle 0|B|0\rangle\langle 0|\bar{B}|0\rangle + \sum_{\nu>0}\langle 0|B|\nu\rangle\langle\nu|\bar{B}|0\rangle e^{-tE_\nu} + \sum_{\nu>0}\langle 0|B|\nu\rangle\langle\nu|\bar{B}|0\rangle e^{-(L_t-t))E_\nu}. \tag{7.7.5}$$

This formula can be interpreted as the sum of the amplitudes that the particle is part of the vacuum (which is zero in most cases), the amplitudes that any intermediate particle propagates from 0 to $t$ and the amplitudes that any intermediate antiparticle propagates from $L_t$ back to $t$. In most cases, where the separation between the ground state $G$ produced by $\bar{B}$ and the excited states is large, the contributions of the higher states fall off much faster than the contribution of the ground state. So for values of $0 \ll t \ll L_t/2$ we can write:

$$C(t) \approx \langle 0|B|G\rangle\langle G|\bar{B}|0\rangle e^{-tE_G}. \tag{7.7.6}$$

This essential result allowes for the extraction of masses from a lattice simulation. The strength of the exponential decay in time is controlled by the energy of the ground state $G$ produced by the operator $\bar{B}$. It is extremely useful to define an observable called effective mass by

$$m_{\mathrm{eff}}(n_t + 1/2) = \ln\frac{C(an_t)}{C(an_t + a)} \tag{7.7.7}$$

which corresponds to a fit of $C(t) = Ae^{-mt}$ to the pair of data points around $n_t + 1/2$. Once the correlator is dominated by the ground state energy, $m_{\text{eff}}$ becomes constant and forms an effective mass plateau at that ground state energy.

## 7.8 Extraction of Matrix Elements

In section 3.10 we have seen how to extract masses of composite particles using the transfer matrix formalism. Now we are interested in matrix elements of certain operators $\mathcal{O}$ in the background of some particle $N$:

$$\langle N|\mathcal{O}|N\rangle \tag{7.8.1}$$

Unfortunately we do not have to full wavefunctions $|N\rangle$ at hand, but using the trick of dividing certain three-point functions by certain two-point functions (i.e. correlators) we can extract the interesting quantities. In contrast to the extraction of masses we do not analyze its behavior in time but its amplitude to calculate matrix elements with the help of three-point functions. The transfer matrix formalism predicts for the three-point functions:

$$C_3(\tau,t) = \langle B(t)\mathcal{O}(\tau)\bar{B}(0)\rangle = \frac{1}{Z}\mathrm{Tr}\left(S^{N_t-t/a}BS^{(t-\tau)/a}\mathcal{O}(\tau)\bar{B}S^{\tau/a}\right). \tag{7.8.2}$$

By inserting identities, taking again the limit $0 \ll \tau \ll t \ll L_t/2$, such that higher states than $N$ are suppressed, and keeping in mind $\langle 0|B|0\rangle = 0 = \langle 0|\bar{B}|0\rangle$ (for baryons), we may write for the three-point correlator $C3(\tau,t)$ (as the operator $\mathcal{O}$ has no effective creation and annihilation content):

$$C_3(\tau,t) \approx \langle 0|B|N\rangle\langle N|\mathcal{O}|N\rangle\langle N|\bar{B}|0\rangle e^{-tE_N}. \tag{7.8.3}$$

Finally we can divide three- by two-point correlator to obtain their ratio $R$,

$$R(\tau,t) \equiv \frac{C_3(\tau,t)}{C(t)} = \frac{\langle 0|B|N\rangle\langle N|\mathcal{O}|N\rangle\langle N|\bar{B}|0\rangle e^{-tE_N}}{\langle 0|B|N\rangle\langle N|\bar{B}|0\rangle e^{-tE_N}} = \langle N|\mathcal{O}|N\rangle \tag{7.8.4}$$

to get our matrix element. In real calculations the independence on $\tau$ should thus lead to a plateau-type behavior between time zero and $t$. To convert it to the standard continuum normalisation one has to take

$$R(\tau,t) \equiv \frac{C_3(\tau,t)}{C(t)} = \frac{1}{2E_N}\langle N|\mathcal{O}|N\rangle_{\text{continuum}}. \tag{7.8.5}$$

Now, we need to find the proper operators to access the spin structure of the $\Lambda^0$ hyperon. On the lattice the choice of the operators $\mathcal{O}$ is a non-trivial task, because the discretisation reduces the symmetry group of (Euclidean) space-time from $O(4)$ to the hypercubic group $H(4) \subset O(4)$. Therefore, one has to find combinations of operators which avoid the problem of operator mixing [G$^+$96]. After renormalisation, the matrix elements of these operators are expressed in terms of the reduced matrix elements $v_2$, $a_0$, $a_1$ and $t_0$ which correspond to moments of the parton distribution functions. We will work with the operators [G$^+$02]:

$$\mathcal{O}_{v_2} = \frac{1}{2}\bar{q}(\gamma_4 \overleftrightarrow{D}_4 - \frac{1}{3}(\gamma_1 \overleftrightarrow{D}_1 + \gamma_2 \overleftrightarrow{D}_2 + \gamma_3 \overleftrightarrow{D}_3))q, \tag{7.8.6}$$

$$\mathcal{O}_{a_0} = \frac{1}{2}\bar{q}\gamma_2\gamma_5 q, \tag{7.8.7}$$

$$\mathcal{O}_{a_1} = \frac{1}{2}\bar{q}(\gamma_4\gamma_5 \overleftrightarrow{D}_2 + \gamma_2\gamma_5 \overleftrightarrow{D}_4), \tag{7.8.8}$$

$$\mathcal{O}_{t_0} = \frac{1}{2}\bar{q}\sigma_{24}\gamma_5 q. \tag{7.8.9}$$

While the $v_2$ operator is used in a spin-averaged matrix element, the other operators require a polarised baryon state to give a non-zero result. In these latter cases we choose the spin to point into the 2-direction. In parton model language we have (this can be derived with help of the operator product expansion (OPE)):

$$v_2^q = \langle xq(x)\rangle, \tag{7.8.10}$$

$$a_0^q = 2\langle \Delta q(x)\rangle, \tag{7.8.11}$$

$$a_1^q = 2\langle x\Delta q(x)\rangle, \tag{7.8.12}$$

$$\mathcal{O}_{t_0} = 2\langle \delta q(x)\rangle. \tag{7.8.13}$$

For baryons with momentum zero the ratios $R_{\mathcal{O}}$ are related to the reduced matrix elements by

$$R_{\mathcal{O}_{v_2}} = -\frac{1}{Z_{v_2}(1+b_{v_2}am)}\frac{1}{2\kappa}Mv_2, \tag{7.8.14}$$

$$R_{\mathcal{O}_{a_0}} = \frac{i}{Z_{a_0}(1+b_{a_0}am)}\frac{1}{2\kappa}Ma_0, \tag{7.8.15}$$

$$R_{\mathcal{O}_{a_1}} = \frac{i}{Z_{a_1}(1+b_{a_1}am)}\frac{1}{2\kappa}\frac{M}{4}a_1, \tag{7.8.16}$$

$$R_{\mathcal{O}_{t_0}} = \frac{1}{Z_{t_0}(1+b_{t_0}am)}\frac{1}{2\kappa}\frac{1}{2}t_0. \tag{7.8.17}$$

Depending on the flavour of the quark flavor $q$ one has to insert the appropriate quark mass $\kappa_q$. These relations account for the operator renormalisation and different normalisations on the lattice and in the continuum. The renormalisation constants $Z_{v_2}, Z_{a_0}, Z_{a_1}, Z_{t_0}$ depend on the renormalisation scale $\mu$ of the continuum theory and the lattice cut-off $1/a$ or equivalently $\beta$.

# Chapter 8

# Calculation of the Two- and Three-Point-Functions

This chapter addresses the calculation of the appropriate three-point functions to access the spin structure of the $\Lambda^0$. Furthermore, two-point functions are presented which allow to caluclate masses of different baryons and mesons with strangeness content. We provide these two-point function in order to extract the physical strange quark mass from the lattice results. At the end of the chapter we will give a short status report on the development of the software package which allows to simulate the two- and three-point functions on the APE-mille machines at DESY Zeuthen.

## 8.1 Two Point Correlation Functions

In the subsequent subsections we want to derive expressions for two-point correlation functions of mesons and baryons whose quark masses are non-degenerate.

### 8.1.1 The Meson Case: $K^+$

First we want to caluclate the two-point correlator for the meson case. Our meson of choice is the positive Kaon. Its quantum numerbs are $J^{PC} = 0^{--}$ and its quark content is given by $|K^+\rangle \equiv |K\rangle = |u\bar{s}\rangle$. The interpolating fields of choice are

$$\begin{aligned} K(t;\vec{p}) &= \sum_{\vec{x}} e^{-i\vec{p}\vec{x}} \bar{s}(\vec{x},t)\gamma_5 u(\vec{x},t), \\ \bar{K}(t;\vec{p}) &= \sum_{\vec{y}} e^{+i\vec{p}\vec{y}} \bar{u}(\vec{y},t)\gamma_5 s(\vec{y},t). \end{aligned} \tag{8.1.1}$$

These fields can be combined in the two point function of the Kaon as follows

$$C(t;\vec{p}) = \langle K(t;\vec{p})\bar{K}(0;\vec{p})\rangle = \sum_{\vec{x},\vec{y}} e^{-i\vec{p}(\vec{x}-\vec{y})} \left\langle \bar{s}(\vec{x},t)\gamma_5 u(\vec{x},t)\bar{u}(\vec{y},0)\gamma_5 s(\vec{y},0)\right\rangle . \tag{8.1.2}$$

Exploiting translational invariance which is only recovered in the full ensemble average we can shift $\vec{y}$ to zero and obtain a multiplicative factor of $N_s^3$. Furthermore we use $\gamma_5$ hermiticity:

$$\begin{aligned} C(t;\vec{p}) &= -N_s^3 \sum_{\vec{x}} e^{-i\vec{p}\vec{x}} \mathrm{Tr}_{\mathrm{DC}} \left( {}^{SS}_{s}G(\vec{0},0;\vec{x},t)\,\gamma_5\, {}^{SS}_{u}G(\vec{x},t;\vec{0},0)\,\gamma_5 \right) \\ &= -N_s^3 \sum_{\vec{x}} e^{-i\vec{p}\vec{x}} \mathrm{Tr}_{\mathrm{DC}} \left( {}^{SS}_{s}G^{\dagger_{DC}}(\vec{x},t;\vec{0},0)\, {}^{SS}_{u}G(\vec{x},t;\vec{0},0) \right). \end{aligned} \tag{8.1.3}$$

The traces are applied in Dirac- as well as in color-Space.

### 8.1.2 The Baryon Case I: The $\Lambda^0$ Hyperon

Now we want to have a look at a baryonic two point function, namely the one of the $\Lambda^0$-Baryon. Its quark content is $|\Lambda^0\rangle \equiv |\Lambda\rangle = |uds\rangle$ which makes the contractions of the corresponding quark fields easier compared to the case of the nucleon (the proton or the neutron case repectively [WDL92]. It is part of the baryon octet and depicts the SU(3)-singlet part. Its quantum numbers are $J^P = \frac{1}{2}^+$. In the calculations we use the following interpolating fields [G$^+$02]

$$\begin{aligned}\Lambda_\alpha(t;\vec{p}) &= \sum_{\vec{x}} e^{-i\vec{p}\vec{x}}\varepsilon^{abc} s^a_\alpha(\vec{x},t)\Big[u^b(\vec{x},t)^T C\gamma_5 d^c(\vec{x},t)\Big],\\ \bar{\Lambda}_\beta(t;\vec{p}) &= \sum_{\vec{y}} e^{+i\vec{p}\vec{y}}\varepsilon^{a'b'c'} \bar{s}^{a'}_\beta(\vec{y},t)\Big[\bar{d}^{b'}(\vec{y},t)\gamma_5 C^{-1}\bar{u}^{c'}(\vec{y},t)^T\Big].\end{aligned} \tag{8.1.4}$$

The $\gamma_5$-matrix gives rise to a diquark with spin $J = 0$ and together with the quark outside the diquark the resulting interpolator has spin $J = \frac{1}{2}$. Combining the fields given in (8.1.4) in the corresponding two-point function yields

$$\begin{aligned}C_{\alpha\beta}(t;\vec{p}) &= \langle \Lambda_\alpha(t;\vec{p})\bar{\Lambda}_\beta(0;\vec{p})\rangle\\ &= \sum_{\vec{x},\vec{y}} e^{-i\vec{p}(\vec{x}-\vec{y})}\varepsilon^{abc}\varepsilon^{a'b'c'}\\ &\quad\times\Big\langle s^a_\alpha(\vec{x},t)\Big[u^b_\gamma(\vec{x},t)^T(C\gamma_5)_{\gamma\delta}d^c_\delta(\vec{x},t)\Big]\bar{s}^{a'}_\beta(\vec{y},0)\Big[\bar{d}^{b'}_\varepsilon(\vec{y},0)(\gamma_5 C^{-1})_{\varepsilon\rho}\bar{u}^{c'}_\rho(\vec{y},0)^T\Big]\Big\rangle.\end{aligned} \tag{8.1.5}$$

Exploiting translational invariance which is only recovered in the full ensemble average we can shift $\vec{y}$ to zero and obtain a multiplicative factor of $N_s^3$. Perfoming the following Wick contractions

$$\Big\langle s^a_\alpha(\vec{x},t)\Big[u^b_\gamma(\vec{x},t)^T(C\gamma_5)_{\gamma\delta}d^c_\delta(\vec{x},t)\Big]\bar{s}^{a'}_\beta(\vec{y},0)\Big[\bar{d}^{b'}_\varepsilon(\vec{y},0)(\gamma_5 C^{-1})_{\varepsilon\rho}\bar{u}^{c'}_\rho(\vec{y},0)^T\Big]\Big\rangle$$

one obtains

$$\begin{aligned}C_{\alpha\beta}(t;\vec{p}) &= N_s^3\sum_{\vec{x}} e^{-i\vec{p}\vec{x}}\varepsilon^{abc}\varepsilon^{a'b'c'}(C\gamma_5)_{\gamma\delta}(\gamma_5 C^{-1})_{\varepsilon\rho}\left({}^{SS}_{s}G^{aa'}_{\alpha\beta}(\vec{x},t;0)\,{}^{SS}_{u}G^{bc'}_{\gamma\rho}(\vec{x},t;0)\,{}^{SS}_{d}G^{cb'}_{\delta\varepsilon}(\vec{x},t;0)\right)\\ &= -N_s^3\sum_{\vec{x}} e^{-i\vec{p}\vec{x}}\varepsilon^{abc}\varepsilon^{a'b'c'}\Big\{{}^{SS}_{s}G^{aa'}_{\alpha\beta}(\vec{x},t;0)\\ &\quad\times\mathrm{Tr}\left({}^{SS}_{u}G^{bb'}(\vec{x},t;0)\,(\gamma_5 C^{-1})^T\,{}^{SS}_{d}G^{cc'}(\vec{x},t;0)^T\,(C\gamma_5)^T\right)\Big\}.\end{aligned} \tag{8.1.6}$$

We finally define the common tilde notation which is common throughout literature (Ref. [WDL92, Gup98])

$$\widetilde{X} = (\gamma_5 C^{-1})^T X^{T_D}(C\gamma_5)^T = \gamma_5 C^{-1} X^{T_D} C\gamma_5, \tag{8.1.7}$$

and obtain

$$C_{\alpha\beta}(t;\vec{p}) = -N_s^3\sum_{\vec{x}} e^{-i\vec{p}\vec{x}}\varepsilon^{abc}\varepsilon^{a'b'c'}\Big\{{}^{SS}_{s}G^{aa'}_{\alpha\beta}(\vec{x},t;0)\,\mathrm{Tr}\left({}^{SS}_{u}G^{bb'}(\vec{x},t;0)\,{}^{SS}_{d}\widetilde{G}^{cc'}(\vec{x},t;0)\right)\Big\}. \tag{8.1.8}$$

As the $\Lambda^0$ Hyperon has positive parity we have to apply the positive parity projector

$$\Gamma = \tfrac{1}{2}(\mathbb{1}+\gamma^0_M) = \tfrac{1}{2}(\mathbb{1}+\gamma^4_E) \tag{8.1.9}$$

on the correlator. The result for the $\Lambda^0$ two point function finally reads

$$\begin{aligned}C^\Gamma(t;\vec{p}) &= \Gamma_{\beta\alpha}C_{\alpha\beta}(t;\vec{p}) = -N_s^3\sum_{\vec{x}} e^{-i\vec{p}\vec{x}}\varepsilon^{abc}\varepsilon^{a'b'c'}\\ &\quad\times\mathrm{Tr}\left(\Gamma\,{}^{SS}_{s}G^{aa'}(\vec{x},t;0)\right)\mathrm{Tr}\left({}^{SS}_{u}G^{bb'}(\vec{x},t;0)\,{}^{SS}_{d}\widetilde{G}^{cc'}(\vec{x},t;0)\right).\end{aligned} \tag{8.1.10}$$

### 8.1.3 The Baryon Case II: The $\Omega^-$ Hyperon

In this subsection we want to discuss the two-point function of the $\Omega^-$. It is member of the baryon decuplet and its quantum numbers are $J^P = \frac{3}{2}^+$. The quark content of the $\Omega$-hyperon is given $|\Omega^-\rangle \equiv |\Omega\rangle = |sss\rangle$ and, thus, we use the following interpolating fields for the construction of the corresponding two-point function (cf. Reference [LMR$^+$05, LDW92])

$$\begin{aligned}\Omega^i_\alpha(t;\vec{p}) &= \sum_{\vec{x}} e^{-i\vec{p}\vec{x}}\varepsilon^{abc} s^a_\alpha(\vec{x},t)\Big[s^b(\vec{x},t)^T C\gamma_i s^c(\vec{x},t)\Big],\\ \bar{\Omega}^j_\beta(t;\vec{p}) &= \sum_{\vec{y}} e^{+i\vec{p}\vec{y}}\varepsilon^{a'b'c'} \bar{s}^{a'}_\beta(\vec{y},t)\Big[\bar{s}^{b'}(\vec{y},t)\gamma_j C^{-1}\bar{s}^{c'}(\vec{y},t)^T\Big].\end{aligned} \tag{8.1.11}$$

The spatial $\gamma_j$-matrix gives rise to a diquark with spin $J = 1$ and together with the quark outside the diquark the resulting interpolator has spin $J = \frac{3}{2}$. Combining the fields given in (8.1.11) in the corresponding two-point function yields

$$\begin{aligned}C^{\alpha\beta}_{ij}(t;\vec{p}) &= \langle \Omega^\alpha_i(t;\vec{p})\bar{\Omega}^\beta_j(0;\vec{p})\rangle\\ &= \sum_{\vec{x},\vec{y}} e^{-i\vec{p}(\vec{x}-\vec{y})}\varepsilon^{abc}\varepsilon^{a'b'c'}\\ &\quad\times\Big\langle s^a_\alpha(\vec{x},t)\Big[s^b_\gamma(\vec{x},t)^T(C\gamma_i)_{\gamma\delta}s^c_\delta(\vec{x},t)\Big]\bar{s}^{a'}_\beta(\vec{y},0)\Big[\bar{s}^{b'}_\varepsilon(\vec{y},0)(\gamma_j C^{-1})_{\varepsilon\rho}\bar{s}^{c'}_\rho(\vec{y},0)^T\Big]\Big\rangle.\end{aligned} \tag{8.1.12}$$

We changed the notation compared to the previous sub-sections. Due to the additional Lorentz indices $i$ and $j$ in the interpolating fields we defined the Dirac indices $\alpha$ and $\beta$ as upper left superscripts. For the caluclation of the two-point correlator we have to perform the following Wick contractions

$$\Big\langle \overbrace{s\,s\,s\,\bar{s}\,\bar{s}\,\bar{s}}\Big\rangle = -\,{}_sG^{aa'}_{\alpha\beta}(\vec{x},t;\vec{y},0)\,{}_sG^{bb'}_{\gamma\varepsilon}(\vec{x},t;\vec{y},0)\,{}_sG^{cc'}_{\delta\rho}(\vec{x},t;\vec{y},0) \tag{8.1.13}$$

$$\Big\langle \overbrace{s\,s\,s\,\bar{s}\,\bar{s}\,\bar{s}}\Big\rangle = +\,{}_sG^{aa'}_{\alpha\beta}(\vec{x},t;\vec{y},0)\,{}_sG^{bc'}_{\gamma\rho}(\vec{x},t;\vec{y},0)\,{}_sG^{cb'}_{\delta\varepsilon}(\vec{x},t;\vec{y},0) \tag{8.1.14}$$

$$\Big\langle \overbrace{s\,s\,s\,\bar{s}\,\bar{s}\,\bar{s}}\Big\rangle = +\,{}_sG^{ac'}_{\alpha\rho}(\vec{x},t;\vec{y},0)\,{}_sG^{bb'}_{\gamma\varepsilon}(\vec{x},t;\vec{y},0)\,{}_sG^{ca'}_{\delta\beta}(\vec{x},t;\vec{y},0) \tag{8.1.15}$$

$$\Big\langle \overbrace{s\,s\,s\,\bar{s}\,\bar{s}\,\bar{s}}\Big\rangle = +\,{}_sG^{ab'}_{\alpha\varepsilon}(\vec{x},t;\vec{y},0)\,{}_sG^{ba'}_{\gamma\beta}(\vec{x},t;\vec{y},0)\,{}_sG^{cc'}_{\delta\rho}(\vec{x},t;\vec{y},0) \tag{8.1.16}$$

$$\Big\langle \overbrace{s\,s\,s\,\bar{s}\,\bar{s}\,\bar{s}}\Big\rangle = -\,{}_sG^{ac'}_{\alpha\rho}(\vec{x},t;\vec{y},0)\,{}_sG^{ba'}_{\gamma\beta}(\vec{x},t;\vec{y},0)\,{}_sG^{cb'}_{\delta\varepsilon}(\vec{x},t;\vec{y},0) \tag{8.1.17}$$

$$\Big\langle \overbrace{s\,s\,s\,\bar{s}\,\bar{s}\,\bar{s}}\Big\rangle = -\,{}_sG^{ab'}_{\alpha\varepsilon}(\vec{x},t;\vec{y},0)\,{}_sG^{bc'}_{\gamma\rho}(\vec{x},t;\vec{y},0)\,{}_sG^{ca'}_{\delta\beta}(\vec{x},t;\vec{y},0). \tag{8.1.18}$$

Exploiting translational invariance which is only recovered in the full ensemble average we can shift $\vec{y}$ to zero and obtain a multiplicative factor of $N_s^3$. Furthermore we define the four vecotrs $x = (\vec{x},t)$ and $0 = (\vec{0},0)$. Merging Equations (8.1.13) - (8.1.14) into the corresponding two-point function and keeping the following notation in mind

$$\widehat{X} = (\gamma_i C^{-1})^T X^{T_D}(C\gamma_j)^T = (\gamma_i C^{-1})X^{T_D}(C\gamma_j), \tag{8.1.19}$$

yields

$$
\begin{aligned}
C_{ij}^{\alpha\beta}(t;\vec{p}) &= \langle \Omega_i^{\alpha}(t;\vec{p})\bar{\Omega}_j^{\beta}(0;\vec{p})\rangle \\
&= N_s^3 \sum_{\vec{x}} e^{-i\vec{p}\vec{x}} \varepsilon^{abc}\varepsilon^{a'b'c'} (C\gamma_i)_{\gamma\delta}(\gamma_j C^{-1})_{\varepsilon\rho} \times \\
&\quad \times \Big\{ -{}_sG_{\alpha\beta}^{aa'}(x;0)\,{}_sG_{\gamma\varepsilon}^{bb'}(x;0)\,{}_sG_{\delta\rho}^{cc'}(x;0) + {}_sG_{\alpha\beta}^{aa'}(x;0)\,{}_sG_{\gamma\rho}^{bc'}(x;0)\,{}_sG_{\delta\varepsilon}^{cb'}(x;0) \\
&\quad + {}_sG_{\alpha\rho}^{ac'}(x;0)\,{}_sG_{\gamma\varepsilon}^{bb'}(x;0)\,{}_sG_{\delta\beta}^{ca'}(x;0) + {}_sG_{\alpha\varepsilon}^{ab'}(x;0)\,{}_sG_{\gamma\beta}^{ba'}(x;0)\,{}_sG_{\delta\rho}^{cc'}(x;0) \\
&\quad - {}_sG_{\alpha\rho}^{ac'}(x;0)\,{}_sG_{\gamma\beta}^{ba'}(x;0)\,{}_sG_{\delta\varepsilon}^{cb'}(x;0) - {}_sG_{\alpha\varepsilon}^{ab'}(x;0)\,{}_sG_{\gamma\rho}^{bc'}(x;0)\,{}_sG_{\delta\beta}^{ca'}(x;0) \Big\} \\
&= N_s^3 \sum_{\vec{x}} e^{-i\vec{p}\vec{x}} \varepsilon^{abc}\varepsilon^{a'b'c'} \times \\
&\quad \times \Big\{ -{}_sG_{\alpha\beta}^{aa'}(x;0)\,\mathrm{Tr}\Big({}_s\widehat{G}^{bb'}(x;0)\,{}_sG^{cc'}(x;0)\Big) + {}_sG_{\alpha\beta}^{aa'}(x;0)\,\mathrm{Tr}\Big({}_s\widehat{G}^{bc'}(x;0)\,{}_sG^{cb'}(x;0)\Big) \\
&\quad + \Big({}_sG^{ac'}(x;0)\,{}_s\widehat{G}^{bb'}(x;0)\,{}_sG^{ca'}(x;0)\Big)_{\alpha\beta} + \Big({}_sG^{ab'}(x;0)\,{}_s\widehat{G}^{cc'}(x;0)\,{}_sG^{ba'}(x;0)\Big)_{\alpha\beta} \\
&\quad - \Big({}_sG^{ac'}(x;0)\,{}_s\widehat{G}_{\gamma\beta}^{cb'}(x;0)\,{}_sG^{ba'}(x;0)\Big)_{\alpha\beta} - \Big({}_sG^{ab'}(x;0)\,{}_s\widehat{G}^{bc'}(x;0)\,{}_sG^{ca'}(x;0)\Big)_{\alpha\beta} \Big\} \\
&= N_s^3 \sum_{\vec{x}} e^{-i\vec{p}\vec{x}} \varepsilon^{abc}\varepsilon^{a'b'c'} \times \\
&\quad \times \Big\{ -{}_sG_{\alpha\beta}^{aa'}(x;0)\,\mathrm{Tr}\Big({}_s\widehat{G}^{bb'}(x;0)\,{}_sG^{cc'}(x;0)\Big) - {}_sG_{\alpha\beta}^{aa'}(x;0)\,\mathrm{Tr}\Big({}_s\widehat{G}^{bb'}(x;0)\,{}_sG^{cc'}(x;0)\Big) \\
&\quad - \Big({}_sG^{aa'}(x;0)\,{}_s\widehat{G}^{bb'}(x;0)\,{}_sG^{cc'}(x;0)\Big)_{\alpha\beta} - \Big({}_sG^{aa'}(x;0)\,{}_s\widehat{G}^{bb'}(x;0)\,{}_sG^{cc'}(x;0)\Big)_{\alpha\beta} \\
&\quad - \Big({}_sG^{cc'}(x;0)\,{}_s\widehat{G}^{bb'}(x;0)\,{}_sG^{cc'}(x;0)\Big)_{\alpha\beta} - \Big({}_sG^{aa'}(x;0)\,{}_s\widehat{G}^{bb'}(x;0)\,{}_sG^{cc'}(x;0)\Big)_{\alpha\beta} \Big\} \\
&= -N_s^3 \sum_{\vec{x}} e^{-i\vec{p}\vec{x}} \varepsilon^{abc}\varepsilon^{a'b'c'} \times \\
&\quad \times \Big\{ 2\,{}_sG_{\alpha\beta}^{aa'}(x;0)\,\mathrm{Tr}\Big({}_s\widehat{G}^{bb'}(x;0)\,{}_sG^{cc'}(x;0)\Big) + 4\Big({}_sG^{aa'}(x;0)\,{}_s\widehat{G}^{bb'}(x;0)\,{}_sG^{cc'}(x;0)\Big)_{\alpha\beta} \Big\}
\end{aligned}
\tag{8.1.20}
$$

Like in the case of the $\Lambda^0$-hyperon we have to apply the projector (8.1.9) on the two-point function (8.1.20) of the $\Omega^-$ as well. One finally finds.

$$
\begin{aligned}
C_{ij}(t;\vec{p}) &= \Gamma_{\beta\alpha} C_{ij}^{\alpha\beta}(t;\vec{p}) \\
&= -N_s^3 \sum_{\vec{x}} e^{-i\vec{p}\vec{x}} \varepsilon^{abc}\varepsilon^{a'b'c'} \times \\
&\quad \times \Big\{ 2\,\mathrm{Tr}\Big(\Gamma\,{}_sG^{aa'}(x;0)\Big)\,\mathrm{Tr}\Big({}_s\widehat{G}^{bb'}(x;0)\,{}_sG^{cc'}(x;0)\Big) \\
&\qquad + 4\,\mathrm{Tr}\Big(\Gamma\,{}_sG^{aa'}(x;0)\,{}_s\widehat{G}^{bb'}(x;0)\,{}_sG^{cc'}(x;0)\Big) \Big\}
\end{aligned}
\tag{8.1.21}
$$

Now, we can find unclosed Lorentz indices in the expression for the two-point correlator $C_{ij}(t;\vec{p})$. As the $\Omega^-$-hyperon is a spin-$\frac{3}{2}$ particle one can argue to apply an additional Spin projector on the two-point correlator. Leinweber et al. [LDW92] showed, though, that the overlap of the interpolating fields of the $\Delta$- baryons and of the $\Omega^-$ with spin-$\frac{1}{2}$ baryons is neglibible. This is due to the fact that these baryons are the lowest-lying baryons in the mass spectrum having the appropriate isospin and strangeness quantum numbers.

## 8.2 Three Point Correlation Functions

For the three point correlation function we want to restrict our calculations to the baryonic case.

### 8.2.1 The Three Point Function of the $\Lambda^0$ Hyperon

The purpose of evaluating three-point correlation functions is to extract the expectation values of a given operator $\mathcal{O}$. This operator $\mathcal{O}$ is inserted at time slice $\tau$. The three-point correlator then reads

$$
C_{\alpha\beta}^{\mathcal{O}_q}(t,\tau;\vec{p}) = \left\langle \Lambda_\alpha(t;\vec{p})\mathcal{O}_q(\tau)\bar{\Lambda}_\alpha(0;\vec{p})\right\rangle . \tag{8.2.1}
$$

The operator $\mathcal{O}_q(\tau)$ can be decomposed as follows

$$\mathcal{O}_q(\tau) = \sum_{\vec{y}} \mathcal{O}(\vec{y},\tau) = \sum_{\vec{y},v,w} \bar{q}^a_\alpha(v)\mathcal{O}^{ab}_{\alpha\beta}(v,w;\vec{y},\tau)q^b_\beta(w). \tag{8.2.2}$$

As in the case of the two-point correlator we are only interested in the positive parity states. We project them out by using the following projector [GHI+96]

$$\Gamma^{(i)} = \tfrac{1}{2}(\mathbb{1}+\gamma^4)\mathrm{i}\gamma^5\gamma^i. \tag{8.2.3}$$

In contrast to the projector we used in the calculations for the two-point correlators (8.1.9) there are additional terms $\mathrm{i}\gamma^5\gamma^i$ in the projector for the three-point function. These terms serve as polarization projectors in the (space) direction $i$, corresponding to the polarization $(+\,-\,-)$ in the $i$ direction. In the following calculations we omit the superscript $i$. Using the same interpolating fields as in the chapter before (c.f. formula (8.1.4)) one obtains for the three-point correlation function

$$\begin{aligned} C^{\mathcal{O}_q}_\Gamma(t,\tau;\vec{p}) &= \Gamma_{\beta\alpha}\left\langle \Lambda_\alpha(t;\vec{p})\mathcal{O}_q(\tau)\bar{\Lambda}_\beta(0;\vec{p})\right\rangle \\ &= \sum_{\vec{y},v,w}\sum_{\vec{x},\vec{z}} e^{-i\vec{p}(\vec{x}-\vec{z})}\varepsilon^{abc}\varepsilon^{a'b'c'}(C\gamma_5)_{\gamma\delta}(\gamma_5 C^{-1})_{\varepsilon\rho}\Gamma_{\beta\alpha}\mathcal{F}^q_{\alpha\beta}, \end{aligned} \tag{8.2.4}$$

where we define the object $\mathcal{F}^q_{\alpha\beta}$ as follows

$$\begin{aligned} \mathcal{F}^q_{\alpha\beta} &= \left\langle s^a_\alpha(\vec{x},t)u^b_\gamma(\vec{x},t)d^c_\delta(\vec{x},t)\bar{q}^d_\sigma(v)\mathcal{O}^{de}_{\sigma\chi}(v,w;\vec{y},\tau)q^e_\chi(w)\bar{s}^{a'}_\beta(\vec{z},0)\bar{d}^{b'}_\varepsilon(\vec{z},0)\bar{u}^{c'}_\rho(\vec{z},0)\right\rangle \\ &\propto \left\langle s\,u\,d\,\bar{q}\,q\,\bar{s}\,\bar{d}\,\bar{u}\right\rangle \end{aligned} \tag{8.2.5}$$

The quarks denotetd by $q$ are treated as local quarks. This means that the corresponding quark fields of flavour $q$ are not smeared and the resulting propagator term has an upper-left superscript $L$, depending whether the sink (${}^{LS}_{q}G$) or the source (${}^{SL}_{q}G$) are treated as local. Now we can subesequently insert for $q$ the different quarks of flavours $u$, $d$ and $s$. Regarding the $u$- and $d$-quarks as degenerate in mass and following Wick's theorem we obtain the following contractions:

- $s$-quark insertion: $\left\langle s\,u\,d\,\bar{s}\,s\,\bar{s}\,\bar{d}\,\bar{u}\right\rangle$

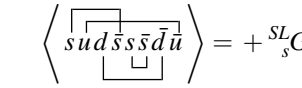

$$= +\,{}^{SL}_{s}G^{ad}_{\alpha\sigma}(\vec{x},t;v)\,{}^{SS}_{u}G^{bc'}_{\gamma\rho}(\vec{x},t;\vec{z},0)\,{}^{SS}_{d}G^{cb'}_{\delta\varepsilon}(\vec{x},t;\vec{z},0)\,{}^{LS}_{s}G^{ea'}_{\chi\beta}(w;\vec{z},0) \tag{8.2.6}$$

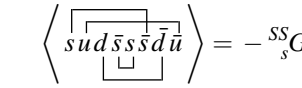

$$= -\,{}^{SS}_{s}G^{aa'}_{\alpha\beta}(\vec{x},t;\vec{z},0)\,{}^{SS}_{u}G^{bc'}_{\gamma\rho}(\vec{x},t;\vec{z},0)\,{}^{SS}_{d}G^{cb'}_{\delta\varepsilon}(\vec{x},t;\vec{z},0)\,{}^{LL}_{s}G^{ed}_{\chi\sigma}(w;v) \tag{8.2.7}$$

- $u$-quark insertion: $\left\langle s\,u\,d\,\bar{u}\,u\,\bar{s}\,\bar{d}\,\bar{u}\right\rangle$

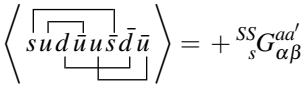

$$= +\,{}^{SS}_{s}G^{aa'}_{\alpha\beta}(\vec{x},t;\vec{z},0)\,{}^{SL}_{u}G^{bd}_{\gamma\sigma}(\vec{x},t;v)\,{}^{SS}_{d}G^{cb'}_{\delta\varepsilon}(\vec{x},t;\vec{z},0)\,{}^{LS}_{u}G^{ec'}_{\chi\rho}(w;\vec{z},0) \tag{8.2.8}$$

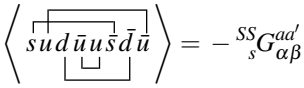

$$= -\,{}^{SS}_{s}G^{aa'}_{\alpha\beta}(\vec{x},t;\vec{z},0)\,{}^{SS}_{u}G^{bc'}_{\gamma\rho}(\vec{x},t;\vec{z},0)\,{}^{SS}_{d}G^{cb'}_{\delta\varepsilon}(\vec{x},t;\vec{z},0)\,{}^{LL}_{u}G^{ed}_{\chi\sigma}(w;v) \tag{8.2.9}$$

- $d$-quark insertion: $\left\langle s\,u\,d\,\bar{d}\,d\,\bar{s}\,\bar{d}\,\bar{u}\right\rangle$

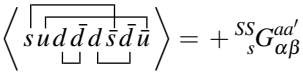

$$= +\,{}^{SS}_{s}G^{aa'}_{\alpha\beta}(\vec{x},t;\vec{z},0)\,{}^{SS}_{u}G^{bc'}_{\gamma\rho}(\vec{x},t;\vec{z},0)\,{}^{SL}_{d}G^{cd}_{\delta\sigma}(\vec{x},t;v)\,{}^{LS}_{d}G^{eb'}_{\chi\varepsilon}(w;\vec{z},0) \tag{8.2.10}$$

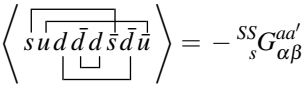

$$= -\,{}^{SS}_{s}G^{aa'}_{\alpha\beta}(\vec{x},t;\vec{z},0)\,{}^{SS}_{u}G^{bc'}_{\gamma\rho}(\vec{x},t;\vec{z},0)\,{}^{SS}_{d}G^{cb'}_{\delta\varepsilon}(\vec{x},t;\vec{z},0)\,{}^{LL}_{d}G^{ed}_{\chi\sigma}(w;v) \tag{8.2.11}$$

Now we can insert the terms obtained from the contractions into the three-point correlator. Combining formula (8.2.4) with the propagators from (8.2.6)-(8.2.11) allows us to construct the three-point function for the $\Lambda^0$-Baryon. By exploiting translational invariance in the full ensemble average we can shift $\vec{z}$ to zero and obtain a multiplicative factor of $N_s^3$. We finally get the following three-point correlators depending on which type of quark we insert in formula (8.2.2) for $q$. For the $d$-quark insertion we get

$$
\begin{aligned}
C_\Gamma^{\mathcal{O}_d}(t,\tau;\vec{p}) &= \Gamma_{\beta\alpha}\left\langle \Lambda_\alpha(t;\vec{p})\mathcal{O}_d(\tau)\bar{\Lambda}_\beta(0;\vec{p})\right\rangle \\
&= N_s^3 \sum_{\vec{x},\vec{y},v,w} e^{-i\vec{p}\vec{x}}\varepsilon^{abc}\varepsilon^{a'b'c'}(C\gamma_5)_{\gamma\delta}(\gamma_5 C^{-1})_{\varepsilon\rho}\Gamma_{\beta\alpha}\mathcal{F}^d_{\alpha\beta} \\
&= N_s^3 \sum_{\vec{x},\vec{y},v,w} e^{-i\vec{p}\vec{x}}\varepsilon^{abc}\varepsilon^{a'b'c'}(C\gamma_5)_{\gamma\delta}(\gamma_5 C^{-1})_{\varepsilon\rho}\Gamma_{\beta\alpha} \\
&\quad\times\Big\{ {}^{SS}_{s}G^{aa'}_{\alpha\beta}(\vec{x},t;\vec{0},0)\,{}^{SS}_{u}G^{bc'}_{\gamma\rho}(\vec{x},t;\vec{0},0)\,{}^{SL}_{d}G^{cd}_{\delta\sigma}(\vec{x},t;v)\,\mathcal{O}^{de}_{\sigma\chi}(v,w;\vec{y},\tau)\,{}^{LS}_{d}G^{eb'}_{\chi\varepsilon}(w;\vec{0},0) \\
&\quad- {}^{SS}_{s}G^{aa'}_{\alpha\beta}(\vec{x},t;\vec{0},0)\,{}^{SS}_{u}G^{bc'}_{\gamma\rho}(\vec{x},t;\vec{0},0)\,{}^{SS}_{d}G^{cb'}_{\delta\varepsilon}(\vec{x},t;\vec{0},0)\,\mathcal{O}^{de}_{\sigma\chi}(v,w;\vec{y},\tau)\,{}^{LL}_{d}G^{ed}_{\chi\sigma}(w;v)\Big\} \\
&= N_s^3 \sum_{\vec{x},\vec{y},v,w} e^{-i\vec{p}\vec{x}}\varepsilon^{abc}\varepsilon^{a'b'c'}\Gamma_{\beta\alpha} \\
&\quad\times\Big\{ {}^{SS}_{s}G^{aa'}_{\alpha\beta}(\vec{x},t;\vec{0},0)\,(\gamma_5 C^{-1})_{\varepsilon\rho}\,{}^{SS}_{u}G^{bc'}_{\rho\gamma}(\vec{x},t;\vec{0},0)^{T_D}\,(C\gamma_5)_{\gamma\delta}\,{}^{SL}_{d}G^{cd}_{\delta\sigma}(\vec{x},t;v)\,\mathcal{O}^{de}_{\sigma\chi}(v,w;\vec{y},\tau)\,{}^{LS}_{d}G^{eb'}_{\chi\varepsilon}(w;\vec{0},0) \\
&\quad- {}^{SS}_{s}G^{aa'}_{\alpha\beta}(\vec{x},t;\vec{0},0)\,(\gamma_5 C^{-1})_{\varepsilon\rho}\,{}^{SS}_{u}G^{bc'}_{\rho\gamma}(\vec{x},t;\vec{0},0)^{T_D}\,(C\gamma_5)_{\gamma\delta}\,{}^{SS}_{d}G^{cb'}_{\delta\varepsilon}(\vec{x},t;\vec{0},0)\,\mathcal{O}^{de}_{\sigma\chi}(v,w;\vec{y},\tau)\,{}^{LL}_{d}G^{ed}_{\chi\sigma}(w;v)\Big\} \\
&= N_s^3 \sum_{\vec{x},\vec{y},v,w} e^{-i\vec{p}\vec{x}}\varepsilon^{abc}\varepsilon^{a'b'c'}\Gamma_{\beta\alpha} \\
&\quad\times\Big\{ {}^{SS}_{s}G^{aa'}_{\alpha\beta}(\vec{x},t;\vec{0},0)\,\mathrm{Tr}\Big({}^{SS}_{u}\widetilde{G}^{bc'}(\vec{x},t;\vec{0},0)\,{}^{SL}_{d}G^{cd}(\vec{x},t;v)\,\mathcal{O}^{de}(v,w;\vec{y},\tau)\,{}^{LS}_{d}G^{eb'}(w;\vec{0},0)\Big) \\
&\quad- {}^{SS}_{s}G^{aa'}_{\alpha\beta}(\vec{x},t;\vec{0},0)\,\mathrm{Tr}\Big({}^{SS}_{u}\widetilde{G}^{bc'}(\vec{x},t;\vec{0},0)\,{}^{SS}_{d}G^{cb'}(\vec{x},t;\vec{0},0)\Big)\,\mathrm{Tr}\Big(\mathcal{O}^{de}(v,w;\vec{y},\tau)\,{}^{LL}_{d}G^{ed}(w;v)\Big)\Big\} \\
&= -N_s^3 \sum_{\vec{x},\vec{y},v,w} e^{-i\vec{p}\vec{x}}\varepsilon^{abc}\varepsilon^{a'b'c'}\,\mathrm{Tr}\Big(\Gamma\,{}^{SS}_{s}G^{aa'}(\vec{x},t;\vec{0},0)\Big) \\
&\quad\times\Big\{\underbrace{\mathrm{Tr}\Big({}^{SS}_{u}\widetilde{G}^{bb'}(\vec{x},t;\vec{0},0)\,{}^{SL}_{d}G^{cd}(\vec{x},t;v)\,\mathcal{O}^{de}(v,w;\vec{y},\tau)\,{}^{LS}_{d}G^{ec'}(w;\vec{0},0)\Big)}_{\text{connected part}} \\
&\quad\underbrace{-\,\mathrm{Tr}\Big({}^{SS}_{u}\widetilde{G}^{bb'}(\vec{x},t;\vec{0},0)\,{}^{SS}_{d}G^{cc'}(\vec{x},t;\vec{0},0)\Big)\,\mathrm{Tr}\Big(\mathcal{O}^{de}(v,w;\vec{y},\tau)\,{}^{LL}_{d}G^{ed}(w;v)\Big)}_{\text{disconnected part}}\Big\}.
\end{aligned}
\tag{8.2.12}
$$

In the case of an $u$-quark insertion we just have to replace the $d$-quarks in formula (8.2.12) by $u$-quarks. This replacement yields

$$
\begin{aligned}
C_\Gamma^{\mathcal{O}_u}(t,\tau;\vec{p}) = &-N_s^3 \sum_{\vec{x},\vec{y},v,w} e^{-i\vec{p}\vec{x}}\varepsilon^{abc}\varepsilon^{a'b'c'}\,\mathrm{Tr}\Big(\Gamma\,{}^{SS}_{s}G^{aa'}(\vec{x},t;\vec{0},0)\Big) \\
&\times\Big\{\underbrace{\mathrm{Tr}\Big({}^{SS}_{d}\widetilde{G}^{bb'}(\vec{x},t;\vec{0},0)\,{}^{SL}_{u}G^{cd}(\vec{x},t;v)\,\mathcal{O}^{de}(v,w;\vec{y},\tau)\,{}^{LS}_{u}G^{ec'}(w;\vec{0},0)\Big)}_{\text{connected part}} \\
&\underbrace{-\,\mathrm{Tr}\Big({}^{SS}_{d}\widetilde{G}^{bb'}(\vec{x},t;\vec{0},0)\,{}^{SS}_{u}G^{cc'}(\vec{x},t;\vec{0},0)\Big)\,\mathrm{Tr}\Big(\mathcal{O}^{de}(v,w;\vec{y},\tau)\,{}^{LL}_{u}G^{ed}(w;v)\Big)}_{\text{disconnected part}}\Big\}.
\end{aligned}
\tag{8.2.13}
$$

The three-point correlation function for the insertion of an $s$-quark consists of the two contractions calculated in (8.2.6) and (8.2.7). The algebraic structure differs a bit form the $u$- and $d$-quark cases. One finally obtains

$$\begin{aligned} C_\Gamma^{\mathcal{O}_s}(t,\tau;\vec{p}) = & -N_s^3 \sum_{\vec{x},\vec{y},v,w} e^{-i\vec{p}\vec{x}} \varepsilon^{abc}\varepsilon^{a'b'c'} \mathrm{Tr}\left( {}^{SS}_{u}\widetilde{G}^{bb'}(\vec{x},t;\vec{0},0)\, {}^{SS}_{d}G^{cc'}(\vec{x},t;\vec{0},0)\right) \\ & \times \Big\{ \underbrace{\mathrm{Tr}\left(\Gamma\, {}^{SL}_{s}G^{ad}(\vec{x},t;v)\, \mathcal{O}^{de}(v,w;\vec{y},\tau)\, {}^{LS}_{s}G^{ea'}(w;\vec{0},0)\right)}_{\text{connected part}} \\ & - \underbrace{\mathrm{Tr}\left(\Gamma\, {}^{SS}_{s}G^{aa'}(\vec{x},t;\vec{0},0)\right) \mathrm{Tr}\left(\mathcal{O}^{de}(v,w;\vec{y},\tau)\, {}^{LL}_{s}G^{ed}(w;v)\right)}_{\text{disconnected part}} \Big\}. \end{aligned} \tag{8.2.14}$$

So far the disconnected pieces of the three-point correlators were still taken into account. The calculations of lattice observables containing diconnected diagrams is especially difficult, since much more than a single column of the propagator is necessary for their evaluation since one requires propagators from any sink to any source. This vast amount of additional matrix inversions are typically several orders of magnitude more computationally expensive than for the calculation of the connected parts. Current development of eigenmode expansions and stochastic source techniques offer the prospect of calculating these contributions. One can nevertheless show that the contributions arising from the disconnected diagrams are negligible (cf. Reference [Gus99]). Practically we will discard the disconnected term for our calculations. Please note that we use a consequent four vector notation for the arguments from now on. Thus, we set $y = (\vec{y},\tau)$, $x = (\vec{x},t)$ and $0 = (\vec{0},0)$.

### 8.2.2 Sequential Sources and Propagators

The expressions for the three-point correlation functions still look very ugly. We will try to re-write the three-point functions in order to get them well-arranged. Our aim is to obtain expressions for the correlators which are of the following shape

$$C_\Gamma^{\mathcal{O}_q}(t,\tau;\vec{p}) = -N_s^3 \sum_{\vec{y},v,w} \mathrm{Tr}_{\mathrm{DC}}\left( {}^{SL}_{q}\Sigma_\Gamma(0,v;\vec{p},t)\, \mathcal{O}(v,w;y)\, {}^{LS}_{q}G(w,0)\right). \tag{8.2.15}$$

First, we have a look at the three-point correlation function for the $d$-quark insertion. Omitting the disconnected terms in (8.2.12) one gets

$$\begin{aligned} C_\Gamma^{\mathcal{O}_d}(t,\tau;\vec{p}) = & -N_s^3 \sum_{\vec{x},\vec{y},v,w} e^{-i\vec{p}\vec{x}} \varepsilon^{abc}\varepsilon^{a'b'c'} \mathrm{Tr}\left(\Gamma\, {}^{SS}_{s}G^{aa'}(x;0)\right) \\ & \times \mathrm{Tr}\left( {}^{SS}_{u}\widetilde{G}^{bb'}(x;0)\, {}^{SL}_{d}G^{cd}(x;v)\, \mathcal{O}^{de}(v,w;y)\, {}^{LS}_{d}G^{ec'}(w;0)\right) \\ = & -N_s^3 \sum_{\vec{y},v,w} \mathrm{Tr}\Big( \sum_{\vec{x}} \Big\{ e^{-i\vec{p}\vec{x}} \varepsilon^{abc}\varepsilon^{a'b'c'} \mathrm{Tr}\left(\Gamma\, {}^{SS}_{s}G^{aa'}(x;0)\right) {}^{SS}_{u}\widetilde{G}^{bb'}(x;0)\Big\} \\ & \times {}^{SL}_{d}G^{cd}(x;v)\, \mathcal{O}^{de}(v,w;y)\, {}^{LS}_{d}G^{ec'}(w;0)\Big). \end{aligned} \tag{8.2.16}$$

The $u$-quark correlator can be easily obtained by replacing the $d$-quark indices in (8.2.16) with $u$-quark indices. Omitting the disconnected terms in (8.2.14) one gets for the three-point correlation function of the $s$-quark

$$\begin{aligned} C_\Gamma^{\mathcal{O}_s}(t,\tau;\vec{p}) = & -N_s^3 \sum_{\vec{y},v,w} \mathrm{Tr}\Big( \sum_{\vec{x}} \Big\{ e^{-i\vec{p}\vec{x}} \varepsilon^{abc}\varepsilon^{a'b'c'} \mathrm{Tr}\left( {}^{SS}_{u}\widetilde{G}^{bb'}(x;0)\, {}^{SS}_{d}G^{cc'}(x;0)\right)\Gamma\Big\} \\ & \times {}^{SL}_{s}G^{ad}(x;v)\, \mathcal{O}^{de}(v,w;y)\, {}^{LS}_{s}G^{ea'}(w;0)\Big). \end{aligned} \tag{8.2.17}$$

Next, we define the objects in the curly brackets as *sequential sources*. For the $d$-quark case we obtain

$${}_{d}S_\Gamma^{a'a}(x,0;\vec{p}) = e^{-i\vec{p}\vec{x}} \varepsilon^{abc}\varepsilon^{a'b'c'} \mathrm{Tr}\left(\Gamma\, {}^{SS}_{s}G^{aa'}(x;0)\right) {}^{SS}_{u}\widetilde{G}^{bb'}(x;0). \tag{8.2.18}$$

The $u$-case can be obtained by the usual $u \leftrightarrow d$-replacement. For the $s$-quark the sequential source is given by

$${}_{s}S_\Gamma^{a'a}(x,0;\vec{p}) = e^{-i\vec{p}\vec{x}} \varepsilon^{abc}\varepsilon^{a'b'c'} \mathrm{Tr}\left( {}^{SS}_{u}\widetilde{G}^{bb'}(x;0)\, {}^{SS}_{d}G^{cc'}(x;0)\right)\Gamma. \tag{8.2.19}$$

This way the three-point function can be simplified to

$$C_{\Gamma}^{\mathcal{O}_q}(t,\tau;\vec{p}) = -N_s^3 \sum_{\vec{y},v,w} \mathrm{Tr}_{\mathrm{DC}} \left( \sum_{\vec{x}} \left\{ {}_qS_{\Gamma}(x,0;\vec{p})\, {}^{SL}_{q}G(x,v) \right\} \mathcal{O}(v,w;y)\, {}^{LS}_{q}G(w,0) \right). \tag{8.2.20}$$

Once again the expression in the curly brackets can be absorbed by the definition of the *sequential propagator*

$${}^{SL}_{q}\Sigma_{\Gamma}(0,v;\vec{p},t) = \sum_{\vec{x}} {}_qS_{\Gamma}(x,0;\vec{p})\, {}^{SL}_{q}G(x,v). \tag{8.2.21}$$

Now, we succeded in simplifying the three-point functions and obtained formula (8.2.15). The choice of the correlator (*u*/*d* or *s*) only depends on which sequential source ((8.2.16) or (8.2.17)) one is using for the calculation of the sequential propagator. By massively exploiting $\gamma_5$-hermiticity of the Dirac operator we obtain the following equation for the sequential propagator $\Sigma$ (8.2.21):

$$\sum_{v} {}_qD(v',v)\,\gamma_5\, {}^{SL}_{q}\Sigma_{\Gamma}(0,v;\vec{p},t)^{\dagger_{\mathrm{DC}}} = \sum_{\vec{x}} {}^{S}H(v',\vec{x};U,t)\,({}_qS_{\Gamma}(x,0;\vec{p})\,\gamma_5)^{\dagger_{\mathrm{DC}}}\,\delta_{v'_0,t}. \tag{8.2.22}$$

We see that this form of $\Sigma$ is like a Greens function from the complicated looking source given on the RHS of the equation.The matrix inversion techniques described in the previous chapter can thus be applied again here. To obtain the propagator ${}^{SL}_{q}\Sigma_{\Gamma}(0,v;\vec{p},t)$ from the result of the inversion algorithm $\gamma_5\, {}^{SL}_{q}\Sigma_{\Gamma}(0,v;\vec{p},t)^{\dagger_{\mathrm{DC}}}$ we have to perform the following operation:

$${}^{SL}_{q}\Sigma_{\Gamma}(0,v;\vec{p},t) = \left( \gamma_5 \left[ \gamma_5\, {}^{SL}_{q}\Sigma_{\Gamma}(0,v;\vec{p},t)^{\dagger_{\mathrm{DC}}} \right] \right)^{\dagger_{\mathrm{DC}}}. \tag{8.2.23}$$

Finding the three-point correlation function is a two stage process. In stage I the ususal Greens function from $0 = (\vec{0},0)$ to any point $x$ is calculated. In stage II a second inversion is made, but – in contrast to the normal inversion procedure – on the sources given in formula (8.2.19) for the sequential propagator of the strange quark and in formula (8.2.18) for the sequential propagator of the up- and down-quark, respectively. The advantage of this technique is simply that by tying together the two Greens functions properly any operator insertion can be performed without any additional numerical costs, independent of the underlying (derivative- or $\gamma$-) structure of the operator. The disadvantage is that for each baryon state, momentum $\vec{p}$ and baryon sink position $t$ a separate inversion is required. Practically we must restrict ourselves to one value.

## 8.3 Status of the Numerical Calculations

Originally it was planed to perform the calculations of the N-Point functions with the software used in [G$^+$02]. Unfortunately, it turned out that this software package is not available anymore. Thus, we had to build up the complete software for the caluclation of the non-degenerate three-point functions from scratch. Due to the complexity of this thesis, it was not possible to finish this task in time. First test runs over an ensemble of 150 $n_f = 2$-configurations (provided by the QCDSF-collaboration) have been performed, but not yet evaluated. The status of the software project is the following. All the two- and three-point functions mentioned in this Chapter have successfully been implemented in the code. So far we used Jacobi-smeared Clover-Wilson-Fermions in our simulations. Currently, we are working on the read-out and analysing software. For that reason we are adapting the existing evaluation-software of the QCDSF-collaboration to our needs.

# Chapter 9

# Conclusions

## 9.1 Summary

### Part I

The goal of the first part of this thesis was to extract the analysing power $A_{UT}$ of inclusive charged mesons from $lp^{\uparrow} \rightarrow hX$-processes at the HERMES-experiment at DESY. The used data set taken on a transversely polarised target between 2002 and 2005 provides a tremendously large amount of statistics for this inclusive processes. We succeeded in dealing with this uniquely large amount of data. For this reason we built up a competely independent software package for the data selection, the particle identifiaction and the final analysis. For the latter we implemented an innovative extraction method of the analysing power $A_{UT}$. This method is based on the analysis of Fourier amplitudes and allows to measure the full analysing power without any influences originating from the acceptance of the HERMES spetrometer.
The result of our analysis is – so far – the most precise measurement of analysing powers for charged mesons, both among the DIS-experiments and among other experiments. These so-called single spin asymmetries, which are a function of the transverse momentum $P_{h\perp}$ and the longitudinal momentum fraction $P_{hz}/E_{Beam}$ of the hadrons, can be related to a specific quark distribution function of the proton: the leading-twist Sivers function $f_{1T}^{\perp q}$. The Sivers function describes the correlation between the transverse polarisation of the target nucleon and the transverse momentum $p_T$ of quarks.
We observed significantly large asymmetries for positvely charged pions (maximimum value $\sim 6\%$) and kaons (maximimum value $\sim 7\%$). For negatively charged mesons, the measured asymmetry equals zero over the complete kinematic range. For deeper investigations of the underlying physics processes contributing to the observed positive asymmetries, we succeeded in the disentenglement of several sub-processes conributing to the final asymmetry. As a result of our studies we can state that the Sivers function is dominted by leading-twist effects and that sub-leading twist effects are suppressed. Furthermore, the Sivers effect implies a non-vanishing orbital angular momentum of quarks inside the proton. Unfortunately, the Sivers function does not provide a quantitative estimation of the orbital angular momentum of the quarks. In particular, the analysing power $A_{UT}$ for positive kaons was found to be larger as that for postive pions, thus suggesting a significant Sivers function for the sea quarks.

### Part II

The goal of the second Part of this thesis was to calculate the spin structure of $\Lambda^0$ hyperon using partially quenched lattice-QCD. The $\Lambda^0$'s spin structure is especially sensitive to $SU(3)$ breaking effects and allows to access several quark distributions of the nucleon. It turned out that the software framework which is necessary to compute the relevant matrix elements, got lost over the past years. Thus we could not complete the calculations so far. Nevertheless, we succeeded in recovering the main parts of the code. First test runs over an ensemble of 150 gauge configurations have been successful so far. Furthermore, we implemented all kinds of two-point functions for mesons and baryons containing a strange quark. This allows us to determine the strange quark mass on the lattice in latter studies.

## 9.2 Outlook

### Part I

The measured analysing powers $A_{UT}$ look very promising for further studies. First, a cross-check of our measurements has to be performed. In addition the systematic uncertainties of the analysing powers have to be investigated and estimated. The major tool to access and reveal these uncertainties is the use of Monte Carlo simulations. Monte Carlo simulations can combine physics processes with the acceptance of the HERMES-spectrometer, for example. Thus we can estimate the impact of acceptance effects on the final, measured aymmetries. At the Transversity Week 2009 in Ferrara, the theory group of Anselmino showed strong interest in our results. As a consequence we will strengthen the collaboration with this group to provide experimental input for their theoretical studies.

### Part II

We will further build up the codes for two- and three-point functions which allow to access the spin structure of the $\Lambda^0$ hyperon. Furthermore the built up software-framework would allow the extraction of the mass of the strange quark from the lattice.

# Appendix A

# Appendix

## A.1 Conventions

The following metric tensor is used

$$g_{\mu\nu} = \begin{pmatrix} 1 & 0 & 0 & 0 \\ 0 & -1 & 0 & 0 \\ 0 & 0 & -1 & 0 \\ 0 & 0 & 0 & -1 \end{pmatrix}, \tag{A.1.1}$$

where the Greek indices run over 0, 1, 2, 3. In contrast, Latin indices are used for 1, 2, 3. The normalisation of the Levi–Civita tensor is defined by:

$$\varepsilon^{0123} = 1 = -\varepsilon_{0123}. \tag{A.1.2}$$

The Einstein summation convention is applied unless noted otherwise.

## A.2 Light-Cone Vectors

A four–vector with Cartesian contravariant components $a^\mu = (a^0, a^i)$ can be written as a Light–cone vector:

$$a^\mu = [a^-, a^+, \vec{a}_T] = \left[\frac{a^0 - a^3}{\sqrt{2}}, \frac{a^0 + a^3}{\sqrt{2}}, a^1, a^2\right], \tag{A.2.1}$$

where the $\pm$ components are along the light– cone axes $x\pm$. The scalar product of two light–cone vectors reads:

$$a \cdot b = a^+ b^- + a^- b^+ - \vec{a}_T \cdot \vec{b}_T. \tag{A.2.2}$$

In the Bjorken limit ($Q^2 \to \infty$, $\nu \to \infty$, $x$ const.) the four-momentum vectors of the proton and the virtual photon can be parametrised in light-cone coordinates as:

$$P^\mu = \left[\frac{M^2}{2P^+}, P^+, \vec{0}\right], \tag{A.2.3}$$

$$q^\mu = \left[\frac{Q^2}{2xP^+}, -xP^+, \vec{0}\right]. \tag{A.2.4}$$

This parametrisation is valid in any collinear frame, i.e., in any frame of reference in which the virtual–photon direction is antiparallel to the $x^3$ axis. For all collinear frames $P^+$ is the dominant variable in a $1/Q$ expansion. In the infinite momentum frame the plus component of the nucleon is of the order of $Q$.

## A.3 Dirac Matrices

The Dirac matrices $\gamma^\mu$ in the chiral representation are defined by means of the Pauli matrices $\sigma^i$:

$$\gamma^0 = \begin{pmatrix} 0 & \mathbb{1} \\ \mathbb{1} & 0 \end{pmatrix}, \quad \gamma^i = \begin{pmatrix} 0 & \sigma^i \\ -\sigma^i & 0 \end{pmatrix}, \tag{A.3.1}$$

where $\mathbb{1}$ is the $2 \times 2$ unit matrix. The product

$$\gamma_5 = i\gamma^0\gamma^1\gamma^2\gamma^3 = \begin{pmatrix} \mathbb{1} & 0 \\ 0 & -\mathbb{1} \end{pmatrix}, \tag{A.3.2}$$

anticommutes with all four $\gamma$–matrices: $\gamma^5\gamma^\mu = -\gamma^\mu\gamma^5$. As for any other Lorentz vector, the Dirac matrices $\gamma^\mu$ can be expressed in the light-cone coordinates with $\gamma^\pm = (\gamma^0 \pm \gamma^3)/\sqrt{2}$.

# Bibliography


[A+76] M. J. Alguard et al., *Deep inelastic scattering of polarized electrons by polarized protons*, Phys. Rev. Lett. **37** (1976), 1261.

[A+88] J. Ashman et al., *A measurement of the spin asymmetry and determination of the structure function g(1) in deep inelastic muon proton scattering*, Phys. Lett. **B206** (1988), 364.

[A+89] _____, *An investigation of the spin structure of the proton in deep inelastic scattering of polarized muons on polarized protons*, Nucl. Phys. **B328** (1989), 1.

[A+91] D. L. Adams et al., *Comparison of spin asymmetries and cross-sections in pi0 production by 200-GeV polarized anti-protons and protons*, Phys. Lett. **B261** (1991), 201–206.

[A+92a] _____, *High x(t) single spin asymmetry in pi0 and eta production at x(F) = 0 by 200-GeV polarized anti-protons and protons*, Phys. Lett. **B276** (1992), 531–535.

[A+92b] _____, *Large x(F) spin asymmetry in pi0 production by 200-GeV polarized protons*, Z. Phys. **C56** (1992), 181–184.

[A+93] B. Adeva et al., *Measurement of the spin dependent structure function g1(x) of the deuteron*, Phys. Lett. **B302** (1993), 533–539.

[A+94] D. Adams et al., *Measurement of the spin dependent structure function g1(x) of the proton*, Phys. Lett. **B329** (1994), 399–406.

[A+95] _____, *A New measurement of the spin dependent structure function g1(x) of the deuteron*, Phys. Lett. **B357** (1995), 248–254.

[A+96] P. L. Anthony et al., *Deep Inelastic Scattering of Polarized Electrons by Polarized $^3$He and the Study of the Neutron Spin Structure*, Phys. Rev. **D54** (1996), 6620–6650.

[A+97] B. Adeva et al., *The spin-dependent structure function g1(x) of the proton from polarized deep-inelastic muon scattering*, Phys. Lett. **B412** (1997), 414–424.

[A+98a] K. Ackerstaff et al., *HERMES spectrometer*, Nucl. Instrum. Meth. **A417** (1998), 230–265.

[A+98b] B. Adeva et al., *Polarised quark distributions in the nucleon from semi- inclusive spin asymmetries*, Phys. Lett. **B420** (1998), 180–190.

[A+00] A. Airapetian et al., *Observation of a single-spin azimuthal asymmetry in semi- inclusive pion electro-production*, Phys. Rev. Lett. **84** (2000), 4047–4051.

[A+01] A. Andreev et al., *Multiwire proportional chambers in the HERMES experiment*, Nucl. Instrum. Meth. **A465** (2001), 482–497.

[A+04] John Adams et al., *Cross sections and transverse single-spin asymmetries in forward neutral pion production from proton collisions at s**(1/2) = 200-GeV*, Phys. Rev. Lett. **92** (2004), 171801.

[A+05a] A. Airapetian et al., *Quark helicity distributions in the nucleon for up, down, and strange quarks from semi–inclusive deep–inelastic scattering*, Phys. Rev. **D71** (2005), 012003.

[A+05b] _____, *The HERMES polarized hydrogen and deuterium gas target in the HERA electron storage ring*, Nucl. Instrum. Meth. **A540** (2005), 68–101.

[A+06] M. Anselmino et al., *The general partonic structure for hadronic spin asymmetries*, Phys. Rev. **D73** (2006), 014020.

[A+07a] A. Airapetian et al., *Precise determination of the spin structure function g(1) of the proton, deuteron and neutron*, Phys. Rev. **D75** (2007), 012007.

[A+07b] M. Anselmino et al., *Transversity and Collins functions from SIDIS and e+ e- data*, Phys. Rev. **D75** (2007), 054032.

[A+08] C. Amsler et al., *Review of particle physics*, Phys. Lett. **B667** (2008), 1.

[A+09] A. Airapetian et al., *Search for a Two-Photon Exchange Contribution to Inclusive Deep-Inelastic Scattering*, HERMES Internal Draft 77, 2009.

[ABM+09] M. Anselmino, M. Boglione, S. Melis, F. Murgia, A. Prokudin, and U. D'Alesio, *Single Spin Asymmetries in ep-¿h+X processes*, vol. DIS 2009, DIS 2009, no. DIS 2009, DIS 2009, DIS 2009 2009, p. DIS 2009.

[AEL95] M. Anselmino, A. Efremov, and E. Leader, *The theory and phenomenology of polarized deep inelastic scattering*, Phys. Rept. **261** (1995), 1–124.

[AM90] X. Artru and M. Mekhfi, *Transversely polarized parton densities, their evolution and their measurement*, Zeitschrift fÃ¼r Physik C Particles and Fields **45** (1990), no. 4, 669–676.

[AMS+07] W. Augustyniak, A. Miller, G. Schnell, S. Yen, and P. Zupranski, *TMC - Vertex Reconstruction in the Presence of the HERMES Transverse Target Magnet*, Hermes Internal Report **07-008** (2007).

[AP77] Guido Altarelli and G. Parisi, *Asymptotic Freedom in Parton Language*, Nucl. Phys. **B126** (1977), 298.

[B+79] D. P. Barber et al., *Discovery of Three Jet Events and a Test of Quantum Chromodynamics at PETRA Energies*, Phys. Rev. Lett. **43** (1979), 830.

[B+83] Guenter Baum et al., *A new measurement of deep inelastic e p asymmetries*, Phys. Rev. Lett. **51** (1983), 1135.

[B+88] B. E. Bonner et al., *Analyzing Power Measurement in Inclusive pi0 Production at High x(f)*, Phys. Rev. Lett. **61** (1988), 1918.

[B+93] D. P. Barber et al., *The HERA polarimeter and the first observation of electron spin polarization at HERA*, Nucl. Instrum. Meth. **A329** (1993), 79–111.

[B+96] A. Bravar et al., *Single-spin asymmetries in inclusive charged pion production by transversely polarized antiprotons*, Phys. Rev. Lett. **77** (1996), 2626–2629.

[B+98] S. Bernreuther et al., *The HERMES back drift chambers*, Nucl. Instrum. Meth. **A416** (1998), 45–58.

[B+01] J. T. Brack et al., *The HERMES forward tracking chambers: Construction, operation, and aging effects*, Nucl. Instrum. Meth. **A469** (2001), 47–54.

[B+02] M. Beckmann et al., *The longitudinal polarimeter at HERA*, Nucl. Instrum. Meth. **A479** (2002), 334–348.

[Bac02] A. Bacchetta, *Probing the transverse spin of quarks in deep inelastic scattering*, Ph.D. thesis, Vrije Universiteit Amsterdam, 2002, hep-ph/0212025.

[BC03] K. Bora and D. Choudhury, *Transversity of quarks in a nucleon*, Pramana **61** (2003), no. 5, 979–985.

[BDDM04] A. Bacchetta, U. D'Alesio, M. Diehl, and C. A. Miller, *Single-spin asymmetries: The Trento conventions*, Phys. Rev. **D70** (2004), 117504.

[BHS02] Stanley J. Brodsky, Dae Sung Hwang, and Ivan Schmidt, *Final-state interactions and single-spin asymmetries in semi-inclusive deep inelastic scattering*, Phys. Lett. **B530** (2002), 99–107.

[BJ93] M. Burkardt and R. L. Jaffe, *Polarized q–> lambda fragmentation functions from e+e—> lambda + x*, Phys. Rev. Lett. **70** (1993), no. 17, 2537–.

[Bjo69] J. D. Bjorken, *Asymptotic Sum Rules at Infinite Momentum*, Phys. Rev. **179** (1969), 1547–1553.

[BM98] Daniel Boer and P. J. Mulders, *Time-reversal odd distribution functions in leptoproduction*, Phys. Rev. **D57** (1998), 5780–5786.

[BM00] ———, *Color gauge invariance in the Drell-Yan process*, Nucl. Phys. **B569** (2000), 505–526.

[BMP04] Alessandro Bacchetta, Piet J. Mulders, and Fetze Pijlman, *New observables in longitudinal single-spin asymmetries in semi-inclusive DIS*, Phys. Lett. **B595** (2004), 309–317.

[BP69] J. D. Bjorken and Emmanuel A. Paschos, *Inelastic Electron Proton and gamma Proton Scattering, and the Structure of the Nucleon*, Phys. Rev. **185** (1969), 1975–1982.

[BR03] V. Barone and P. G. Ratcliffe, *Transverse Spin Physics*, World Scientific, New Jersey, London, Singapore, Hong Kong, 2003.

[Bra99] A. Bravar, *Hadron azimuthal distributions and transverse spin asymmetries in DIS of leptons off transversely polarized targets from SMC*, Nucl. Phys. Proc. Suppl. **79** (1999), 520–522.

[Bur02] Matthias Burkardt, *Impact parameter dependent parton distributions and transverse single spin asymmetries*, Phys. Rev. **D66** (2002), 114005.

[Bur04] ———, *Quark correlations and single spin asymmetries*, Phys. Rev. **D69** (2004), 057501.

[CG69] C. G. Callan and D. J. Gross, *High-energy electroproduction and the constitution of the electric current*, Phys. Rev. Lett. **22** (1969), 156–159.

[CHL94] John C. Collins, Steve F. Heppelmann, and Glenn A. Ladinsky, *Measuring transversity densities in singly polarized hadron hadron and lepton - hadron collisions*, Nucl. Phys. **B420** (1994), 565–582.

[CM04] John C. Collins and Andreas Metz, *Universality of soft and collinear factors in hard- scattering factorization*, Phys. Rev. Lett. **93** (2004), 252001.

[Col02] John C. Collins, *Leading-twist Single-transverse-spin asymmetries: Drell- Yan and Deep-Inelastic Scattering*, Phys. Lett. **B536** (2002), 43–48.

[CSS88] John C. Collins, Davison E. Soper, and George Sterman, *Factorization of Hard Processes in QCD*, Adv. Ser. Direct. High Energy Phys. **5** (1988), 1–91.

[Die07] M. Diefenthaler, *HERMES measurements of Collins and Sivers asymmetries from a transversely polarised hydrogen target*, arXiv:0706.2242v2 (2007).

[DNLRS+08] L. De Nardo, A. Lopez Ruiz, G. Schnell, N. Makins, and A. De La Ossa, *Search for a Two-photon-exchange signal at HERMES*, Hermes Release Report (2008).

[Dok77] Y. L. Dokshitzer, *Calculation of the Structure Functions for Deep Inelastic Scattering and e+ e- Annihilation by Perturbation Theory in Quantum Chromodynamics*, Sov. Phys. JETP **46** (1977), 641–653.

[EFP83] R. Keith Ellis, W. Furmanski, and R. Petronzio, *Unraveling Higher Twists*, Nucl. Phys. **B212** (1983), 29.

[EHK98] R. G. Edwards, Urs M. Heller, and T. R. Klassen, *The effectiveness of non-perturbative O(a) improvement in lattice QCD*, Phys. Rev. Lett. **80** (1998), 3448–3451.

[EJ74] John Ellis and Robert Jaffe, *Sum rule for deep-inelastic electroproduction from polarized protons*, Phys. Rev. D **9** (1974), no. 5, 1444–.

[Fey69] Richard P. Feynman, *Very high-energy collisions of hadrons*, Phys. Rev. Lett. **23** (1969), 1415–1417.

[G+96] M. Goeckeler et al., *Lattice Operators for Moments of the Structure Functions and their Transformation under the Hypercubic Group*, Phys. Rev. **D54** (1996), 5705–5714.

[G+02] ———, *A lattice study of the spin structure of the Lambda hyperon*, Phys. Lett. **B545** (2002), 112–118.

[G+07] ———, *Transverse spin structure of the nucleon from lattice QCD simulations*, Phys. Rev. Lett. **98** (2007), 222001.

[Gab08] D. Gabbert, *Determination of the structure function F2 at Hermes*, Ph.D. thesis, Universität Hamburg, 2008.

[GBK96] R. Gupta, T. Bhattacharya, and G. Kilcup, *Comparison of Inversion Algorithms for Wilson Fermions on the CM5*, hep-lat/9605029v1 (1996).

[GHI+96] M. Goeckeler, R. Horsley, E. M. Ilgenfritz, H. Perlt, P. Rakow, G. Schierholz, and A. Schiller, *Polarized and unpolarized nucleon structure functions from lattice qcd*, Phys. Rev. D **53** (1996), no. 5, 2317–.

[GL72] V. N. Gribov and L. N. Lipatov, *e+ e- pair annihilation and deep inelastic e p scattering in perturbation theory*, Sov. J. Nucl. Phys. **15** (1972), 675–684.

[GM64] Murray Gell-Mann, *A Schematic Model of Baryons and Mesons*, Phys. Lett. **8** (1964), 214–215.

[Gup98] Rajan Gupta, *Introduction to Lattice QCD*, 1998.

[Gus99] S. Gusken, *Flavor singlet phenomena in lattice qcd*, hep-lat/9906034v1 (1999).

[GW82] Paul H. Ginsparg and Kenneth G. Wilson, *A Remnant of Chiral Symmetry on the Lattice*, Phys. Rev. **D25** (1982), 2649.

[HER] HERMES Data Quality Group, *Offline Data Quality - µDST Productions*, Website, `http://www-hermes.desy.de/groups/daqlgrp/OFFLINE_DQ/uDST/index.html`.

[HM84] F. Halzen and A. D. Martin, *Quarks and Leptons: An Introductory Course in Modern Particle Physics*, John Wiley & Sons, 1984.

[Hom03] B. Hommez, *Hadron identification with the HERMES RICH*, Nucl. Instrum. Meth. **A502** (2003), 294–299.

[Jaf96] R. L. Jaffe, *Spin, Twist and Hadron Structure in Deep Inelastic Processes*, arXiv:hep-ph/9602236v1 (1996).

[JJ91] R. L. Jaffe and Xiang-Dong Ji, *Chiral odd parton distributions and polarized drell-yan*, Phys. Rev. Lett. **67** (1991), 552–555.

[JMY04] Xiang-dong Ji, Jian-Ping Ma, and Feng Yuan, *QCD factorization for spin-dependent cross sections in DIS and Drell-Yan processes at low transverse momentum*, Phys. Lett. **B597** (2004), 299–308.

[JMY05] Xiang-dong Ji, Jian-ping Ma, and Feng Yuan, *QCD factorization for semi-inclusive deep-inelastic scattering at low transverse momentum*, Phys. Rev. **D71** (2005), 034005.

[JR75] F. James and M. Roos, *Minuit: A System for Function Minimization and Analysis of the Parameter Errors and Correlations*, Comput. Phys. Commun. **10** (1975), 343–367.

[K+76] R. D. Klem et al., *Measurement of Asymmetries of Inclusive Pion Production in Proton Proton Interactions at 6-GeV/c and 11.8-GeV/c*, Phys. Rev. Lett. **36** (1976), 929–931.

[K+99] K. Krueger et al., *Large analyzing power in inclusive pi+- production at high x(F) with a 22-GeV/c polarized proton beam*, Phys. Lett. **B459** (1999), 412–416.

[KE87] S. B. Kowalski and H. A. Enge, *The ion-optical program raytrace*, Nucl. Instrum. Meth. **A258** (1987), 407.

[KS87] G. W. Kilcup and Stephen R. Sharpe, *A TOOL KIT FOR STAGGERED FERMIONS*, Nucl. Phys. **B283** (1987), 493.

[LDW92] Derek B. Leinweber, Terrence Draper, and R. M. Woloshyn, *Decuplet baryon structure from lattice qcd*, Phys. Rev. D **46** (1992), no. 7, 3067–.

[LH08] R. Lamb and A. Hillenbrand, *Event Level RICH algorithm: An explanation and user guide*, Hermes Internal Report **07-017** (2008).

[Lip75] L. N. Lipatov, *The parton model and perturbation theory*, Sov. J. Nucl. Phys. **20** (1975), 94–102.

[LMR+05] D.B. Leinweber, W. Melnitchouk, D.G. Richards, A.G. Williams, and J.M. Zanotti, *Baryon spectroscopy in lattice qcd*, 2005, pp. 71–112.

[LW85] M. Luscher and P. Weisz, *On-Shell Improved Lattice Gauge Theories*, Commun. Math. Phys. **97** (1985), 59.

[Man92] A. V. Manohar, *An Introduction to Spin Dependent Deep Inelastic Scattering*, arXiv:hep-ph/9204208v1 (1992).

[MT96] P. J. Mulders and R. D. Tangerman, *The complete tree-level result up to order 1/Q for polarized deep-inelastic leptoproduction*, Nucl. Phys. **B461** (1996), 197–237.

[PS95] M. E. Peskin and D. V. Schroeder, *An Introduction to Quantum Field Theory*, Westview Press, 1995.

[S+90] S. Saroff et al., *SINGLE SPIN ASYMMETRY IN INCLUSIVE REACTIONS polarized P, P GOES TO pi+, pi-, AND P AT HIGH P(t) AT 13.3-GeV/c AND 18.5-GeV/c*, Phys. Rev. Lett. **64** (1990), 995.

[Sak69] J. J. Sakurai, *Vector meson dominance and high-energy electron proton inelastic scattering*, Phys. Rev. Lett. **22** (1969), 981–984.

[Siv90] D. Sivers, *Single Spin Production Asymmetries from the Hard Scattering of Point-Like Constituents*, Phys. Rev. **D41** (1990), 83.

[Siv91] _____, *Hard scattering scaling laws for single spin production asymmetries*, Phys. Rev. **D43** (1991), 261–263.

[Siv06] _____, *Single-spin observables and orbital structures in hadronic distributions*, Phys. Rev. **D74** (2006), 094008.

[SMM08] Jun She, Yajun Mao, and Bo-Qiang Ma, *Left-right asymmetry in semi-inclusive deep inelastic scattering process*, Phys. Lett. **B666** (2008), 355–358.

[Sof95] Jacques Soffer, *Positivity constraints for spin dependent parton distributions*, Phys. Rev. Lett. **74** (1995), 1292–1294.

[SS72] J. J. Sakurai and D. Schildknecht, *Generalized vector dominance and inelastic electron - proton scattering*, Phys. Lett. **B40** (1972), 121–126.

[ST64] A. A. Sokolov and I. M. Ternov, *On Polarization and spin effects in the theory of synchrotron radiation*, Sov. Phys. Dokl. **8** (1964), 1203–1205.

[SW85] B. Sheikholeslami and R. Wohlert, *Improved Continuum Limit Lattice Action for QCD with Wilson Fermions*, Nucl. Phys. **B259** (1985), 572.

[WDL92] Walter Wilcox, Terrence Draper, and Keh-Fei Liu, *Chiral limit of nucleon lattice electromagnetic form- factors*, Phys. Rev. **D46** (1992), 1109–1122.

[Wen01] J. Wendland, *Particle Identifiaction for HERMES Run I*, Hermes Internal Report (2001).

[Wil74] Kenneth G. Wilson, *CONFINEMENT OF QUARKS*, Phys. Rev. **D10** (1974), 2445–2459.

# Acknowledgements

First and foremost I would like to thank Andreas Schäfer who gave me the opportunity to write this uncommon, very challenging thesis in his group. He gave me maximum freedom to work on the data analysis at the HERMES experiment and supported me where- and whenever possible. Thus I could join several conferences and workshops in Ferrara, Trento, Berlin and Hamburg. The combination between experiment and theory was hard, but very fruitful.

I also want to thank Gunar Schnell for making the experimental side of this thesis possible and for integrating me in the ”transversity” group at HERMES. I am also grateful for the supervision by Markus Diefenthaler. Although he was about to finish his PhD-thesis he agreed to the supervision. Thanks, Markus, for introducing me to the experimental side of high energy physics!

Further thanks goes to Caroline Riedl who supported me in the bad and good times of the thesis. She always succeeded in giving me hope and motivation for this challenging thesis.

In addition I want to Charlotte van Huelse and Alejandro López Ruìz for hosting me in the office of the Ghent-Group ;-) I really enjoyed the time being and the nice discussions about (non-)physics topics.

Special thanks goes to the ”gods” of object-orientated programming, Andreas Mussgiller and Alberto Martínez de la Ossa, for their help concerning problems with C++, Hanna++ and the ROOT framework. Without their help I wouldn’t have succeeded in building up my own, independent analysing code. Futhermore, I want to thank all the active members contributing to the HERMES-wiki. Without this source of (really!) profound knowledge on details about all kinds of analysis, I sometimes would have been completely lost.

Concerning the lattice-QCD part of my diploma thesis I want to thank Dirk Pleiter, Meinulf Göckeler and James Zanotti for always giving me a hand when needed. Special thanks goes to Martin Gürtler for his very, very strong support during the development of the three-point code, based on the TAO-language. I also want to thank Monika Mascheck for all her help concerning administrative concerns.

In addition I want to thank all the people making life outside physics enjoyable!

Finally, I want to express my greatest gratitude to my parents who always supported me during my studies and made all this possible.

# Erklärung

Hiermit erkläre ich, dass ich diese Diplomarbeit selbstständig angefertigt und keine Hilfsmittel außer den in der Arbeit angegebenen benutzt habe.

Regensburg, 31.05.2009
Ort, Datum

Florian Sanftl